



MONASH University

The stress-corrosion cracking in Ti-8Al-1Mo-1V

Sheng Cao

Bachelor of Engineering (with Honours) in Materials Engineering

A thesis submitted for the degree of *Doctor of Philosophy* at

Monash University in 2017

Department of Materials Science and Engineering

Monash University

VICTORIA, AUSTRALIA

Copyright notice

© The author (2017).

*I certify that I have made all reasonable efforts to secure copyright permissions
for third-party content included in this thesis and have not knowingly added
copyright content to my work without the owner's permission.*

ABSTRACT

Compared to the widely used Ti-6Al-4V, Ti-8Al-1Mo-1V (Ti-811) is characterized by a lower density and a higher elastic modulus. However, it suffers from stress-corrosion cracking (SCC). Crystallographic texture and ordered α_2 precipitates are two known factors influencing the SCC properties of Ti-811. However, previous studies were conducted on materials with an intrinsic texture, and the discussion of texture effects was on a macroscale. In this work, electron backscatter diffraction (EBSD) was applied to investigate the effect of microtexture in materials with an intrinsic texture, and designed hot isostatic pressing (HIPping) and post heat treatment scheme were conducted to study the effect of α_2 precipitates without the complicating effects of texture. The result shows that the presence of both microtexture and α_2 precipitates will increase the SCC susceptibility. EBSD investigation illustrates that the SCC crack propagation direction was aligned with the microtextured regions in wrought Ti-811, and α grains were favourably orientated for basal $< a >$ slip along the SCC crack. In the absence of both crystallographic microtexture and α_2 precipitates, there was no SCC crack propagation. Therefore, it is shown for the first time that SCC susceptibility in Ti-811 can be eliminated entirely by implementing the HIPping process and post heat treatment used in this work.

A fracture mode transition from dimples to facets was presented at the starting point of aqueous NaCl SCC tests in both milled Ti-8Al-1Mo-1V bar and powder hot isostatic pressed (HIPped) Ti-8Al-1Mo-1V materials. An understanding of the transition between the pre-crack region (fractured in air) and SCC crack region (failed in 0.1M NaCl aqueous solutions) is needed to reveal the SCC mechanism. Transmission electron backscatter diffraction (T-EBSD) and transmission electron microscope analysis on focused ion beam (FIB) lift-out lamellae were used to study the dislocation nature and density underneath the fracture surface. It was found that the fracture mode transition accompanied with changes in activated dislocation type from

basal $\langle a \rangle$ to basal $\langle a \rangle$ and $\langle c + a \rangle$, and increased dislocation density, those changes are believed to be related to the absorbed and diffused hydrogen in SCC. The possible SCC mechanism might be a combination of absorption induced dislocation emission (AIDE) and hydrogen enhanced localized plasticity (HELP) mechanisms for Ti-8Al-1Mo-1V.

DECLARATION

This thesis contains no material which has been accepted for the award of any other degree or diploma at any university or equivalent institution and that, to the best of my knowledge and belief, this thesis contains no material previously published or written by another person, except where due reference is made in the text of the thesis.

Signature: *Sheng Cao*

Print Name: SHENG CAO

Date: 20/03/2017

PUBLICATIONS AND PRESENTATIONS DURING ENROLMENT

Publications:

S. Cao, C.V.S. Lim, B. Hinton, X. Wu, Effects of microtexture and Ti₃Al (α_2) precipitates on stress-corrosion cracking properties of a Ti-8Al-1Mo-1V alloy, Corros. Sci. 116 (2017) 22–33.

Based on chapter IV in the thesis.

S. Cao, S. Zhu, C. V. S. Lim, X. Zhou, X. Chen, B. R. W. Hinton, R. R. Boyer, J. C. Williams, X. Wu, The mechanism of aqueous stress-corrosion cracking of $\alpha + \beta$ titanium alloys, “Under Review”. Based on chapter V in the thesis.

Presentations:

27th Aeromat Conference and Exposition (May 2016): Presentation on topic of “Study of Stress-corrosion Cracking Mechanism by Direct Observation and Analysis of Dislocation Substructure in α Phase”.

146th TMS Annual Meeting & Exhibition (Feb-Mar 2017): Presentation on topic of “Stress-corrosion Cracking in Ti-8Al-1Mo-1V”.

ACKNOWLEDGEMENTS

Firstly I would like to thank the Australian Postgraduate Awards (APA) and International Postgraduate Research Scholarship (IPRS) for the sponsorship of this research, which have enabled me to undertake this research at Monash University. I would also like to express my appreciation to the technical support from Monash Centre of Electron Microscopy (MCEM) and Monash Centre for Additive Manufacturing (MCAM) during my candidature. Special thanks to my advisor Prof. Xinhua Wu and Dr. Chao Voon Samuel Lim, for their tremendous guidance and support in this project.

I would like to acknowledge the help of Prof. Nick Birbilis, Dr. Xiaobo Chen, and Dr. Steven Knight on stress-corrosion cracking tests. I would also like to acknowledge Dr. Yu Chen, Dr. Xi-ya Fang, Dr. Jisheng Ma, Dr. Russell King, and Mr. Renji Pan for their training in SEM, TEM, and FIB lift-out. I would like to extend my acknowledgements to Dr. Suming Zhu for the help in the dislocation contrast experiment and Dr. Yichao Zou in the HRTEM experiment. Thank you to Dr. Bruce Hinton for the fruitful discussion in the corrosion aspect of my project.

I would like to express many thanks to Ms. Jane Moodie and Ms. Jackie Shurvinton, for her patient help with my English.

Thank you to my colleagues, Dr. Lingfei Cao, Dr. Tom Jarvis, Mr. Simon Logsdail, Mr. John Shurvinton, Dr. Dacian Tomus, Mr. Yu Zhang, Mr. Xigen Zhou.

Finally, thank you to my father and mother for their ongoing support, although they are thousand miles away in China.

TABLE OF CONTENTS

ABSTRACT	I
DECLARATION	III
PUBLICATIONS AND PRESENTATIONS DURING ENROLMENT	IV
ACKNOWLEDGEMENTS	V
LIST OF FIGURES	IX
LIST OF TABLES.....	XIV
1 CHAPTER I: LITERATURE REVIEW	1
1.1 Introduction.....	1
1.2 Metallurgy of Titanium Alloys	3
1.2.1 Phase Diagram and Crystal Structures	3
1.2.2 Alloying Elements.....	5
1.2.3 Phase Transformations	7
1.2.4 Classification of Titanium Alloys	9
1.3 Deformation Behaviours	11
1.3.1 Schmid Factor	11
1.3.2 Deformation Modes of α Phase.....	13
1.3.3 Deformation Modes of β Phase.....	16
1.3.4 Deformation Modes of α_2 Precipitates	16
1.3.5 Deformation Modes of Martensite	18
1.4 Texture	18
1.4.1 Texture Evolution	18
1.4.2 The Effect of Texture	19
1.4.3 The Effect of Microtexture.....	21
1.5 Stress-corrosion Cracking.....	23
1.5.1 Corrosion Behaviour	23
1.5.2 Stress-corrosion Cracking Characteristics and Mechanisms	26
Dissolution Mechanism:	27
Film Induced Cleavage (FIC):	28
Hydride Formation and Fracture:.....	29
Hydrogen Enhanced Decohesion (HEDE):.....	30
Hydrogen Enhanced Localized Plasticity (HELP):.....	31
Absorption Induced Dislocation Emission (AIDE):	32
Hybrid Mechanism:	33
1.5.3 Role of Environment and Metallurgy on SCC Properties in Ti alloys.....	34

Effect of Ion Additions and Concentration	38
Effect of Crystallographic Orientations	40
Effect of Presented Phases and Microstructure.....	43
1.5.4 Role of Hydrogen in SCC of Titanium Alloys.....	45
2 CHAPTER II: RESEARCH OBJECTIVES	51
3 CHAPTER III: EXPERIMENTAL METHODS	55
3.1 Materials and Heat treatment	55
3.2 SCC Tests and Mechanical Tests.....	61
3.3 Microstructure and Fracture Surface Characterization	63
3.4 TEM Sample Preparation and Analysis	63
4 CHAPTER IV: STRESS-CORROSION CRACKING: EFFECT OF VARIABLES.....	67
4.1 Experimental Results	67
4.1.1 Microstructure and Texture.....	68
4.1.2 Mechanical Properties.....	74
4.1.3 Stress-corrosion Cracking Properties.....	78
4.2 Discussions	85
4.2.1 Effect of the Microtexture.....	86
4.2.2 Effect of the α_2 Precipitates	88
4.2.3 Reduction and Elimination of Stress-corrosion Cracking Susceptibility	89
4.2.4 Mechanism of Propagation Stress-corrosion Cracking Facets Formation	90
4.3 Summary	93
5 CHAPTER V: STUDY OF THE AQUEOUS SCC MECHANISM(S) IN Ti-8Al-1Mo-1V	95
5.1 Experimental Results	95
5.1.1 Fractography	95
5.1.2 FIB Lift-out and T-EBSD	97
5.1.3 Dislocation Contrast Analysis.....	100
5.2 Discussion	105
5.2.1 Nature of Dislocation	105
5.2.2 Dislocation Density.....	106
5.2.3 Hydrogen Diffusion	107
5.2.4 Crystallographic Orientation of SCC Faceted Planes	110
5.2.5 SCC Mechanisms	112
5.3 Summary	114
6 CHAPTER VI: CONCLUSIONS	115
7 CHAPTER VII: SUGGESTIONS FOR FUTURE WORK	117
REFERENCE.....	118

8 Appendix.....	123
-----------------	-----

LIST OF FIGURES

Fig. 1.1 Specific strength and operating temperature of various materials [8]	1
Fig. 1.2 Ti-Al Binary phase diagram. The highlighted red dashed line denotes 8 Wt. % Al coposition. [8, 9].....	4
Fig. 1.3 Crystal structure of α and β phases of Titanium [8]	4
Fig. 1.4 D019 crystal structure of Ti_3Al (α_2) phase [8].....	5
Fig. 1.5 Effects of alloying elements on phase diagram for Ti alloys [8, 9].....	6
Fig. 1.6 Burgers relationship between BCC (β) and HCP (α) crystals during the β/α phase transformation [9]	8
Fig. 1.7 Pseudo-binary β -isomorphous phase diagram [24]	10
Fig. 1.8 Diagram of calculating critical resolve shear stress [26].....	12
Fig. 1.9 Slip planes and directions of HCP α titanium [8]	13
Fig. 1.10 Influence of temperature on CRSS for slip systems with $\langle a \rangle$ and $\langle c + a \rangle$ Burgers Vectors in single crystal of Ti-6.6Al [8]	15
Fig. 1.11 Dark-field TEM image shows a slip band, in which the α_2 precipitates are destroyed in a Ti-6.6Al crystal, $B=\{10\bar{1}1\}$ [28].....	17
Fig. 1.12 The influence of deformation modes and temperatures on the texture type in Ti-6Al-4V, where RD is the rolling direction [9].	19
Fig. 1.13 Influence of texture and test direction on macrocrack propagation in Ti-6Al-4V having a fully equiaxed microstructure with α grain size at 12 μm , (a) in vacuum, (b) in 3.5% NaCl aqueous solution. T is the transverse texture, and B/T is the basal/transverse texture. TD and RD are loading directions. [8]	20
Fig. 1.14 Inverse pole figure (IPF) of wrought TIMET Ti-8Al-1Mo-1V bar material [13]	22
Fig. 1.15 Pourbaix diagram of Ti-H ₂ O system at 25 °C [53]	24
Fig. 1.16 SCC data representation for (a) type 1 test method: a static load is applied on smooth samples, (b) and (c) for type 2 test: a static or dynamic load is applied on samples with notches or pre-cracks [60].....	26
Fig. 1.17 Illustration of slip dissolution mechanism [58]	27
Fig. 1.18 Illustration of film induced cleavage mechanism.[58]	28
Fig. 1.19 Illustration of hydride formation and fracture mechanism [65].....	29
Fig. 1.20 Hydrogen Enhanced Decohesion (HEDE) mechanism at (i) ahead of crack tip, (ii) crack tip, (iii) grain boundaries [65].	31
Fig. 1.21 Illustration of Hydrogen Enhanced Localized Plasticity (HELP) processes, involving a mircovoid-coalescence process, and a localized plasticity in high hydrogen concentration region.[65]	32
Fig. 1.22 Illustration of Absorption Induced Dislocation Emission (AIDE) mechanism, in which absorbed hydrogen caused dilocation emission [65]	33
Fig. 1.23 Illustration of hybride SCC mechanisms [65].	34
Fig. 1.24 Transgranular SCC crack of Ti-8Al-1Mo-1V tested in aqueous NaCl solution [16]	35
Fig. 1.25 SCC initiation facets on the fracture surface of Ti-8Al-1Mo-1V tested in 3.5% NaCl solution at 95% yield strength, 1 indicates the primary initiation site and 2-6 are the secondary initiation sites [75].....	36
Fig. 1.26 SCC Propagation facets on the fracture surface of Ti-8Al-1Mo-1V tested in 3.5% NaCl solution at 95% yield strength [75]	37

Fig. 1.27 Facet crystallography of as-received Ti-8Al-1Mo-1V in aqueous 3.5% NaCl solution [13]	38
Fig. 1.28 Effect of ions in solution, (a) effect of Cl^{-1} concentration on crack propagation rate of Ti-8Al-1Mo-1V, (b) Effect of SO_4^{2-} or NO_3^{-1} on SCC crack propagation [36]	38
Fig. 1.29 Effect of microstructure on SCC susceptibility of Ti-8Al-1Mo-1V with different microstructures, SC (step cooled - solution treated at 820°C and then step-cooled to 450°C): designed to promote α_2 precipitation, MA (wrought annealed - solution treated at 820°C and then furnace-cooled): equiaxed microstructure with α_2 precipitates formed during the cooling , DA (duplex annealed - solution treated at 820°C and then water-quenched): bi-modal microstructure with no α_2 precipitates [36].	39
Fig. 1.30 Effect of hydrogen ion concentration in solution on SCC susceptibility of Ti-8Al-1Mo-1V [36].....	40
Fig. 1.31 Basal pole figure of hand wrought Ti-8Al-1Mo-1V plate [36].....	40
Fig. 1.32 (a) SCC specimen orientations, (b) stress-corrosion susceptibility as a function of specimen orientations in 0.6 M aqueous NaCl solution [36, 80].	41
Fig. 1.33 SCC crack propagates parallel to the basal planes of α phase [36, 80].	42
Fig. 1.34 Stress-corrosion susceptibility relative to basal pole intensity in tensile axis [79].....	42
Fig. 1.35 Effect of presented phases on stress-corrosion cracking of Ti-8Al-1Mo-1V: (a) Crack initiation load, (b) Crack propagation velocity [36, 81].....	43
Fig. 1.36 Crack propagation velocity versus stress intensity factor for Ti-8Al-1Mo-1V with 3 different processing routes, SC (step cooled - solution treated at 820°C and then step-cooled to 450°C): designed to promote α_2 precipitation, MA (wrought annealed - solution treated at 820°C and then furnace-cooled): equiaxed microstructure with α_2 precipitates formed during the cooling , DA (duplex annealed - solution treated at 820°C and then water-quenched): bi-modal microstructure with no α_2 precipitates [36].	44
Fig. 1.37 Fracture toughness (K_{IC}) and threshold SCC stress intensity (K_{ISCC}) of Ti-8Al-1Mo-1V with various hydrogen contents [16].....	46
Fig. 1.38 The effect of hydrogen on dislocation velocity, I: the first introduce of hydrogen into the environment cell, II: hydrogen introduced by stage I has been removed and then re-introduced into the environment cell [67].	48
Fig. 1.39 Current, pH, and potential distribution of the fluid within crevice as a function of time for a CP titanium alloys in neutral solution, (1) potential of the Ti sample outside the crevice, (2) potential of the Ti sample inside the crevice, (3) corrosion current, (4) crevice pH. The electrode potential is referenced to the Ag/AgCl (0.1 M KCl) electrode [85].	49
Fig. 1.40 pH distribution of the fluid within the aqueous SCC crack for titanium alloys in neutral solution [64].....	49
Fig. 3.1 Ti-8Al-1Mo-1V pre-alloyed powder particles size distribution.	55
Fig. 3.2 Ti-8Al-1Mo-1V pre-alloyed powder: (a) secondary electron (SE) image of an overview for powder size distribution, powders were attached to a conductive carbon tape, (b) backscatter electron (BSE) image shows the Ti-8Al-1Mo-1V pre-alloyed powder with a fully lamellar microstructure, powders were mounted in conductive resin.	56
Fig. 3.3 Calculated isopleth of Ti-Al-Mo-V alloys with weight fraction of Mo and V being fixed at 0.01.	57
Fig. 3.4 Illustration of hot isostatic pressing (HIPping) [99]	58
Fig. 3.5 Illustration of a post heat treatment: 30 minutes at 860 °C followed by water quench (WQ). The black dashed line is the martensitic transformation start temperature (M_s) at 900 °C [11], the blue dashed line is the α_2 ordering transformation temperature at 837 °C.....	59

Fig. 3.6 Illustration of a DCB sample with a C-L orientation in the wrought Ti-8Al-1Mo-1V bar.	60
Fig. 3.7. Schematic diagram of Double Cantilever Beam (DCB) samples with dimensions (mm), a0 – starting crack length, B – width, co – distance from sample edge to loading axis, 2H – height, L – length.	62
Fig. 3.8. Illustration of a dual (FIB-SEM) system, which is able to provide real-time SEM imaging during the FIB milling processes [109].....	64
Fig. 3.9. Illustration of fractured SCC samples in the top view of the DCB sample in Fig. 3.7.....	65
Fig. 4.1 Backscattering electron (BSE) images showing the microstructure of (a) wrought Ti-811, (b) wrought Ti-811 + HT860, (c) HIPped Ti-811, and (d) HIPped Ti-811 + HT860. Prior particle boundaries are denoted by black dashed lines in (c) and (d). In all images, dark area is α phase and bright area indicates β phase.	68
Fig. 4.2 (a) Dark field (DF) TEM image of wrought Ti-811 bar, (b) DF TEM image of HIPped Ti-811, (c) Bright field TEM image of HIPped Ti-811 + HT860 – suppressing α_2 ordering transformation; beam parallel to $[0110]_{\alpha}$	70
Fig. 4.3 (a) High resolution TEM (HR-TEM) image of ordered and disordered regions in HIPped Ti-811 sample, (b) HR-TEM image from box b, (c) and (d) [2110] fast Fourier transforms (FFT) pseudo-diffraction patterns processed from boxes c and d, and (d) HRTEM image from box d, beam parallel to [2110].....	71
Fig. 4.4 The Inverse Pole Figure (IPF) maps and associated pole figures of α -Ti phase for as-received Ti-811 bar: (a) and (c) transverse to longitudinal direction – surface 1, (b) and (d) circumferential surface parallel to longitudinal direction – surface 2. Schematic illustration of surfaces 1 and 2 in Ti-811 bar is depicted in (e). R: radial direction, C: circumferential direction, and L: longitudinal direction.	72
Fig. 4.5. IPF images and associated pole figures of α -Ti phase, (a) and (c) HIPped Ti-811, (b) and (d) HIPped Ti-811 + HT860.....	73
Fig. 4.6. True stress-strain curves of the wrought Ti-811 (red), wrought Ti-811 + HT860 (pink), HIPped Ti-811 (blue), and HIPped Ti-811 + HT860 (black). Three repeat tests were carried out for all samples.....	74
Fig. 4.7. SEM secondary electron images of fracture surface of tensile test specimens at low and high magnifications: (a) and (b) wrought Ti-811, (c) and (d) wrought Ti-811 + HT860, (e) and (f) HIPped Ti-811, (g) and (h) HIPped Ti-811 + HT860. Ductile dimples are main characteristics on the fracture surface in all cases.	77
Fig. 4.8. SEM secondary electron images of fracture dimples of tensile test specimen of HIPped Ti-811 sample: (a) shear zone, (b) tear zone.....	78
Fig. 4.9. The interim SCC crack length versus time for various Ti-811 conditions in 0.1 M aqueous NaCl solution. Two repeated tests (the solid and hollow data points) for each conditions.	79
Fig. 4.10. Crack propagation velocities as a function of stress intensity factors for various Ti-811 conditions in 0.1 M aqueous NaCl solution. Two repeated tests (the solid and hollow data points) were conducted for each condition. Solid lines are polynomial fitted curves for SCC data points of different sample conditions, corresponding dashed lines indicate a band of 95% confidence level (For all solid and dashed lines, blue - HIPped Ti-811, black - Wrought Ti-811 + HT 860, green - wrought Ti-811).	80
Fig. 4.11. Fractography on crack surface of wrought Ti-811 sample (a-c): (a) High magnification secondary electron (SE) image of dimpled fracture from the pre-crack in air, (b) high magnification SE image of SCC faceted fracture, (c) low magnification SE image of SCC fracture, and the overall propagation direction is shown by the black arrow; of wrought Ti-811 + HT860 sample, and (d) high	

magnification SE image of SCC fracture. All the red arrowheads indicate the local crack propagation direction on SCC propagation facets.....	81
Fig. 4.12. SCC fractography of wrought Ti-811 + HT860 sample: (a) SE image of dimpled region fracture during the initial overload in air, (b) SE image of SCC faceted fracture surface failed in 0.1M NaCl aqueous solution.....	82
Fig. 4.13. Secondary images of crack surface for HIPped Ti-811 condition: (a) Ductile dimpled fracture to faceted failure transition at the beginning of SCC test in 0.1 M aqueous NaCl solution, and (b) high magnification image of a facet with slip bands formed steps, which are indicated by white arrowhead. All the red arrowheads indicate the local crack propagation direction on a SCC propagation facet.....	83
Fig. 4.14. (a) IPF map of α -Ti phase collected along the SCC crack path in a wrought Ti-811 sample, four microtextured regions are labeled as 1, 2, 3 and 4. In (a), the crack propagation direction is denoted by black arrow in the longitudinal direction (L) of the bar and loading direction is indicated by white arrows. (b) and (c) are associated pole figures for microtextured regions 2 and 3; Schmid factor distribution map for (d) basal $<\alpha>$, and (e) prismatic $<\alpha>$ slip systems of same area in (a). The four microtextured region are demarcated by black dashed lines.....	84
Fig. 4.15. (a) Proposed facets formation mechanism involve hydrogen enhanced localized plasticity (HELP); (b)SE image of cross section view of SCC crack tip in the wrought Ti-811 sample, feature 1 is the primary SCC crack and feature 2 is the secondary SCC cracks. The black arrow indicates the crack propagation direction.....	92
Fig. 5.1. Fractography, (a-b) of wrought Ti-811 (a) dimples on pre-crack failed in air and (b) propagation SCC facets fractured in 0.1M aqueous NaCl solution; (c-d) of HIPped Ti-811 sample (c) propagation SCC facets fractured in 0.1M aqueous NaCl solution and (d) localized slip band observed on facets in white dashed line box in (c).....	96
Fig. 5.2 (a-f) FIB lift-out lamellae obtained from a fractured wrought Ti-811 sample, (a) and (b) from pre-crack dimpled fracture, (d) and (e) from SCC faceted fracture. Pole figures of α phase, (c) the pole figure corresponding to region 1 in (b), (f) the pole figure corresponding to region 2 in (e). (g-i) FIB lift-out lamella obtained from a fractured HIPped Ti-811 sample, (g) and (h) from SCC faceted fracture, and the insert in (h) is an enlarged view of region 3; (i) the pole figure corresponding to region 3 in (h). All the fracture surfaces beneath the platinum (Pt) deposition are denoted by the black arrowheads, and all the red arrows denote the tensile direction in (b), (e) and (h).....	98
Fig. 5.3. Bright Field (BF) TEM micrographs of region 1 lift-out from the pre-crack dimples of wrought Ti-811 in Fig. 5.2b. Low magnification (a) $g = [0002]$, high magnification (b) $g = [0002]$, the white arrowheads indicate two planar slip bands, (c) $g = [0111]$, the black arrowhead denotes a grain boundary at bottom right, $B \approx [2110]$. In all case black arrow indicates the excited g vector.	102
Fig. 5.4. BF TEM micrographs of region 2 lift-out from the SCC facets of wrought Ti-811 sample in Fig. 5.2e. (a) BF image when $g = [0002]$ is excited, the black arrowhead denotes the secondary crack tip which is previously illustrated in Fig. 5.2 (e); (b) BF image when $g = [0111]$ is excited, white arrowhead indicates a sub-grain boundary; (c) Selective area diffraction (SAD) pattern taken from the yellow circle in (b). $B \approx [2110]$. In all case black arrow indicates the excited g vector.	103
Fig. 5.5. BF TEM micrographs of region 3 lift-out from the SCC facets of HIPped Ti-811 sample in Fig. 5.2h. (a) $g = [0002]$, (b) $g = [2112]$, (c) proposed steps formation mechanism on facets in α grain. The white arrowheads indicate the linear $<c+a>$ segments resided on the (2112) plane, and the black arrowhead denotes a step on facet surface. $B \approx [0110]$, In all case black arrow indicates the excited g vector.	104

Fig. 5.6. (a) BSE SEM image of the fully lamellar IMI834 alloy in the study of [87], (b) BSE SEM image of the wrought Ti-8Al-1Mo-1V alloy with a bi-modal microstructure used in the current study, (c) BSE SEM image of the HIPped Ti-8Al-1Mo-1V alloy used in the current study.	107
Fig. 5.7. BF TEM micrographs of (a) region 2 lift-out from the SCC facet of wrought Ti-811 sample in Fig. 5.2e, and the black arrow head indicates the secondary crack tip, $B \approx [2110]$, (b) region 3 lift-out from the SCC facet of HIPped Ti-811 sample containing the surface steps in Fig. 5.2h, $B \approx [0110]$, (c) region 4 lift-out from the SCC facet of HIPped Ti-811 sample in Fig. 5.2h, $B \approx [0110]$. The main fracture surface is below the Pt deposition in all cases, and trace of $(0002)_\alpha$ planes are indicated by the SAD patterns.	111
Fig. 5.8. Illustration of a hybrid aqueous NaCl SCC mechanism including absorption induced dislocation emission (AIDE) and hydrogen enhanced localized plasticity (HELP) for Ti-8Al-1Mo-1V. H_{abs} is the absorbed hydrogen.....	113

LIST OF TABLES

Tab. 1.1 Slip systems in HCP α titanium [8, 9]	14
Tab. 1.2 Relevant electrochemical reactions of Ti-H ₂ O system in the range of open circuit potential in Fig. 1.15 [53].....	25
Tab. 1.3 The frequency factor (DH_0) and activation energy (Q) for α and β titanium alloys [87, 88].	50
Tab. 3.1. Descriptions of various Ti-811 samples studied.....	59
Tab. 3.2. The chemical composition of various tested samples.....	60
Tab. 4.1 Summary of tensile properties for various Ti-8Al-1Mo-1V samples.....	75
Tab. 4.2 Threshold stress intensity for various Ti-8Al-1Mo-1V samples.	81
Tab. 5.1. Schmid factors, relative CRSS and relative critical tensile stress for various slip systems for the interested regions of FIB lift-out lamellae in Fig. 5.2b, e and h.	100
Tab. 5.2. Crystallographic orientations of SCC facets investigated in Fig. 5.7.	112

CHAPTER I: LITERATURE REVIEW

1.1 Introduction

Limited resources and growing demands lead to an increasing expense of fuel, which then results in a high cost in transportation. In addition to the fuel cost, the growing concerns on greenhouse gas emissions give motivations in reduction of the fuel consumption in aerospace [1-7]. In order to increase the fuel efficiency, weight reduction in aerospace vehicles is desirable. For example, the tolerances of extra cost to achieve weight reduction are about 1 and 10 Euro per Kg for the aircraft and spacecraft applications respectively [1]. As a result, weight reduction and associated fuel efficiency improvement, play a significant role in aerospace materials selection.

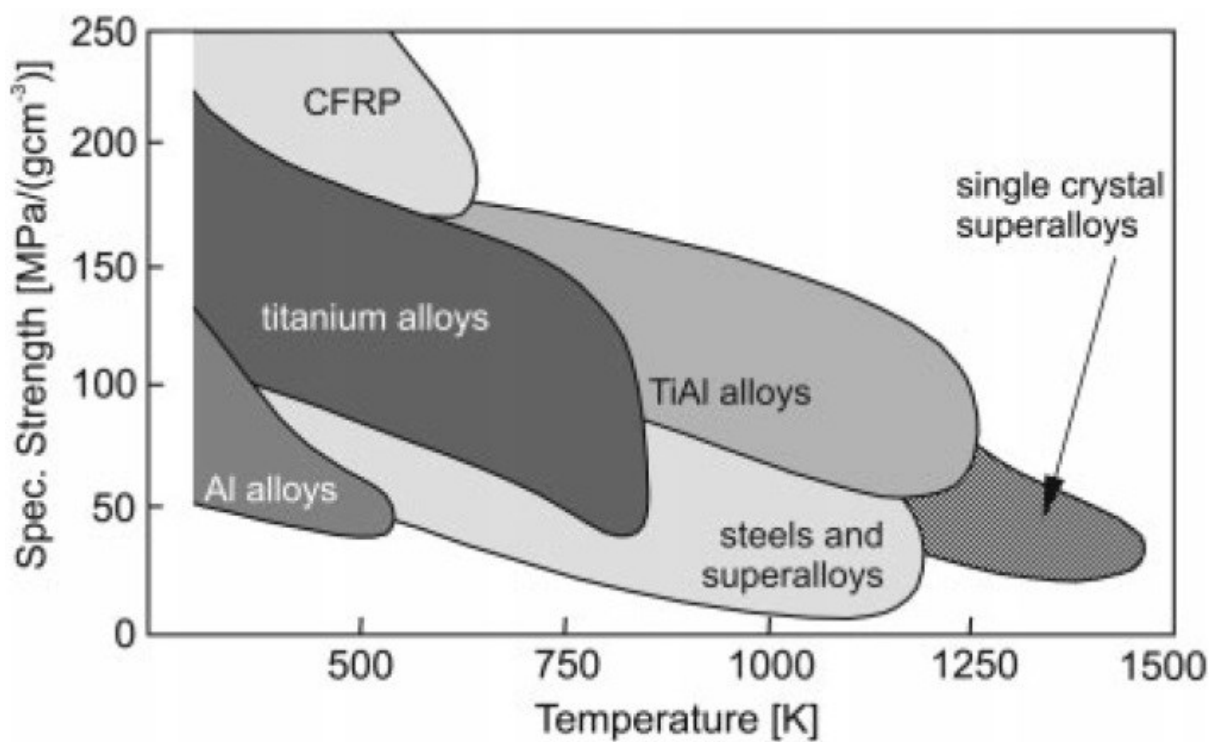


Fig. 1.1 Specific strength and operating temperature of various materials [8]

There are several methods to reduce component weight: the use of lower density materials, or the use of materials with increased strength and/or stiffness [1, 5, 7]. Materials with a higher specific strength (strength/density) has a relatively higher strength and lower density. Therefore,

a high specific strength contributes positively to weight reduction. As shown in Fig. 1.1, Ti alloys and TiAl alloys have a higher specific strength comparing to that of Al alloys, steels and super alloys. Although carbon fibre reinforced plastics (CFRP) have the highest specific strength, Ti alloys, which can be used up to 500 °C, are more attractive comparing to CFRP at temperatures above 300°C (Fig. 1.1) [9]. In addition to the high specific strength, Ti alloys have a good creep strength up to about 550 °C and an excellent corrosion resistance. All these standout properties make them desired in aerospace applications.

Ti-8Al-1Mo-1V (Ti-811) alloy has the highest elastic modulus (stiffness) among all the commercial Ti alloys, which is desirable for the component weight reduction and aircraft fuel efficiency improvement. In addition to weight reduction, materials with a high elastic modulus are favourable for jet engine applications. Ti-811 has a similar tensile strength to that of Ti-6Al-4V (Ti-64) at room temperature [8, 10-12]. But it has a slightly lower density than that of Ti-64, which results in a higher specific strength in turn. Therefore, Ti-811 with a high elastic modulus and specific strength is suitable in the mass reduction point of view.

Back to the 1960s, Ti-811 was contemplated to be applied as the sheet structure in the American supersonic transport (SST) project, but it had been found to have a severe stress-corrosion cracking (SCC) susceptibility. The SCC was attributed to a localized, planar slip due to the presence of ordered Ti_3Al (α_2) precipitates in α phase of Ti-811[13]. In addition to α_2 precipitates, crystallographic texture had been reported to influence the SCC properties in numerous $\alpha+\beta$ Ti alloys [10, 11, 14-18].

However, all the previous studies were only focused on conventional thermomechanical processed materials (eg. wrought Ti-811) with an intrinsic texture, and the discussion of texture effects was on a macroscale. In addition, the degree of effect of the α_2 phase and texture on SCC was not delineated independently. With the development of material processing and

characterization technologies; hot isostatic pressing (HIPping) allows the preparation of isotropic materials without crystallographic texture, and electron backscatter diffraction (EBSD) provides a way to characterize microtexture. In this project, the effect of α_2 phase will be studied in hot isostatic pressed (HIPped) samples without the influences of crystallographic texture, and the effect of microtexture will also be investigated and discussed in samples without the presence of α_2 precipitates. Although several SCC mechanisms have been reported in Ti alloys, which will be reviewed in section 0. But the SCC mechanism has still not be clearly established for Ti-8Al-1Mo-1V, thus understanding of SCC mechanism is also focused in this work.

1.2 Metallurgy of Titanium Alloys

The fundamental concepts of titanium alloys, including crystallographic structures, phase diagrams, alloy elements, phase transformations, classifications of Ti alloys, will be described in this section.

1.2.1 Phase Diagram and Crystal Structures

As illustrated by the phase diagram in Fig. 1.2, α phase is stable at low temperatures, while β phase is the stable phase at high temperatures. The β/α allotropic transformation temperature and melting temperature are around 882 °C and 1670°C respectively in pure titanium. As shown in Fig. 1.3, α phase has a hexagonal closed packed (HCP) crystal structure, which has the most densely packed (0001) plane and three $<11\bar{2}0>$ directions as the most densely packed directions. While β phase is a body centered cubic (BCC) crystal structure, and it has six {110} planes and four $<111>$ directions as the most densely packed planes and directions respectively [8, 9, 19].

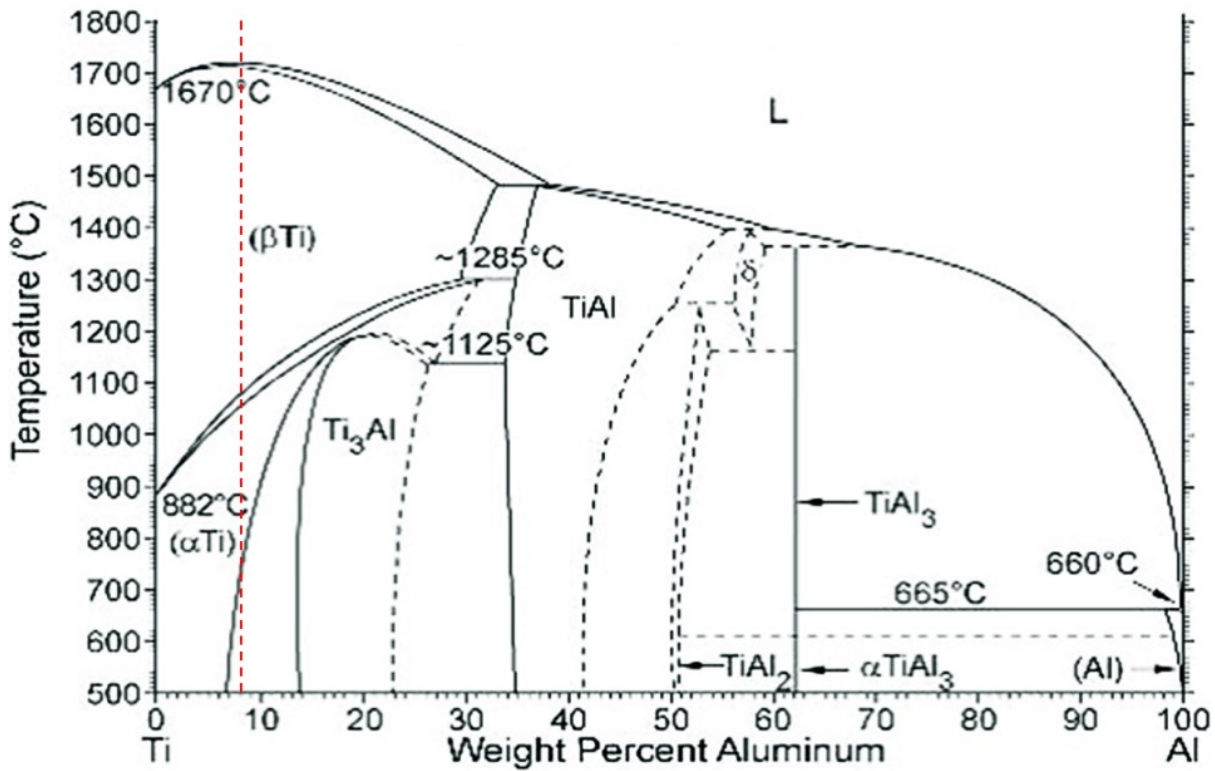


Fig. 1.2 Ti-Al Binary phase diagram. The highlighted red dashed line denotes 8 Wt. % Al composition. [8, 9]

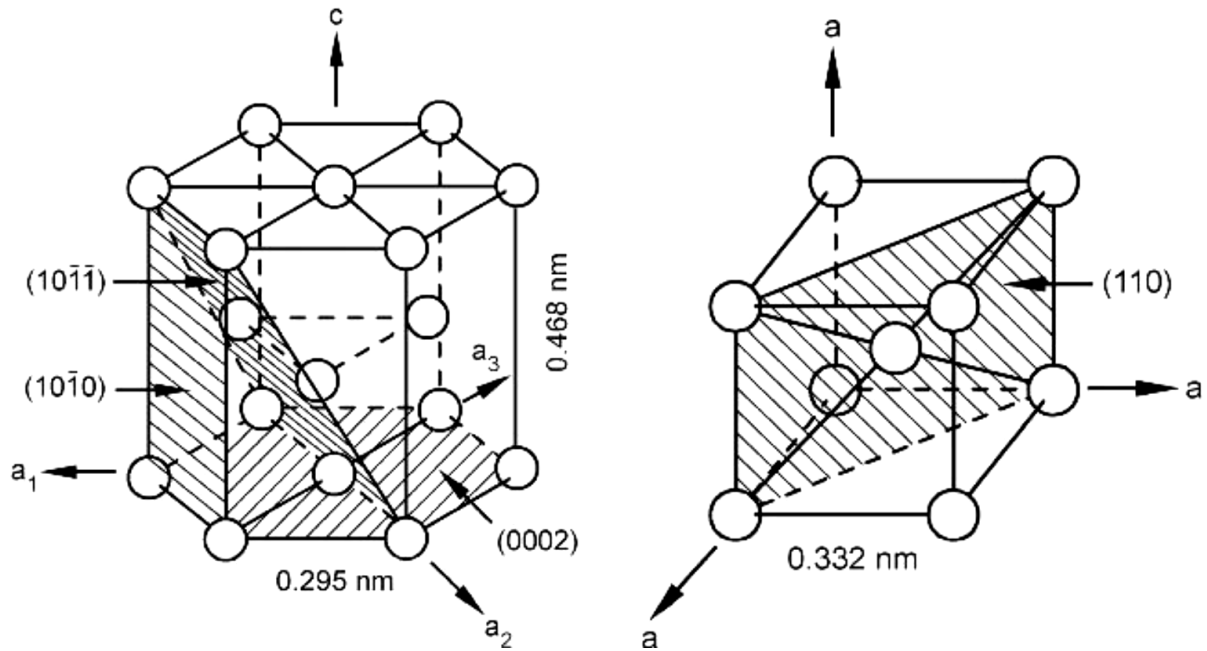


Fig. 1.3 Crystal structure of α and β phases of Titanium [8]

α titanium has an anisotropic mechanical behaviour, which is resulted from the inherent anisotropy of HCP crystal [8, 9]. For example, the elastic modulus is the highest when the loading direction parallel to the [0001] direction. While, it is the lowest when the stress is

applied parallel to the (0001) plane [8, 9]. Similar anisotropic effects has been observed on shear modulus [8].

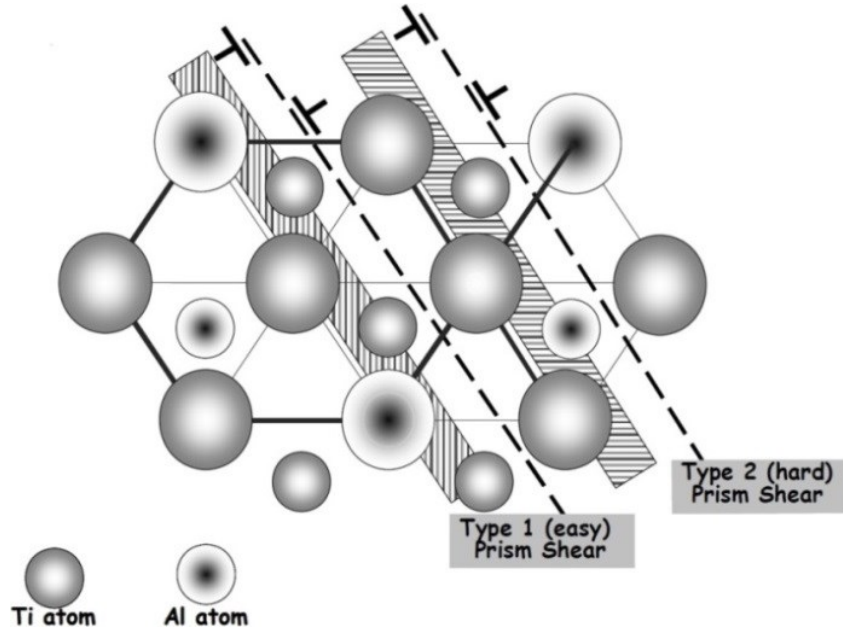


Fig. 1.4 D019 crystal structure of Ti_3Al (α_2) phase [8]

In Ti alloys, the α_2 precipitation can be occurred when Al content exceeding 5 Wt. %. As indicated by the Ti-Al binary phase diagram in Fig. 1.2, 8 Wt. % Al (the red dashed line) leads to the precipitation of α_2 (Ti_3Al) phase at appropriate temperatures. The α_2 precipitate is ordered and coherent in α phase, and it has a hexagonal D0₁₉ superlattice structure illustrated in Fig. 1.4. The small atoms are in the plane above the basal plane, and Ti and Al atoms occupy specific positions in the ordered superlattice [8-10, 20, 21]. Ordering alters lattice parameter for α_2 phase, in which it is doubled on basal plane compared to that of α phase, but it remains the same on the c axis.

1.2.2 Alloying Elements

For Ti alloys, there are two main groups of alloy elements, which are α or β stabilizers. α stabilizing elements increase the β/α allotropic transformation temperature and extend α phase field to higher temperatures. Whereas β stabilizers decrease the transus temperature and stabilize the β phase at lower temperatures.

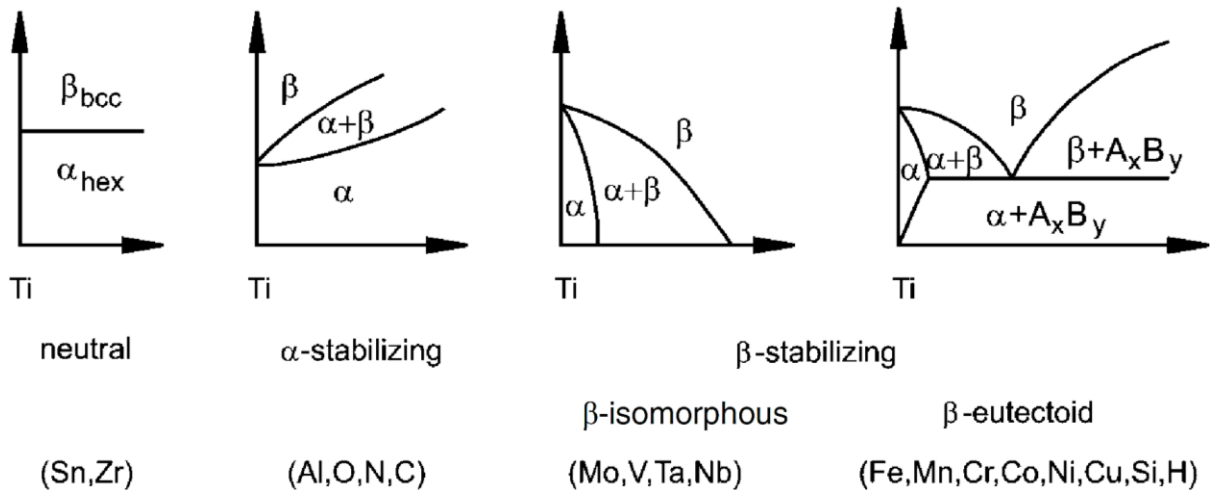


Fig. 1.5 Effects of alloying elements on phase diagram for Ti alloys [8, 9]

As shown in Fig. 1.5, common α stabilizers include substitutional element Al and interstitial elements O, N, and C. Al is the only common metallic α stabilizer and has a high solubilities in titanium, thus it is the most widely used alloying elements. In the Ti-Al binary phase diagram (Fig. 1.2), intermetallic phases, like Ti_3Al (α_2), $TiAl$ (γ), $TiAl_2$, and $TiAl_3$, are formed with increasing Al contents [8, 9]. The effect of other α stabilizers can be expressed by an equivalent Al contents as the following equation [8]:

$$[Al]_{eq} = [Al] + 0.17 [Zr] + 0.33 [Sn] + 10 [O] \quad (1.1)$$

It shows that O is a very strong α stabilizer, and it is also an α_2 stabilizer that extends $\alpha+\alpha_2$ phase field to higher temperatures and promotes the ordering transformation.

β stabilizers can be divided in to β -isomorphous elements and β -eutectoid forming elements groups depending on the resultant phase diagram, and both of them are illustrated in Fig. 1.5. β -eutectoid forming elements include the widely used Cr, Fe, and Si. It is worthwhile to mention that hydrogen is one of β -eutectoid forming elements. Hydrogenation /dehydrogenation (HDH) process is a grain refinement treatment used in Ti alloys, which utilizes the combined effects of the high diffusivity of hydrogen and low eutectoid temperatures when hydrogen is added in Ti alloys [8]. Hydrogen has a much higher diffusivity and solubility

in β phase compared to α phase due to the low packing density in BCC crystal [22]. But the usage of hydrogen is limited to about 150 ppm due to hydrogen embrittlement [22]. The other group is the β -isomorphous elements that contains Mo, V, Ta, and Nb. High concentrations of β -isomorphous alloying additions can stabilize the β phase to room temperature. The overall effect of β stabilizers can be quantitatively described as the following equivalent Mo content [8]:

$$[\text{Mo}]_{\text{eq.}} = [\text{Mo}] + 0.2 [\text{Ta}] + 0.28 [\text{Nb}] + 0.4 [\text{W}] + 0.67 [\text{V}] + 1.25 [\text{Cr}] + 1.25 [\text{Ni}] + 1.7 [\text{Mn}] + 1.7 [\text{Co}] + 2.5 [\text{Fe}] \quad (1.2)$$

In addition to α and β stabilizing elements, neutral alloying elements is another group, which contains Sn and Zr. Neutral alloying elements have a minor effect on the transus temperature [8-10, 20]. However, Sn can replace Al in the hexagonal ordered Ti_3Al superlattice. Therefore, it behaves as an α stabilizer. This explains the presence of Sn in equivalent Al contents described Equation 1.1.

1.2.3 Phase Transformations

Slow cooling from β to α phase field results in the β/α allotropic transformation, governed by diffusion, nucleation, and growth processes. The transformation between the HCP α and BCC β phases obeys the following Burgers relationship [8, 9]:

$$(110)_{\beta} \parallel (0002)_{\alpha}$$

$$<1\bar{1}1>_{\beta} \parallel <11\bar{2}0>_{\alpha}$$

Based on the Burgers relationship, a bcc crystal can have 12 hexagonal variants during the transformation. Because there are six most densely packed $(110)_{\beta}$ planes and two $<1\bar{1}1>_{\beta}$ directions for each plane in the BCC β titanium unit cell. Fig. 1.6 illustrates the lattice distortion during the transformation, the distance between $(0001)_{\alpha}$ planes is slightly larger than that of

$(110)_{\beta}$ planes, which introduces a contraction on c -axis and gives a reduced c/a ratio for HCP α titanium. The transformation is also accompanied with a slight volume increase [8, 9]. In HCP crystal, the ideal c/a ratio is 1.633, but α titanium has a slightly low c/a ratio at 1.587 according to the lattice parameters in Fig. 1.3 [8, 9].

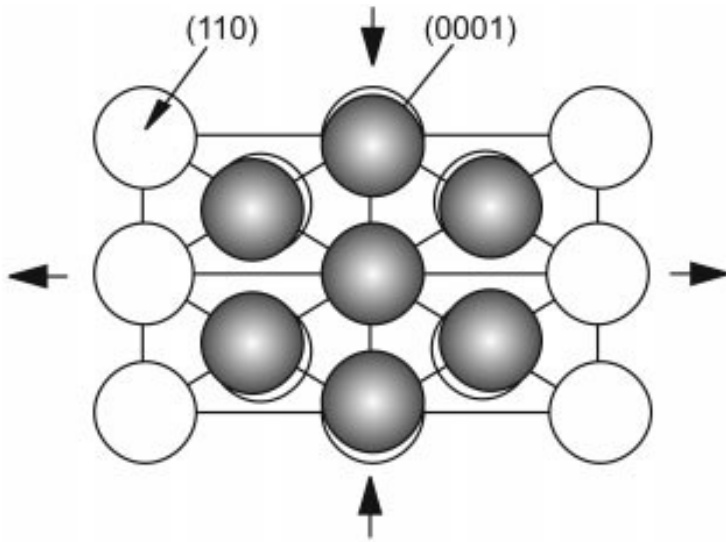


Fig. 1.6 Burgers relationship between BCC (β) and HCP (α) crystals during the β/α phase transformation [9]

Rapid cooling from temperatures above the martensitic start temperature (M_s) results in a diffusionless martensite transformation. Although it involves shear transformation systems of $[111]_{\beta}$ ($11\bar{2}\right)_{\beta}$ and $[111]_{\beta}$ ($\bar{1}01\right)_{\beta}$, the martensite transformation still obeys the Burgers relationship. Similar to the β/α allotropic transformation temperature, the martensitic start temperature is also influenced by alloying elements. It increases with the addition of α stabilizers, and decreases with increasing contents of β stabilizers [8, 9]. Only a small elastic distortion of titanium martensite HCP crystal is induced by interstitial oxygen atoms, while interstitial carbon and nitrogen atoms introduce a strong distortion in BCC lattice of martensite in steels with accompanying significant increase of strength. Therefore, the martensite is much softer in titanium than it is in steel [8, 9].

The martensite can be divided into hexagonal α' martensite and orthorhombic α'' martensite, and both of them decompose into α and β phases upon annealing in the $\alpha+\beta$ phase field [8, 9].

The hexagonal α' martensite has two kinds of morphologies, which includes the massive martensite and “acicular” martensite. The Massive martensite is the form in pure titanium or titanium alloys with a low solute concentration. While the “acicular” martensite is the type in titanium alloys with a higher solute content [8, 9].

α'' martensite is formed when the solute contents are further increased, which introduces a change in crystal symmetry from hexagonal into orthorhombic. An example is that α' is changed into α'' when there is 4 Wt. % Mo in the binary Ti-Mo system [8].

1.2.4 Classification of Titanium Alloys

Fig. 1.7 divides titanium alloys into α , $\alpha+\beta$, and β alloys by β stabilizer concentration contained. The group of α alloys consists of commercial pure (CP) titanium and titanium alloys with a very low β stabilizer addition. Another group is $\alpha+\beta$ alloys, which have a field from α alloys boundary to the intersection point between the M_s dashed line and room temperature. A subcategory of $\alpha+\beta$ alloys is near α alloys, which contains only 1-2% β stabilizers but a large amount of α stabilizers. Therefore, near α alloys have a small volume of stable β phase (less than about 10 Vol%) and a high β transus temperature [8, 9].

β alloys have a high concentration of β stabilizers, and they can be further broken down into metastable and stable β alloys. The stable β alloys is the single phase field, which do not exist as a commercial products. Thus the β alloys is generally used to describe the metastable β alloys. As the M_s temperatures are below the room temperature, there is no martensite transformation in the β alloys [8, 9].

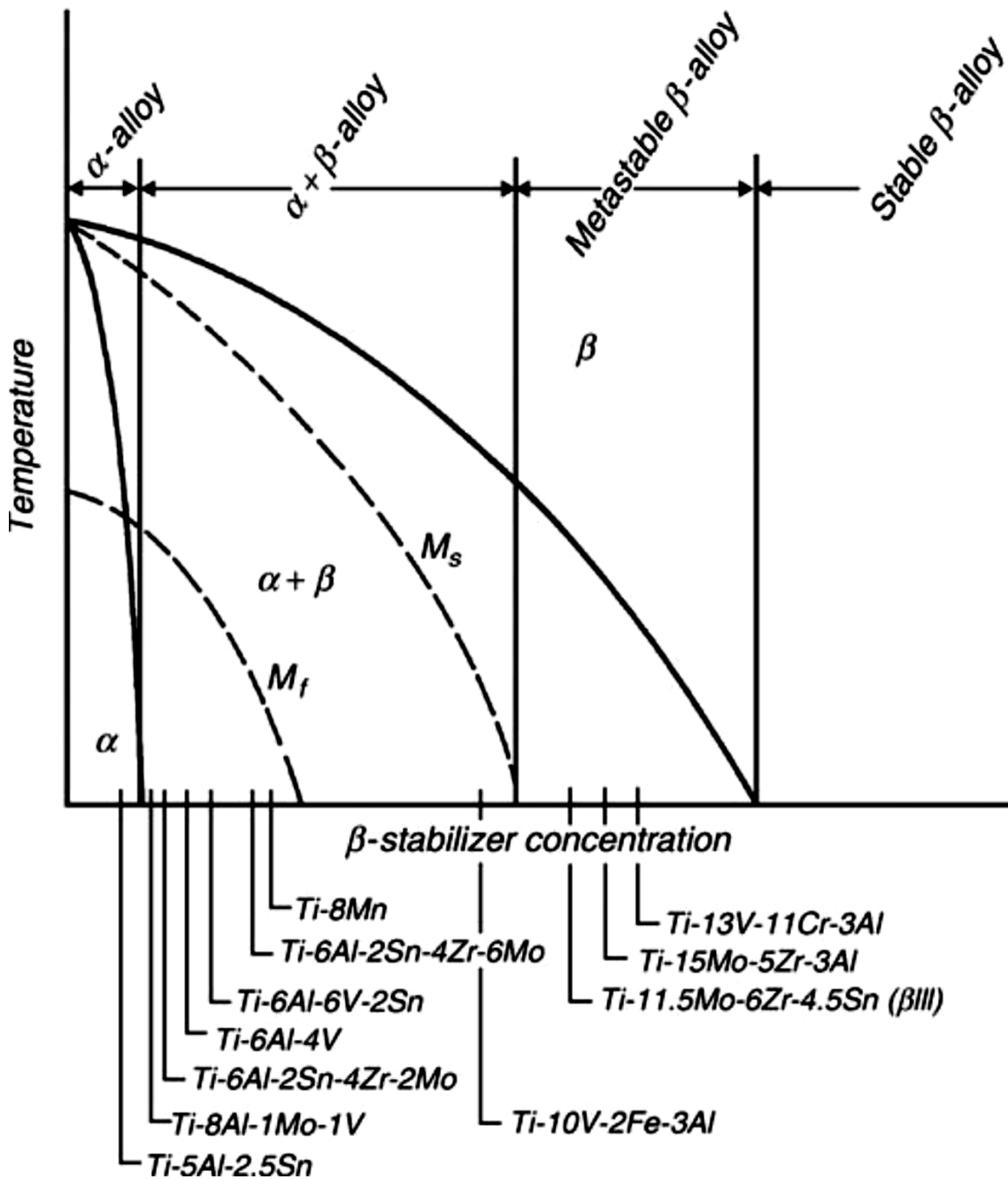


Fig. 1.7 Pseudo-binary β -isomorphous phase diagram [24]

In this work, the studied material is Ti-8Al-1Mo-1V alloy, which belongs to the near α alloys subgroup. Near α alloys have a combination of high strength and good creep resistance, and they are widely used in high temperature aero-engine applications. For Ti-8Al-1Mo-1V, 8 Wt. % Al contents reduce the alloy density to 4.37 g/cm^3 , which is slightly lower than that of Ti-6Al-4V (4.43 g/cm^3). High Al contents also give Ti-8Al-1Mo-1V the highest elastic modulus, 120 GPa, among conventional titanium alloys. The effect of Al on elastic modulus is related to

ordering and accompanied increase of covalent bonding strength [8, 10, 11]. In addition to α , β and α_2 phases, α' , α'' , and ordered ω phases, are possible phases in Ti-8Al-1Mo-1V. The hexagonal α' and orthorhombic α'' martensite are formed when it is quenched from different temperature regions above the M_s at 900 °C [8, 10, 11, 25]. For metastable ω phase, both athermal and isothermal ω phases have a hexagonal symmetry in leaner alloys. Similar with α_2 phases, ω precipitate is also coherent and can be shearable by dislocations [8, 10, 13].

As Ti-8Al-1Mo-1V has a high elastic modulus and a specific strength, it seems to be an extremely attractive material for aerospace applications. However, it was found to have a limitation of stress-corrosion cracking (SCC). As a result, Ti-8Al-1Mo-1V can only be applied in non-corrosive environments. The main applications of Ti-8Al-1Mo-1V are airframes and gas turbine engines, which are driven by the property of high elastic modulus. To be more specific, gas turbine engine applications are compressor blades and vanes, and other applications include mechanical and screw presses, and rapid strain rate hammers [8, 10-12].

1.3 Deformation Behaviours

There are four common presented phases, α , β , α_2 phases and martensite, in Ti-8Al-1Mo-1V. In this section, the concept of Schmid factor and deformation modes of the four common phases are introduced.

1.3.1 Schmid Factor

In crystalline material, the ease of dislocation motion is different on different slip systems. Generally, there are preferred slip systems with specific slip planes and directions [26, 27]. In single crystal, activation of slip systems is influenced by the magnitude of the shear stress, geometry of crystal, and orientation between the active slip plane and shear stress. The resolved shear stress is various for different slip systems, because it depends on the orientation between

the stress axis relative to slip plane normal (ϕ) and slip direction (λ) respectively (see Fig. 1.8).

The resolve stress is given by [26, 27]:

$$\tau_R = \frac{F}{A} \cos \phi \cos \lambda = \sigma m \quad (1.3)$$

where F is the applied stress, A is the cross section area. The ratio between the critical resolved shear stress (τ_{CRSS}) and axial stress is the Schmid factor; $m = \cos \phi \cos \lambda$, which is maximal at 0.5 when $\phi = \lambda = 45^\circ$. Slip cannot be activated when either ϕ or λ equal to 90° , which has the tension axis either parallel to the slip plane or normal to the slip direction. As a result, crystal fracture occurs rather than having a plastic deformation in the above two extreme conditions [8, 26, 27]. A specific slip system of single crystal is initiated when the resolved shear stress reaches the τ_{CRSS} , and it is a property that determines when yielding occurs: $\sigma_y = \tau_{CRSS}/(m)_{max}$ [26, 27].

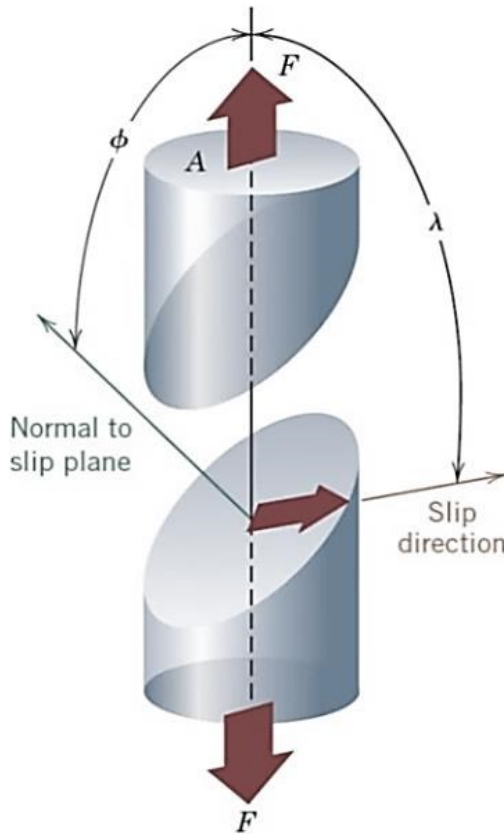


Fig. 1.8 Diagram of calculating critical resolve shear stress [26]

1.3.2 Deformation Modes of α Phase

In HCP α titanium, four slip planes with various slip directions are depicted in Fig. 1.9, and these slip systems are summarized in Tab. 1.1. For $\langle a \rangle$ type slip, the slip directions are three close packed $\langle 11\bar{2}0 \rangle$ directions. The corresponding $\langle a \rangle$ type slip planes are the (0002) , three $\{10\bar{1}0\}$, and six $\{10\bar{1}1\}$ planes. But there are only 4 independent slip systems, because the combination of a $\langle a \rangle$ type slip on the (0002) and $\{10\bar{1}0\}$ planes leads to the same shape change of a $\{10\bar{1}1\}$ $\langle a \rangle$ type slip [8, 9].

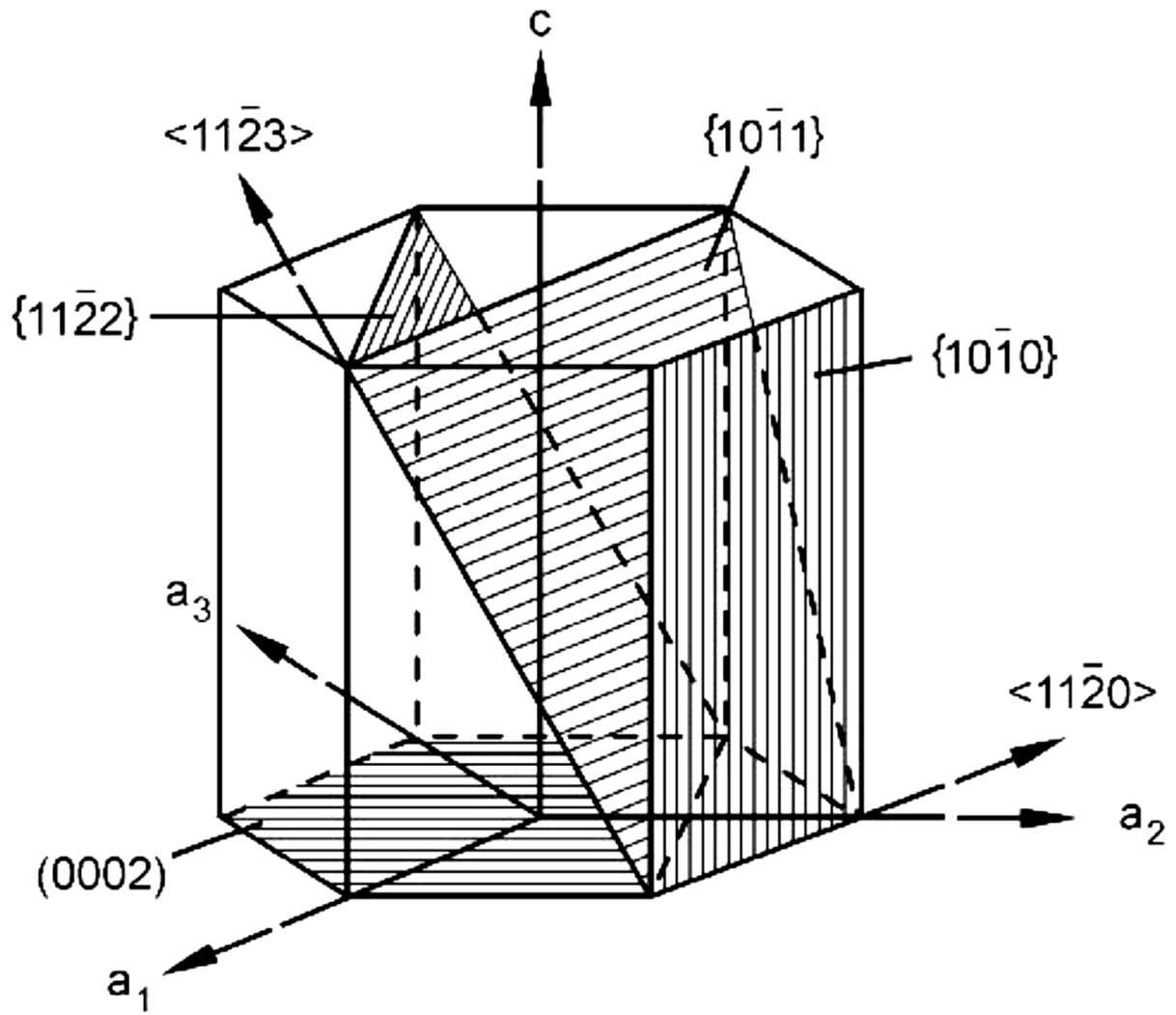


Fig. 1.9 Slip planes and directions of HCP α titanium [8]

According to the von Mises criterion, at least five independent slip systems are required for a homogeneous plastic deformation in polycrystalline materials. As mentioned in the above paragraph, there are only four independent $\langle a \rangle$ type slip systems. Thus a non- $\langle a \rangle$ type slip

system is needed to achieve a homogeneous plastic deformation. In literature, $\langle c + a \rangle$ type dislocations were observed by TEM in titanium alloys [8, 9]. There are two kinds of $\langle c + a \rangle$ slip, which are either on $\{10\bar{1}1\}$ or on $\{11\bar{2}2\}$ planes, and $\{11\bar{2}2\} \langle 11\bar{2}3 \rangle$ slip is more commonly observed [8, 9].

Tab. 1.1 Slip systems in HCP α titanium [8, 9]

Slip systems type	Burgers vector	Slip direction	Slip plane	No. of slip systems	
				Total	Independent
I			(0002)	3	2
II	$\langle a \rangle$	$\langle 11\bar{2}0 \rangle$	$\{10\bar{1}0\}$	3	2
III			$\{10\bar{1}1\}$	6	4
IV	$\langle c + a \rangle$	$\langle 11\bar{2}3 \rangle$	$\{11\bar{2}2\}$	6	5

Fig. 1.10 shows the influence of temperatures on the critical resolved shear stress (τ_{CRSS}) for $\langle a \rangle$ and $\langle c + a \rangle$ type slip systems in a Ti-6.6Al single HCP α crystal. The τ_{CRSS} ratio of basal $\langle a \rangle$, prismatic $\langle a \rangle$, and pyramidal $\langle c + a \rangle$ slip systems is about $0.2625 : 0.2375 : 1$. $\langle c + a \rangle$ slip has a τ_{CRSS} at 800 MPa, which is 4 times of that for $\langle a \rangle$ slip (about 200 MPa) at room temperature (300K), but the difference of τ_{CRSS} between $\langle a \rangle$ slip systems is small. Therefore, it requires a much higher stress to activate $\langle c + a \rangle$ slip. The percentage of $\langle c + a \rangle$ type deformation is quite low when there is no crystallographic texture, and $\langle a \rangle$ slip is preferred due to the easier activation [8]. For $\langle a \rangle$ type slip, τ_{CRSS} of prismatic and basal slip systems are about 190 MPa and 210 MPa respectively at room temperature. This indicates that the prismatic slip is the most favourite slip type [8, 9, 28]. As the c/a ratio in α titanium is 1.587, which is smaller than the ideal ratio at 1.633. The reduction of the c/a ratio leads to a packing density increase on the prismatic planes relative to the basal plane, which changes the favouring slip systems from basal $\langle a \rangle$ slip to prismatic $\langle a \rangle$ slip in titanium [8, 9].

Alloying elements concentration can influence the slip modes, and an example is the Ti-Al binary system [28, 29]. An increase in slip planarity is resulted from increased Al alloy concentration due to the solute partitioning effect [30]. In addition, the α_2 precipitation will be promoted when Al content exceeding 5 Wt. %. The effects of α_2 precipitates on slip behaviours in α titanium single crystals have been investigated in the same study. Although the effect of α_2 on τ_{CRSS} is negligible, it also promotes planar slip [28-30].

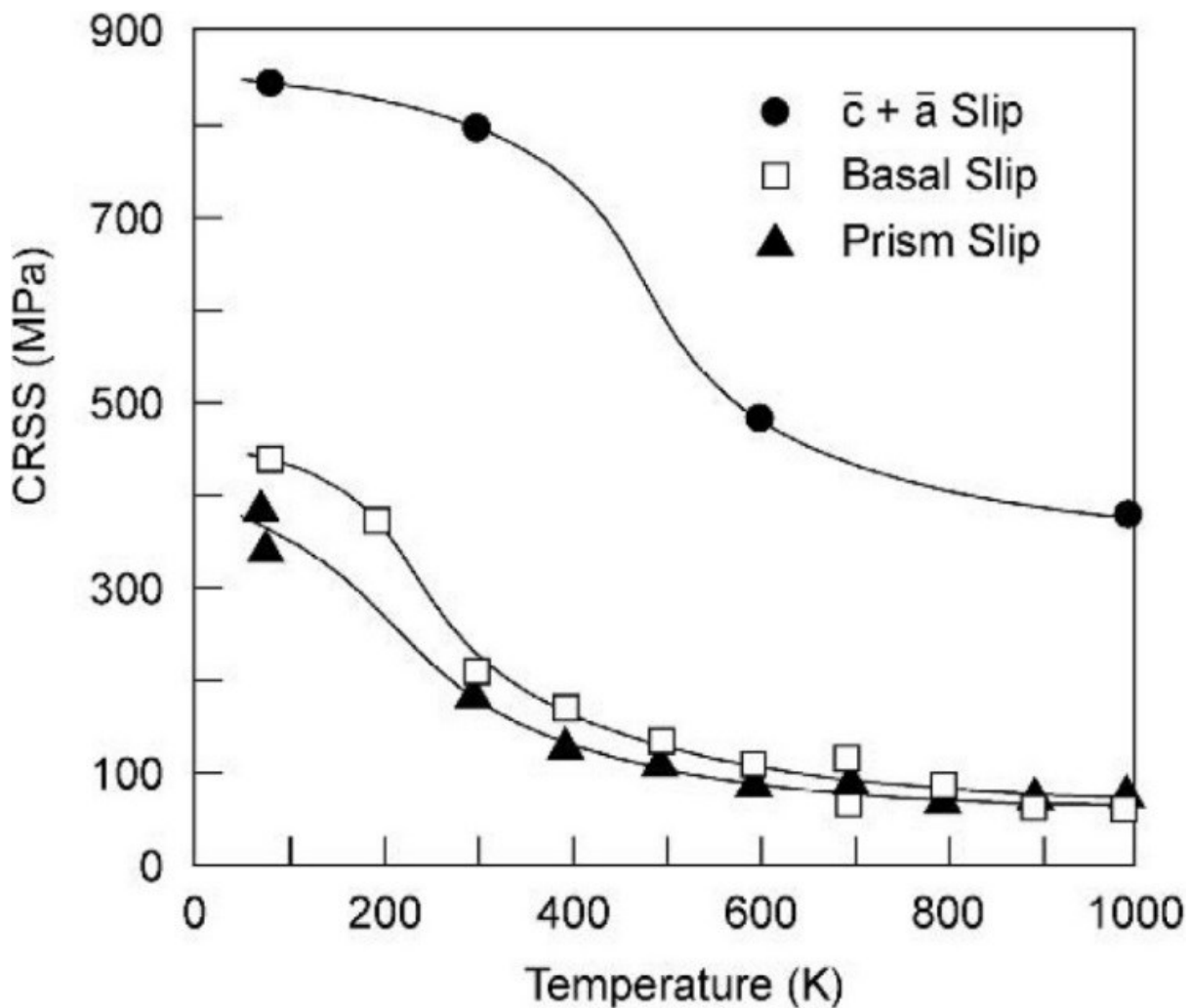


Fig. 1.10 Influence of temperature on CRSS for slip systems with $\langle a \rangle$ and $\langle c + a \rangle$ Burgers Vectors in single crystal of Ti-6.6Al [8]

In addition to slip, twinning is another observed deformation mode in CP titanium and α titanium alloys. The main twinning elements are $\{10\bar{1}2\}$, $\{11\bar{2}1\}$, and $\{11\bar{2}2\}$. However, the occurrence of twinning is suppressed nearly entirely in $\alpha+\beta$ titanium alloys due to the small

dimensions of phases, increased solute content, and precipitation of α_2 phase [8]. Although Ti-8Al-1Mo-1V is a near α alloy, it is still a sub-class of $\alpha+\beta$ titanium alloys. Twinning would be expected to be significantly suppressed due to the high solute concentration in Ti-8Al-1Mo-1V.

1.3.3 Deformation Modes of β Phase

In β phase, $\{110\}$, $\{112\}$, and $\{123\}$, with the same Burgers vector of the $\langle 111 \rangle$ are main slip systems [8], which are general slip systems in bcc metals. As the energy for plastic deformation is proportional to the minimal slip length, which is shorter in the BCC β phase compared to that of HCP α phase. Therefore, the plastic deformation is much easier in BCC β titanium than in α titanium [9].

In addition to the dislocation slip, the twinning is also observed in β phase. However, twinning is limited to single β phase condition and the propensity decreases with increasing solute contents. In heat-treated hardened β alloys, it is totally suppressed in the presence of α precipitation.

1.3.4 Deformation Modes of α_2 Precipitates

In the intermetallic TiAl alloys, ordering influences the deformation mode. Fig. 1.4 shows that basal slip by a $\langle a \rangle$ Burger vector introduces disorders, thus basal $\langle a \rangle$ slip is difficult. However, prismatic slip is easier compared to basal slip, and there are two types of prismatic shear in Fig. 1.4. The operation of type 1 prismatic shear is easier in comparison to that of the type 2 due to the creation of two wrong nearest neighbour atoms in type 2. The $\langle c+a \rangle$ slip has an $\langle a \rangle$ component, which makes it difficult in D0₁₉ crystal structures [8].

However in the Ti-6.6Al alloy, α_2 precipitates do not have any noticeable effects on the value of τ_{CRSS} for different $\langle a \rangle$ type systems. The operation of basal $\langle a \rangle$ and prismatic $\langle a \rangle$ slip systems are depending on the grain orientation and stress axis. $\langle c+a \rangle$ type slip is also observed

when the grain is not orientated favourably for the $\langle a \rangle$ type slip [28]. T. R. Cass showed that high Al content can increase the propensity of $\langle c + a \rangle$ slip in a comparison between Ti-3Al and Ti-7Al crystals [31].

In addition to the slip type operated, α_2 precipitates have a pronounced effect on the slip character. Cross slip is suppressed by ordering; which promotes coarse planar slip bands. These planar slip increase the effective slip length and therefore affects mechanical properties. As shown in Fig. 1.11, the α_2 precipitates can be destroyed completely inside the coarse slip band [28]. In general, alloys with the α_2 precipitation have a low ductility due to the promoted planar slip [8].

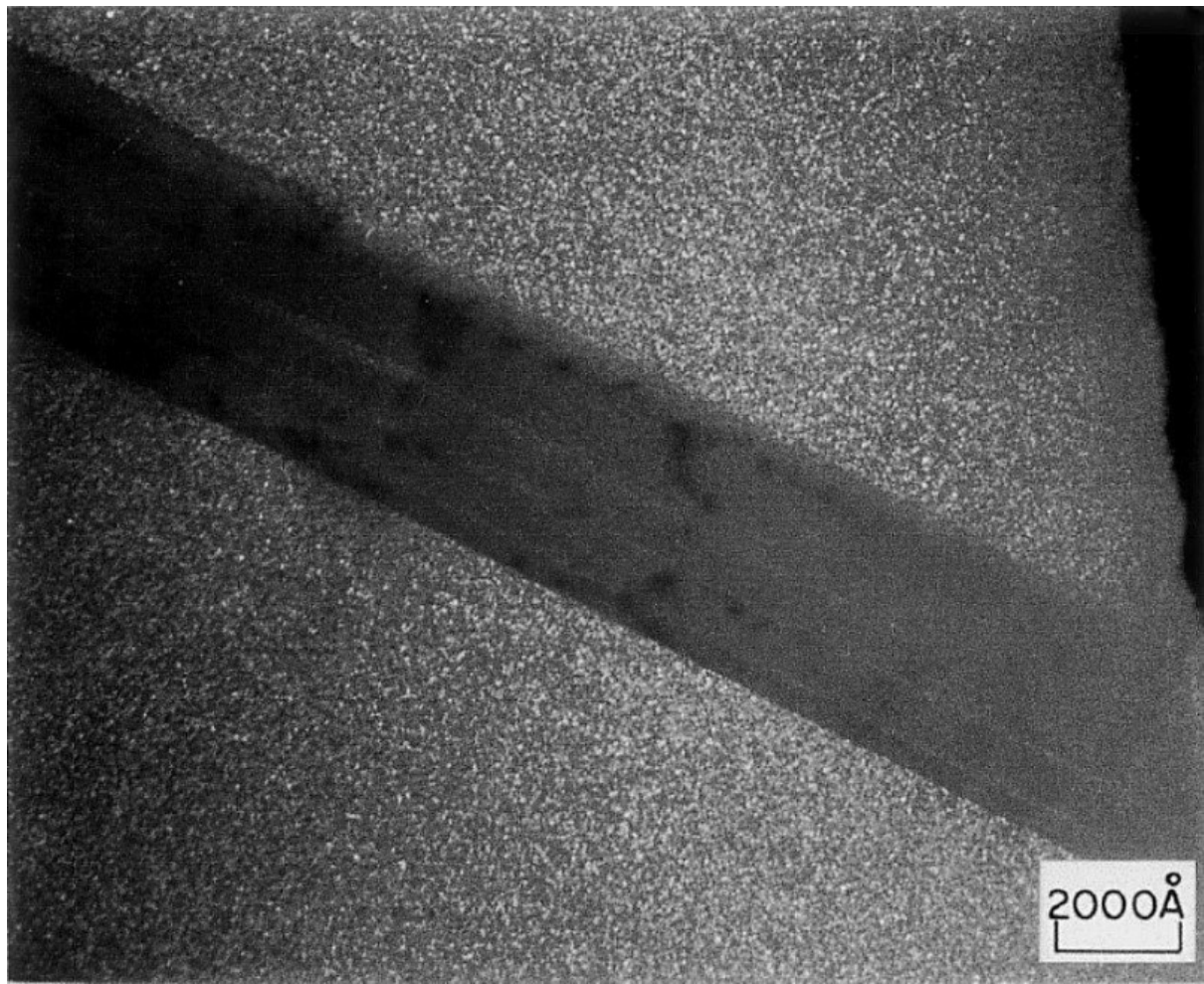


Fig. 1.11 Dark-field TEM image shows a slip band, in which the α_2 precipitates are destroyed in a Ti-6.6Al crystal, $B=\{10\bar{1}1\}$ [28].

1.3.5 Deformation Modes of Martensite

According to previous TEM studies, dislocations [32-34] and interior twins[35] were observed in lenticular martensite, which [32-34] indicate that deformation modes are slip and twinning in titanium martensite.

Slip character is also planar for the martensite in Ti-8Al-1Mo-1V, but the martensite plate boundaries are strong barriers for dislocations and the slip cannot penetrate the boundaries. Therefore, the effective slip length is limited by the size of martensite [36].

1.4 Texture

Titanium alloys have anisotropic properties, which is physically originated from the anisotropy of HCP α crystal. Texture is the preferential grain orientation, and it is developed by deformation and subsequent recrystallization during the thermomechanical processing [8, 9, 37]. In this section, texture, including microtexture, and its effects on mechanical properties are introduced.

1.4.1 Texture Evolution

Crystallographic texture can be divided into deformation texture and recrystallization texture [9]. The deformation texture is related to the deformation temperature, mode, and degree. Generally the texture intensity increases with the deformation degree. An example of the effects of deformation temperatures and modes on the basal texture is illustrated in Fig. 1.12. At low temperatures, there is a large volume fraction of α phase. Therefore, a typical α deformation texture is obtained as a basal/transverse type texture in unidirectional rolling [8, 9]. With a temperature increase into a window from 900 to 930 °C, an increase in β phase volume fraction results in a condition with a weak texture. For the temperatures just below the β transus, a transverse type transformation texture is developed based on the Burgers

relationship during the subsequent cooling process. When the deformation temperatures are above the β transus, a typical cubic texture will be presented. Fig. 1.12 also shows that the texture symmetry has been changed when the deformation mode is pancake forging [8, 9].

Once the deformation texture is developed, it can be further amplified by the recrystallization process [9], in which a selective grain growth results in a more pronounced recrystallization texture [38].

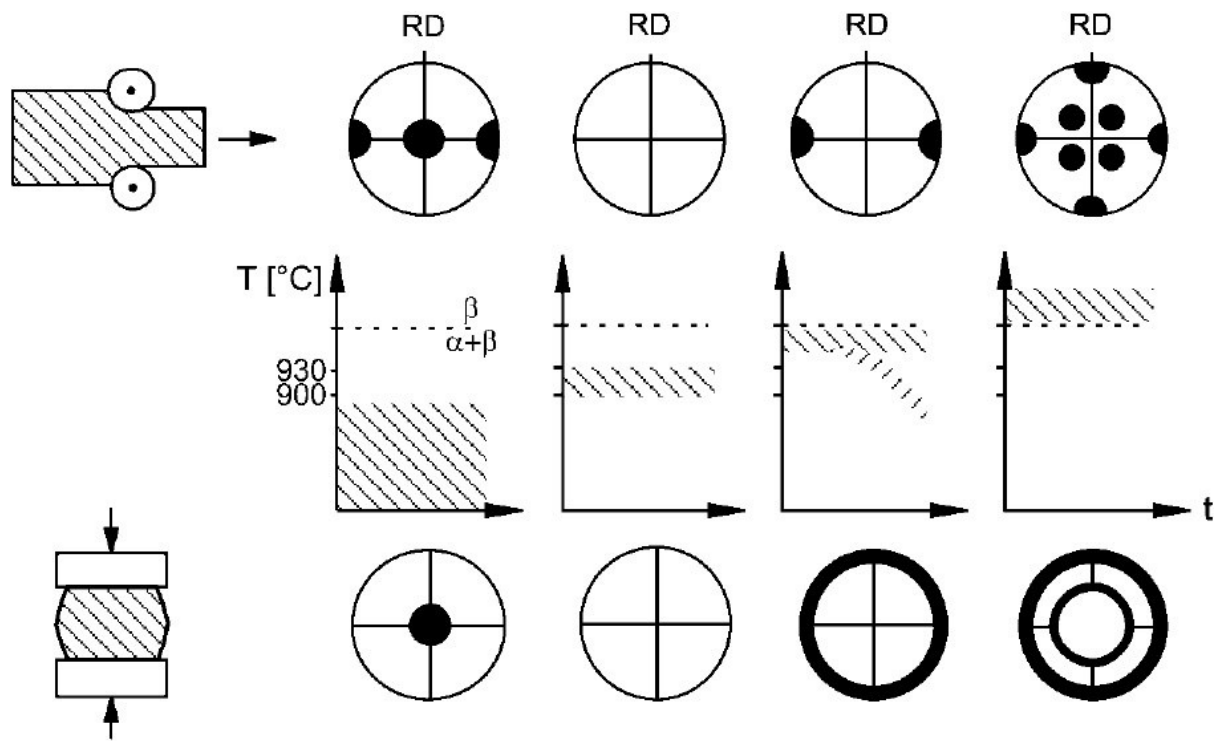


Fig. 1.12 The influence of deformation modes and temperatures on the texture type in Ti-6Al-4V, where RD is the rolling direction [9].

1.4.2 The Effect of Texture

In $\alpha+\beta$ alloys with bi-modal and/or fully equiaxed microstructures, the influence of crystallographic texture on mechanical properties are quite significant. Thermomechanical processing of these two microstructures involves a heavy deformation in the $\alpha+\beta$ phase field, which contributes to an intensive deformation texture. The texture type and intensity are determined by the deformation degree, mode, temperatures [8, 9].

In $\alpha+\beta$ Ti alloys, texture has a pronounced effect on properties including elastic modulus, yield strength, fatigue, fracture toughness and stress-corrosion cracking (SCC) [8, 9, 39]. The tensile properties, are significantly influenced by the orientation between basal component of texture and loading direction. The yield strength and elastic modulus are the highest when the test direction parallel to the *c*-axis of the basal component texture. A similar orientation relationship have been reported in the resistance to fatigue crack nucleation (high cycle fatigue (HCF) strength).

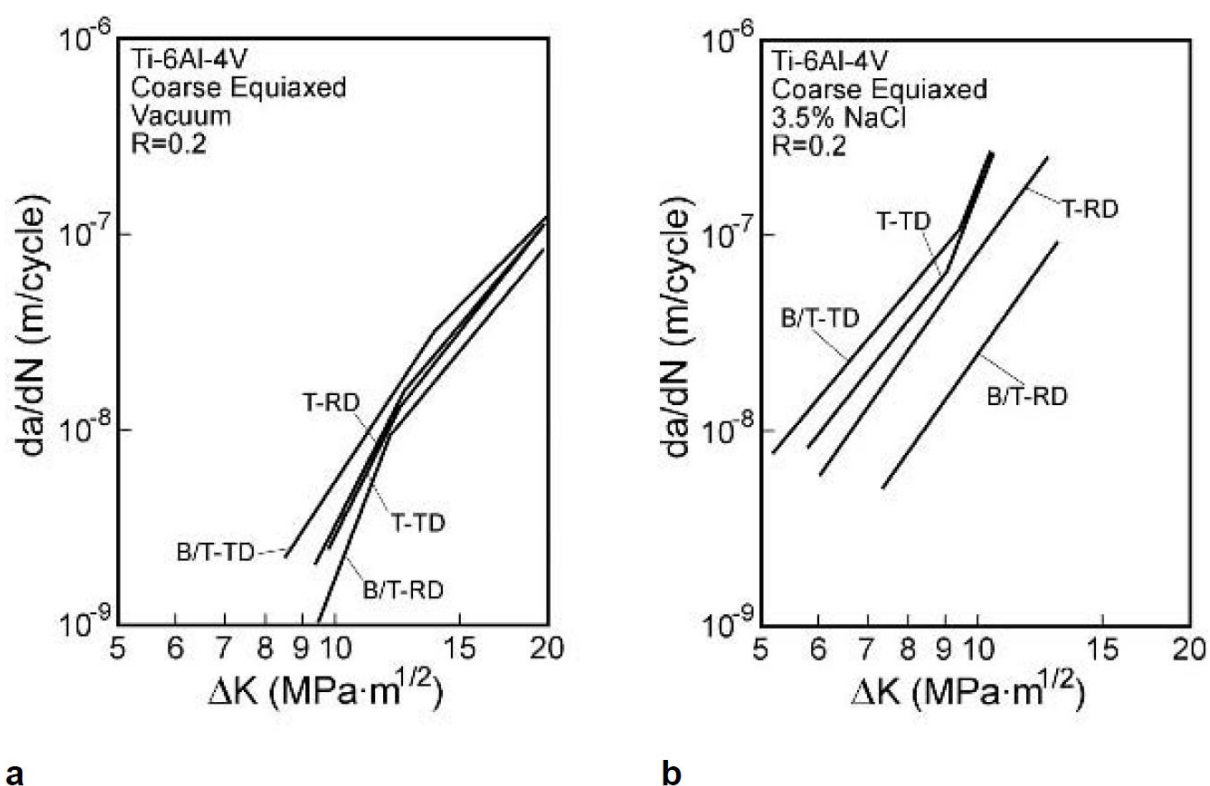


Fig. 1.13 Influence of texture and test direction on macrocrack propagation in Ti-6Al-4V having a fully equiaxed microstructure with α grain size at 12 μm , (a) in vacuum, (b) in 3.5% NaCl aqueous solution. T is the transverse texture, and B/T is the basal/transverse texture. TD and RD are loading directions. [8]

Fig. 1.13 shows the effect of texture on macrocrack propagation in Ti-6Al-4V. There are no noticeable effects in vacuum in Fig. 1.13a. However, the situation is different in an aggressive environment containing hydrogen (Fig. 1.13b). The RD testing conditions (the basal texture component parallel to the loading direction) have a high resistance than that of TD testing conditions ((0002) plane of the basal texture component perpendicular to the loading direction).

These results indicate that there is no texture effect on the fracture toughness, while texture can have an effect on stress-corrosion cracking and hydrogen embrittlement [8]. The Influence of texture on SCC will be further elaborated in section 1.5.

1.4.3 The Effect of Microexture

With the development of electron backscatter diffraction (EBSD), the presence of microtexture is observed in titanium alloys [19]. Microtexture or macrozones are regions of grains with sharp local texture that differ from one region to the next, and the grains have similar crystallographic orientation inside a single microtextured region [40-44]. In a microtextured region, α grains behave similarly as a ‘single grain’, and grain boundaries are not effective barriers for dislocations. Therefore, the effective slip length is much longer in a microtextured region compared to α grains. An example is shown in the following IPF map (Fig. 1.14), α grains with similar colours (microtextured regions) are aligned in the vertical direction in a wrought Ti-8Al-1Mo-1V material [13].

The formation of microtexture occurred in the hot working stage of the ingot during the manufacturing process of wrought products such as sheets, plates or forging billets. Morphology and sharpness of microtexture are related to deformation mode and deformation level. The microtexture is reduced in the Ti alloys which have a severe plastic deformation. But in medium deformed region, microtextured regions are elongated in the same direction of flow line [42, 44]. In a near α alloy IMI 834, L. Germain suggested a macrozone formation mechanism in bi-modal primary and secondary α (α_p/α_s) microstructure [44]. The development of α_p orientation in a microtextured region involves (i) a similar deformation manner of lamellae in the initial colonies, (ii) a limited number of deformation texture components in the HCP crystal structure leads to a sharp texture, (iii) and only a few new orientations are created in α_p globularization. For the sharp texture of α_s colonies, it is related to the obeyed Burgers

relationship between the neighbouring β and α_p grains during the deformation, and the colonies are preferentially selected having the same orientations as that neighbouring α_p grains during β to α transformation [44].

The presence of microtexture has been reported to be detrimental to the fatigue and dwell fatigue properties in titanium alloys [19, 41, 43-49]. For fatigue, the crack formation is promoted in macrozones with (0002) texture in Ti-6Al-4V with bimodal microstructure [40]. The susceptibility of dwell fatigue crack initiation is the highest when the basal plane of microtextured regions is normal to the applied stress in a IMI 834 alloy with a bimodal microstructure [49]. But there are not any published studies about the effect of microtexture on the SCC properties of titanium alloys.

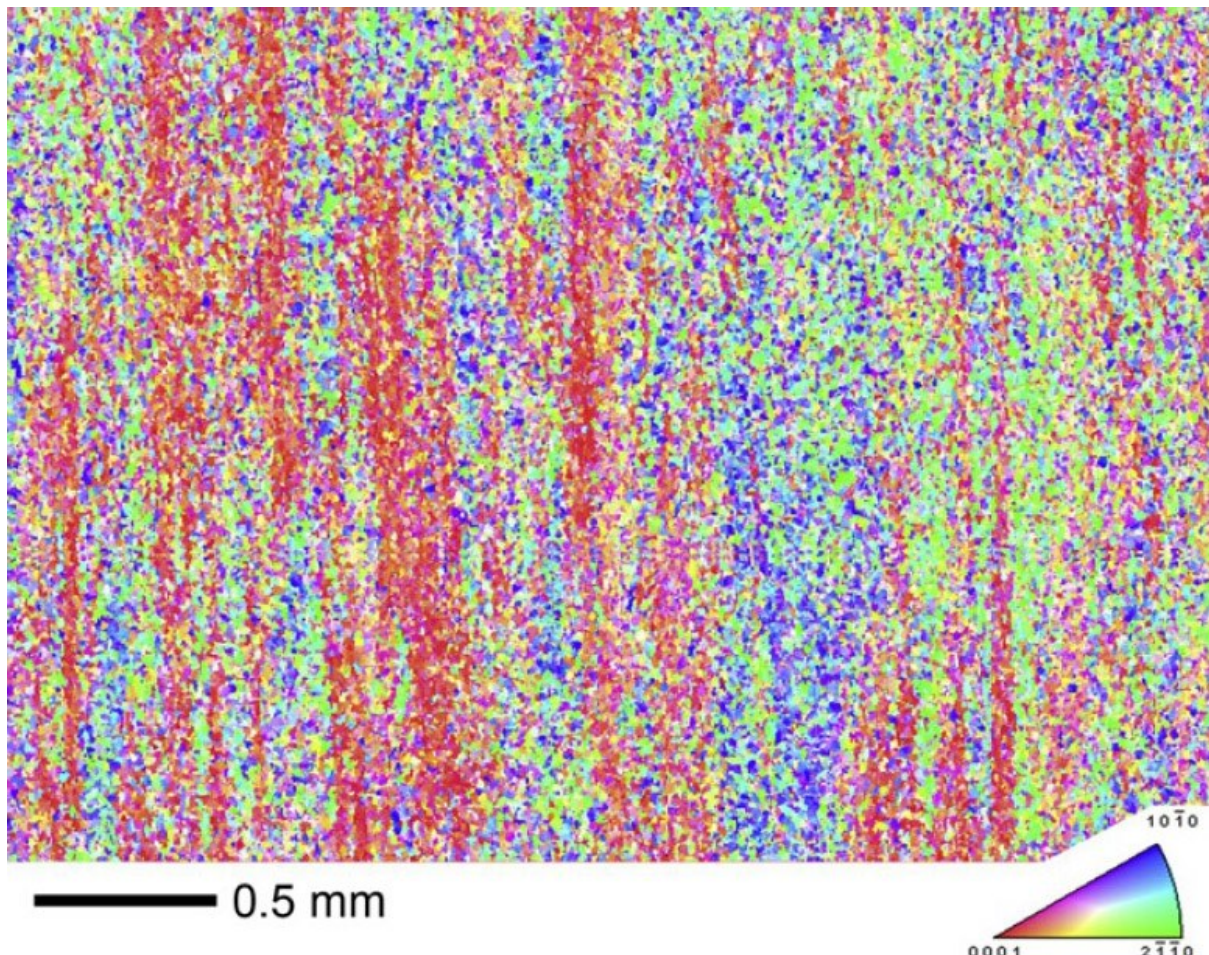


Fig. 1.14 Inverse pole figure (IPF) of wrought TIMET Ti-8Al-1Mo-1V bar material [13]

1.5 Stress-corrosion Cracking

In this section, corrosion behaviour, stress-corrosion cracking (SCC) mechanisms and effects of environmental and metallurgical factors on SCC properties for Ti alloys are described in details.

1.5.1 Corrosion Behaviour

Titanium has a standard hydrogen electrode (SHE) potential at -1.63 V in the galvanic metal series, thus it cannot be regarded as a noble metal. However, titanium has an excellent resistance to general environments including most oxidizing environments, which is arising out of natural protective passive titanium oxide film [8, 50-52]. The passive film can be TiO_2 , Ti_2O_3 or TiO depending on the potential and pH in most aqueous environments, and the amount of Ti^{4+} increases with potential while Ti^{3+} and Ti^{2+} decrease in the passive film. The film has a thickness at order of 10nm and is very corrosive resistant to most aggressive media [22]. The following Ti-H₂O Pourbaix diagram shows that passive film is stable at oxidizing potential and mildly reducing potential for the most of pH range. While, titanium oxide film is not maintained in environments with low a pH. For example, titanium is not corrosion resistant under reducing environments, such as hydrochloride and sulfuric acids, due to the breakdown of protective oxide film [8, 50].

Titanium alloys have a high corrosion resistance to seawater at room temperature due to the oxide film. As inclusions of oxides, carbides and sulphides, are absent in titanium alloys [8, 9], they have a high resistance to pitting corrosion than Hastelloy, Inconel, and passive austenitic stainless steels. However, titanium alloys are rapidly corroded by hydrofluoric acid, because the oxide film is broken down in reducing environments [8, 9]. The corrosion attack even

occurred in fluoride containing solutions. Therefore, Ti alloys cannot be applied in environments where hydrofluoric acid is used [9].

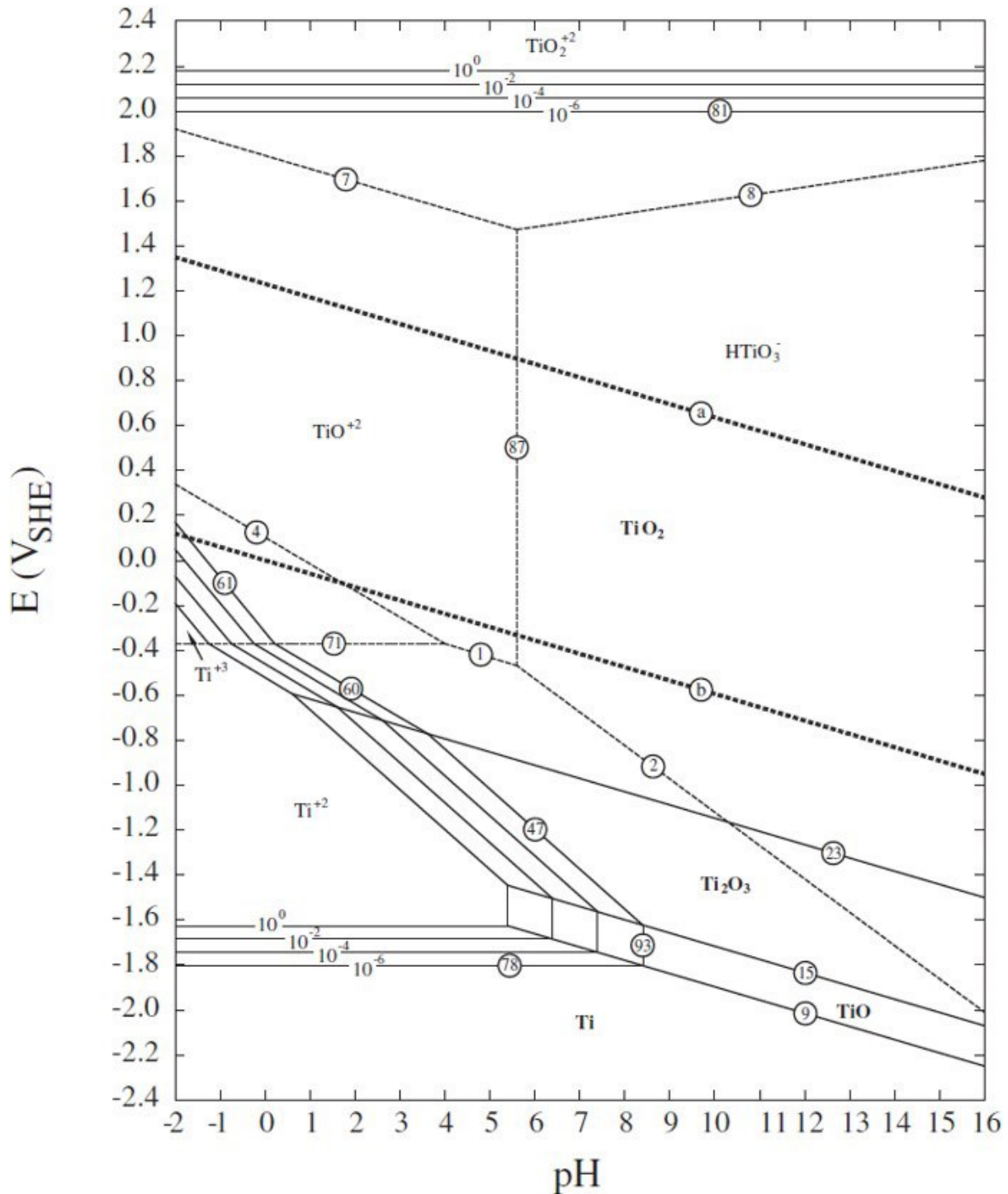


Fig. 1.15 Pourbaix diagram of Ti-H₂O system at 25 °C [53]

Alloying elements also have effects on corrosion properties of titanium alloys. Mo and Zr are highly resistant to corrosion due to their spontaneous oxide films [54, 55]. Therefore, alloying additions of more than 3 Wt. % Mo and 8 Wt. % Zr has a beneficial effect on corrosion

properties of Ti alloys. However, Al content of above 3 Wt.% is detrimental for corrosion resistance [8]. Al is an α stabilizer and enriched in α phase. Thus, an increased Al addition enhances the galvanic interactions between the α and β phases, resulting in an increased dissolution at α/β interface and a reduced corrosion resistance [50].

The investigation of stress-corrosion cracking is in an open circuit condition in current project. The deaerated open circuit potential (OCP) is in the range from -0.38 V to 0.12V (SHE) for titanium [54]. According to Fig. 1.15, relevant electrochemical reactions are summarized in Tab. 1.2.

Tab. 1.2 Relevant electrochemical reactions of Ti-H₂O system in the range of open circuit potential in Fig. 1.15 [53]

Number in Fig. 1.15	Equation
(a)	$2\text{H}_2\text{O} \rightleftharpoons \text{O}_2 + 4\text{H}^+ + 4\text{e}^-$
(b)	$2\text{H}^+ + 2\text{e}^- \rightleftharpoons \text{H}_2$ (acidic, deaerated solution)
(1)	$\text{TiO}^{+2} + 2\text{H}^+ + 2\text{e}^- \rightleftharpoons \text{Ti}^{+2} + \text{H}_2\text{O}$
(2)	$\text{HTiO}_3^- + 5\text{H}^+ + 2\text{e}^- \rightleftharpoons \text{Ti}^{+2} + 3\text{H}_2\text{O}$
(4)	$\text{TiO}^{+2} + 2\text{H}^+ + \text{e}^- \rightleftharpoons \text{Ti}^{+3} + \text{H}_2\text{O}$
(7)	$\text{TiO}_2^{+2} + 2\text{H}^+ + 2\text{e}^- \rightleftharpoons \text{TiO}^{+2} + \text{H}_2\text{O}$
(8)	$\text{TiO}_2^{+2} + \text{H}_2\text{O} + 2\text{e}^- \rightleftharpoons \text{HTiO}_3^- + \text{H}^+$
(9)	$\text{TiO} + 2\text{H}^+ + 2\text{e}^- \rightleftharpoons \text{Ti} + \text{H}_2\text{O}$
(15)	$\text{Ti}_2\text{O}_3 + 2\text{H}^+ + 2\text{e}^- \rightleftharpoons 2\text{TiO} + \text{H}_2\text{O}$
(23)	$2\text{TiO}_2 + 2\text{H}^+ + 2\text{e}^- \rightleftharpoons \text{Ti}_2\text{O}_3 + \text{H}_2\text{O}$
(47)	$\text{Ti}_2\text{O}_3 + 6\text{H}^+ + 2\text{e}^- \rightleftharpoons 2\text{Ti}^{+2} + 3\text{H}_2\text{O}$
(60)	$\text{TiO}_2 + 4\text{H}^+ + 2\text{e}^- \rightleftharpoons \text{Ti}^{+2} + 2\text{H}_2\text{O}$
(61)	$\text{TiO}_2 + 4\text{H}^+ + \text{e}^- \rightleftharpoons \text{Ti}^{+3} + 2\text{H}_2\text{O}$
(71)	$\text{Ti}^{+3} + \text{e}^- \rightleftharpoons \text{Ti}^{+2}$
(78)	$\text{Ti}^{+2} + 2\text{e}^- \rightleftharpoons \text{Ti}$
(81)	$\text{TiO}_2^{+2} + 2\text{e}^- \rightleftharpoons \text{TiO}_2$
(87)	$\text{TiO}^{+2} + 2\text{H}_2\text{O} \rightleftharpoons \text{HTiO}_3^- + 3\text{H}^+$
(93)	$\text{Ti}^{+2} + \text{H}_2\text{O} \rightleftharpoons \text{TiO} + 2\text{H}^+$

For Ti-8Al-1Mo-1V, spontaneous passivation happened in 3.5% NaCl solution. Therefore, Ti-811 also has a good corrosion resistance to seawater. But it is corroded in 5M HCl solution at 35 °C. Ti-8Al-1Mo-1V has an incomplete passivity due to stability of soluble Ti^{3+} anion and the preferential corrosion site is β phase [50, 54, 56].

1.5.2 Stress-corrosion Cracking Characteristics and Mechanisms

Stress-corrosion cracking (SCC) is a gradual crack growth under the simultaneous presence of sustained load and corrosive environment. SCC cracks are normally multiple and branched, and can be either transgranular or intergranular or a combination of both depending on material-environment systems [57, 58]. For transgranular SCC facets, the orientation of the faceted plane are generally close to a specific crystallographic plane. For example, {110} planes in α -brass [57] and {1017} planes in a Ti-8Al-1Mo-1V alloy [17, 59] are observed close to the faceted plane. For some Ti alloys, the SCC cracking rate can be as high as 10^{-4} m/s [58]. The result of SCC can be a catastrophic failure due to the external applied load in a high strength material [57, 58]. Characteristics and mechanisms of SCC are similar to the hydrogen embrittlement (HE) in some conditions due to the hydrogen evolution and entry at the SCC crack tip [57, 58].

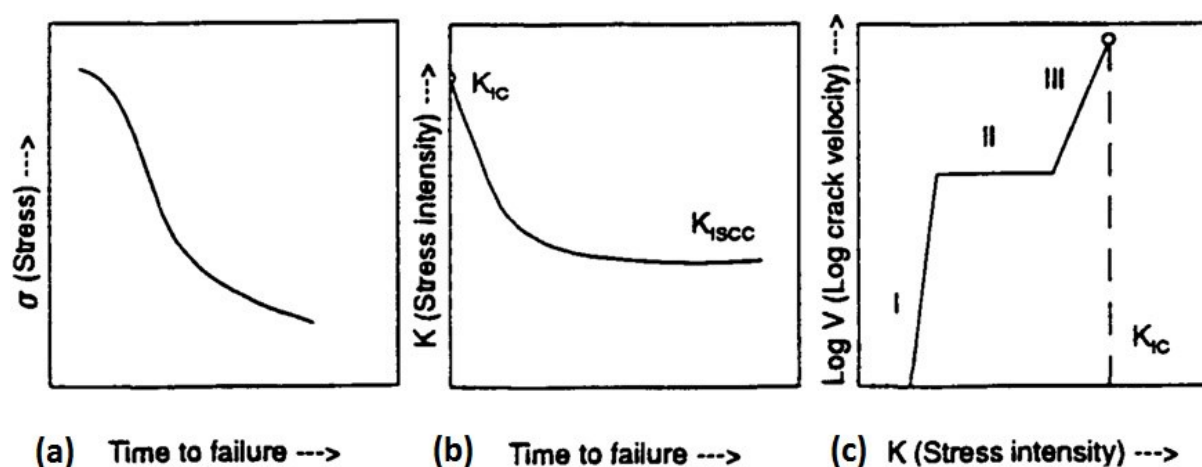


Fig. 1.16 SCC data representation for (a) type 1 test method: a static load is applied on smooth samples, (b) and (c) for type 2 test: a static or dynamic load is applied on samples with notches or pre-cracks [60].

There are several ways to quantitatively measure SCC properties [60]: (1) A static load is applied on smooth U-bend, C-ring, bent beam, and dead-loaded tension sample, and the data is represented in Fig. 1.16a. (2) Fracture mechanics tests are conducted on samples with notches or pre-cracks with a static load or dynamic load, and the data can be represented as Fig. 1.16b and Fig. 1.16c. (3) Slow strain rate test (SSRT) is applied on tensile specimens with a dynamic load.

There are several SCC mechanisms proposed in different alloy systems, which can help us to obtain the understanding of SCC. It is accepted that different mechanisms work in different material-environment systems, but there are still arguments over the operating mechanism of a given materials-environment system [57]. The following paragraphs are a list of SCC mechanisms.

Dissolution Mechanism: SCC growth is an accumulation of limited dissolution and oxidation, which is caused by the rupture of protective film at crack tips due to the mechanical load. The dissolution preferentially occurred at the plane normal to the applied stress [57, 58, 61, 62]. It could be promoted by either a chemical active path, like anodic precipitates, or a stress/strain concentration at crack tips [58].

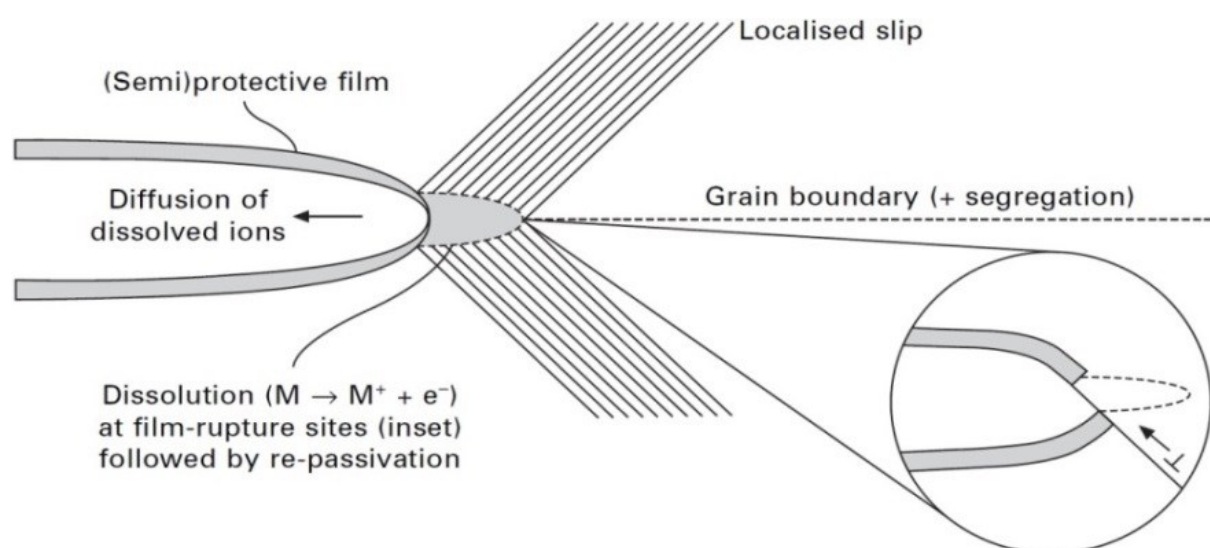


Fig. 1.17 Illustration of slip dissolution mechanism [58]

The most popular term in dissolution mechanism is the slip dissolution mechanism (SDM), which is illustrated in Fig. 1.17 and described as following three steps: (1) Slip bands intersect and rupture the protective film at crack tip. (2) Anodic dissolution then happened to the exposed metal which is located underneath the protective film originally. The preferential attack sites are along grain boundaries or low-index crystallographic planes. (3) The exposed metal is re-passivated, and then slip dissolution occurs again. Generally, re-passivation happens at low crack-tip strain rate. However, it may not occur at high strain rate, when the strain rate is higher than the re-passivation rate [58].

SDM is suitable for some intergranular SCC cases in passivating environments, but it does not fit transgranular SCC conditions. In addition, SDM is not applicable in chloride-SCC, because there is a lack of consideration of the crack tip chemistry [57]. As α and $\alpha+\beta$ titanium alloys have transgranular SCC cracks[13, 63], SDM or dissolution mechanism cannot be the operating SCC mechanism for Ti-8Al-1Mo-1V [22, 64].

Film Induced Cleavage (FIC): Film induced cleavage (FIC) is a rapid fracture of brittle de-alloyed film at crack tips continue into the underlying substrate with a very limited dislocation activity. Crack is then arrested and blunted by encountering obstacles such as slip bands in the substrate. Fig. 1.18 is a schematic illustration of film induced cleavage mechanism [57, 58, 62].

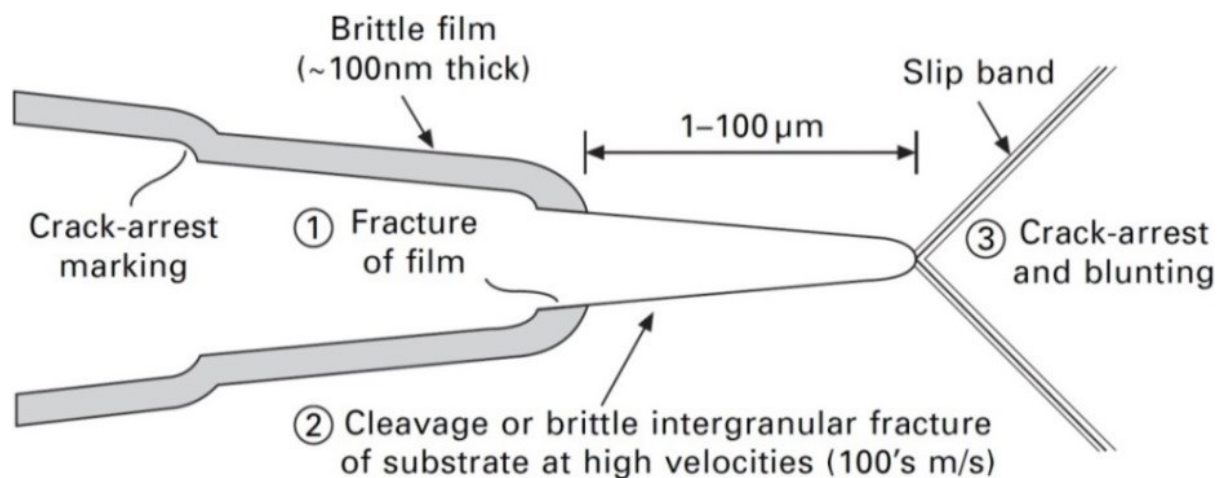


Fig. 1.18 Illustration of film induced cleavage mechanism.[58]

In SCC crack failed by FIC, the crack portion in the underlying substrate is much longer than the brittle film, and the propagation velocity from the brittle film into the substrate is at a magnitude of 10^2 m/s or even more. In the substrate, a decrease of crack propagation velocity will be achieved by dislocations emissions from crack tips and encountering slip bands, and crack arresting and blunting then occur. Cracking by FIC leaves a series of cracking-arrest markings (striation) on the fracture surface sometimes [57, 58].

FIC commonly occurs in relatively high solid solution alloys, such as brass, copper-gold, silver-gold alloys, austenitic stainless steel. It can be either transgranular (cleavage like) or intergranular cracks. The film properties are important to FIC, such as brittleness, bond and coherence between film and substrate, elastic modulus and thickness of the film. Examples of the films are nano-porous and de-alloyed films [57, 58]. On the SCC fracture surface of Ti-8Al-1Mo-1V, there are neither any crack-arrest markings nor continuous propagations from the oxide film to underlying material. Therefore, FIC may not be the operating mechanism for SCC in Ti-8Al-1Mo-1V.

Hydride Formation and Fracture: The hydride formation and fracture mechanism is a repeated cleavage processes of hydrides formed, which are nucleated and grown at the SCC crack tip (See Fig. 1.19). [65]

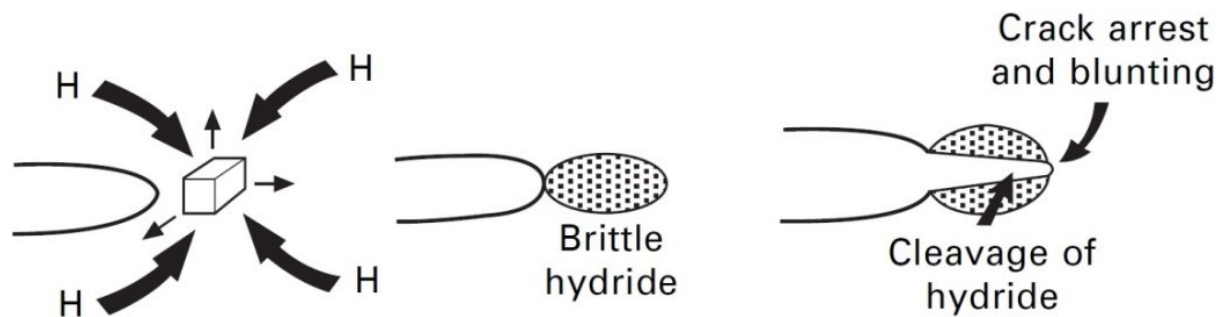


Fig. 1.19 Illustration of hydride formation and fracture mechanism [65]

Titanium alloys are hydride formation alloys. However, hydride formation and crack may be not the mechanism of SCC in titanium alloys even in the presence of hydride on the fracture

surface, because hydride can be formed after fracture in SCC environments [58, 66]. The hydride formation mechanism is kinetically sluggish. For example, 14 minutes was found to be required for the first hydride formation at a 16 KPa gaseous hydrogen environment in Ti-4Al alloy [13, 67]. As a result, this mechanism is only suitable for low stress-corrosion crack propagation velocity situations.

The hydride formation and cleavage mechanism has been reported as the hydrogen embrittlement mechanism in Ti-4Al alloy at low stress intensity conditions [67]. In Ti-8Al-1Mo-1V, the transgranular SCC fracture are favourably orientated on crystallographic planes either parallel to or 10° - 15° from the (0002) plane, and the latter is close to $\{10\bar{1}7\}$ planes. Both of (0002) and $\{10\bar{1}7\}$ planes are hydride habit planes [13, 15, 17, 64, 68]. Although it seems that SCC mechanism could be related to hydride formation in Ti-8Al-1Mo-1V, there are two apparent differences. One is that the SCC fracture is transgranular crack in Ti-811, while hydride formation and fracture mechanism leaves an intergranular fracture. The other is the hydride formation is kinetically sluggish which is much slower than the SCC crack propagation in Ti-811 [67, 69]. Therefore, the mechanism involving hydride formation is not feasible for aqueous SCC mechanism in Ti-8Al-1Mo-1V either.

Hydrogen Enhanced Decohesion (HEDE): Hydrogen enhanced decohesion (HEDE) is a solute hydrogen based mechanism, in which interstitial hydrogen decreases cohesion of intermetallic bonds at the hydrostatic stress region ahead of crack tip, at crack tip, and grain boundaries (See Fig. 1.20). Hypothesis of HEDE includes charge transfer and weakening of intermetallic bonds, which contribute to a tensile separation of atoms [58, 65, 70]. HEDE occurs in both transgranular and intergranular forms, and the fracture surface shows little or no plastic deformation. Grain boundaries are more favourable attacking sites for HEDE compared to grain interior due to the higher hydrogen concentration at grain boundaries [71].

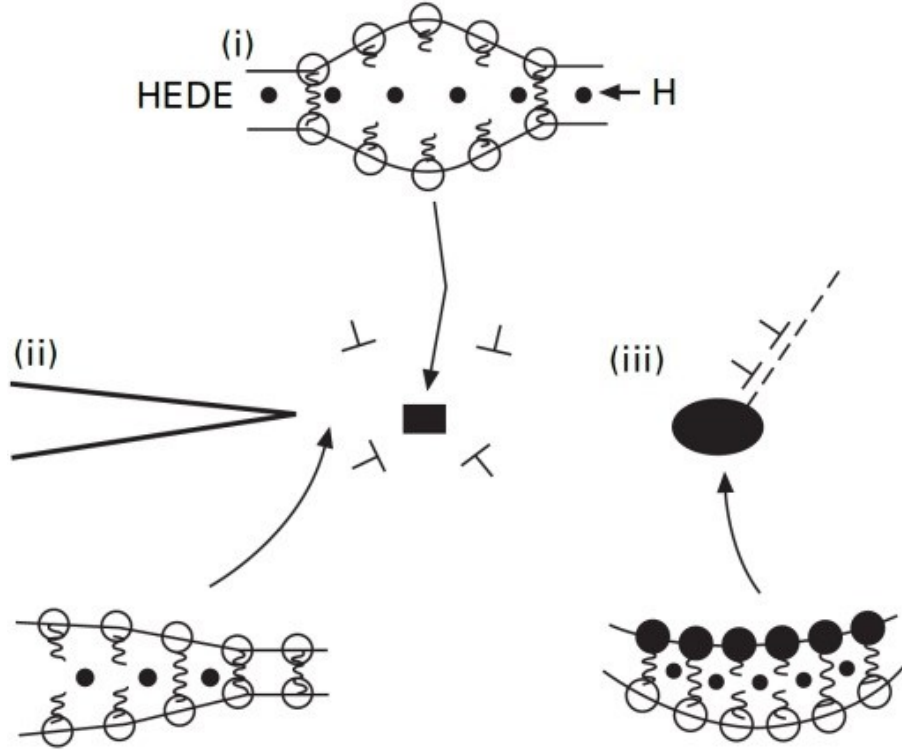


Fig. 1.20 Hydrogen Enhanced Decohesion (HEDE) mechanism at (i) ahead of crack tip, (ii) crack tip, (iii) grain boundaries [65].

Hydrogen Enhanced Localized Plasticity (HELP): In addition to the HEDE, another hydrogen based mechanism is hydrogen enhanced localized plasticity (HELP), in which hydrogen interacts with dislocations and promotes dislocation movement within high hydrogen concentration regions (see Fig. 1.21). The hydrogen concentration is high in the hydrostatic stress region ahead of crack tip, which also provides an entrance for absorbed hydrogen from solution. The repulsive interaction between dislocations is decreased by hydrogen, and a high dislocation activity is then promoted in the localized region of crack tip [57, 58, 62, 65, 70, 72, 73]. Crack paths could be either intergranular or transgranular depending on whether hydrogen segregates to grain boundaries or distributes within grain interior [65].

In aluminium, G. Lu found that hydrogen decreases the Peierls-Nabarro stress of dislocation by more than an order of magnitude, and hydrogen has a strong binding to dislocation cores. They also observed that hydrogen inhibits cross-slip and promotes planar slip [74]. A direct experimental observation of HELP is occurred in Ti-4 Wt. % Al alloy at high stress intensity

test in H₂ gaseous environment [67], in which hydrogen decreases the critical stress for dislocation motion and increases the dislocation velocity at high crack propagation rate.

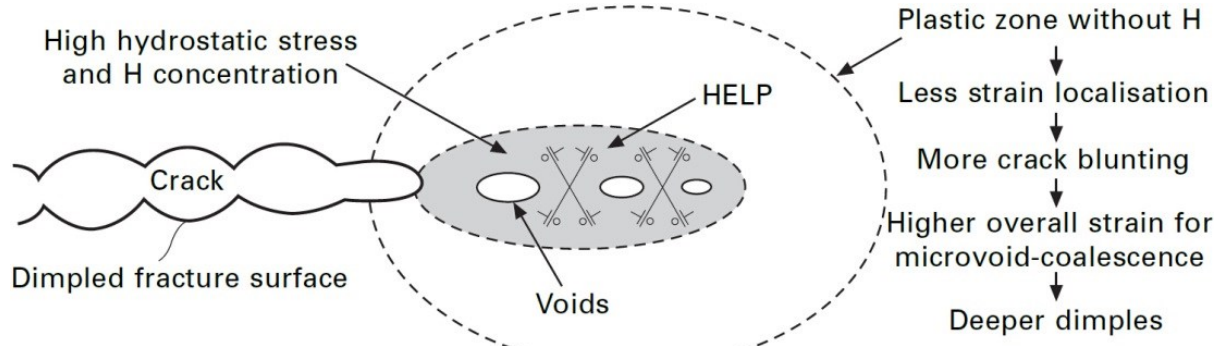


Fig. 1.21 Illustration of Hydrogen Enhanced Localized Plasticity (HELP) processes, involving a mircovoid-coalescence process, and a localized plasticity in high hydrogen concentration region.[65]

Absorption Induced Dislocation Emission (AIDE): Absorption induced dislocation emission (AIDE) is that absorbed hydrogen weakens intermetallic bonding and facilitates dislocation emission at the crack tip, and promotes subsequent motion of dislocations away from the crack tip (see Fig. 1.22) [65, 73].

Comparing to HEDE, the emission of dislocations occurs rather than decohesion. Hydrogen penetrates a few atomic layers and facilitates the formation of a dislocation core by a surface step arising from an atomic shear movement. And then, the dislocation is moved away from crack tip under the applied stress. Only a small portion of dislocations intersect with crack tip and contribute to crack propagation, but most of dislocations result a crack re-blunting. AIDE mechanism also involves nucleation and growth of micro or nano voids ahead of crack tip, and the preferential sites are at second phase particles and slip bands intersections. The formation and growth of voids contribute to crack growth and also crack sharpening. AIDE fracture path can be either intergranular or transgranular depending on whether dislocation emission or voids formation dominating. In transgranular cracks, alternative slip happens due to the built up back-stress by the previously emitted dislocations. As a result, the overall crack front lies along the

intersection line of crack planes and slip planes, such as fracture along {100} planes when <110> directions and {112} slip planes are active in BCC material [57, 58, 65].

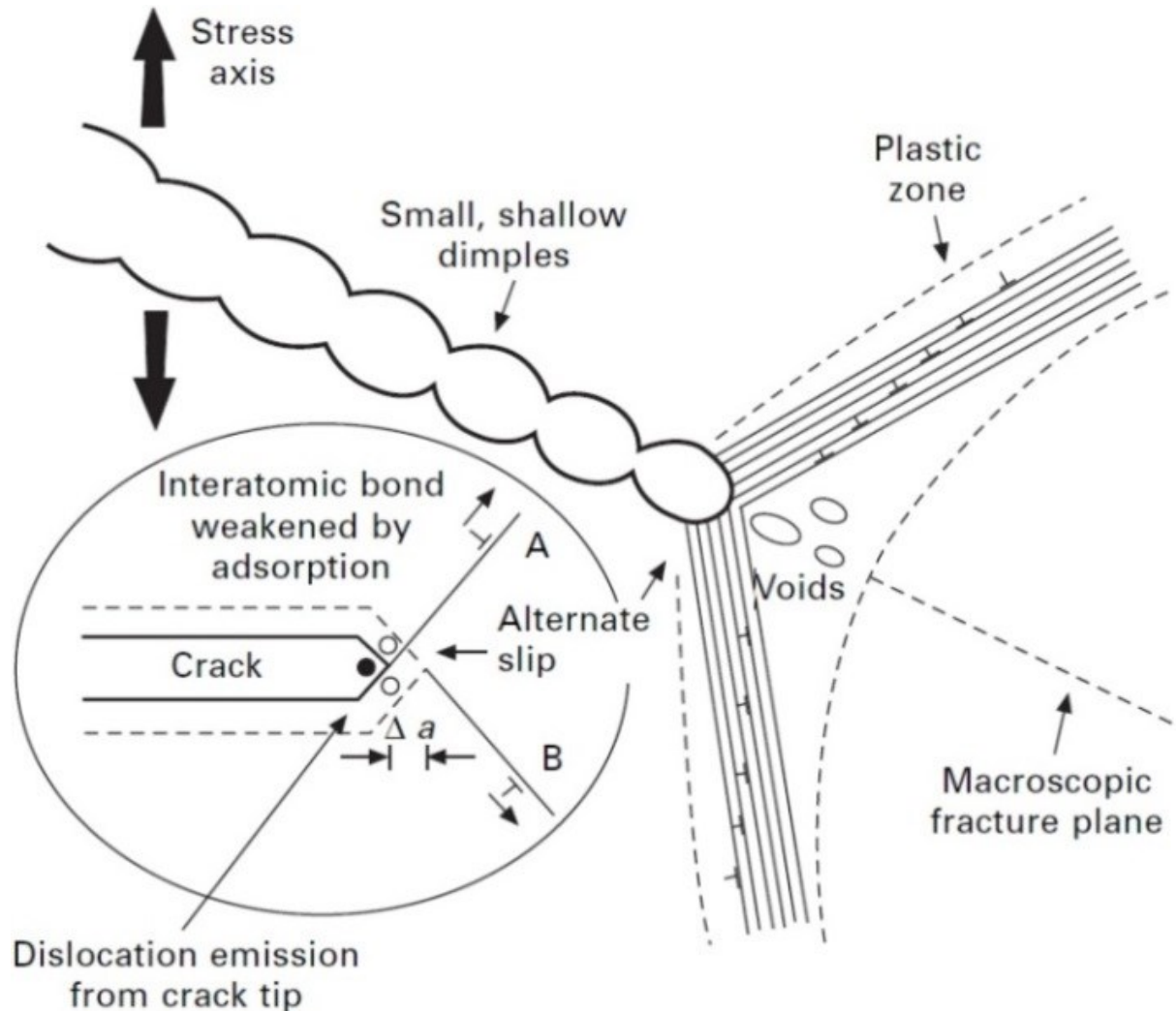


Fig. 1.22 Illustration of Absorption Induced Dislocation Emission (AIDE) mechanism, in which absorbed hydrogen caused dislocation emission [65]

Hybrid Mechanism: There are more than one SCC mechanisms active in some situations, and an example is the corrosion enhanced localized plasticity (CELP), which is a hybrid mechanism. CELP involves anodic dissolution and HELP mechanism. Anodic dissolution ruptures the protective oxide film and causes dissolution on preferred planes, and HELP promotes dislocation activity. CELP is generally applied in FCC materials with a transgranular SCC crack path [65, 71].

Mechanisms involve hydrogen, like HEDE, HELP, and AIDE, could also be active simultaneously [65, 73]. In AIDE, voids nucleation ahead of the crack tip is achieved by slip intersection in HELP and decohesion at secondary phase particle interface in HEDE (See Fig. 1.23a). HELP and AIDE can occurred as a hybrid mechanism. HELP reduces the back-stress of the emitted dislocations in AIDE, and dislocations can then move away from the crack tip. Therefore, HELP and AIDE could occurred in sequence. AIDE and HEDE can also be operated alternatively. HEDE occurs when the back-stress of dislocation emission is high for AIDE, and AIDE occurs again when crack is away from the stress field of the dislocations previous emitted (See Fig. 1.23b) [65].

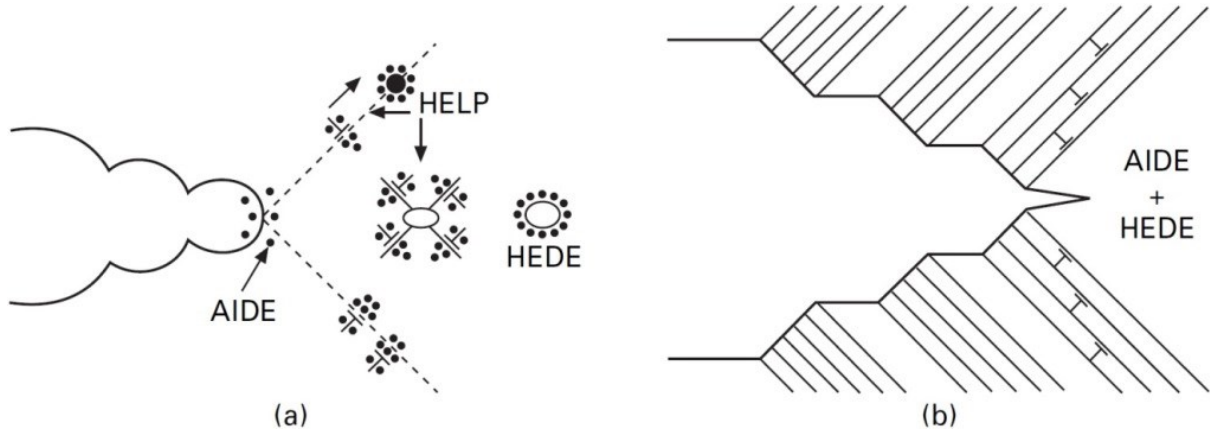


Fig. 1.23 Illustration of hybride SCC mechanisms [65].

Based on the SCC mechanisms described above, HEDE, HELP, AIDE or combination of them could be applied to the SCC of Ti-8Al-1Mo-1V, and some other unknown mechanism(s) may be possible too. Little or no work has been done specifically to elucidate the actual SCC mechanism(s) for Ti-811.

1.5.3 Role of Environment and Metallurgy on SCC Properties in Ti alloys

In aqueous SCC processes of Ti-8Al-1Mo-1V, the dominant characteristic is transgranular cracks (see Fig. 1.24) [16]. Both the SCC initiation facets (Fig. 1.25) and propagation facets (Fig. 1.26) are transcrystalline in Ti-811. The facets contain steps, which formed terrace at

different heights, and primary and secondary tear ridges on the surface. In addition to the facets, a few ductile dimpled regions are also presented [13]. Similarly in Ti-6Al-4V, a typical transgranular SCC crack also has facets containing steps and tear ridges, and some nanoscale dimples [36]. In another near α alloy IMI834, faceted regions and tear ridges are also presented on the hot salt SCC fracture surface [63]. It seems that the SCC fracture surfaces have the same SCC facets for α and $\alpha+\beta$ titanium alloys [13, 16, 22, 75, 76]. While in β titanium, the cracks can be either transgranular or intergranular based on ageing treatments and hydrogen contents [22, 64].

SCC processes involves the protective oxide film breakdown, crack initiation and growth in titanium alloys. The first step is the passive film break down, which is controlled by the corrosive environment and stress intensity at crack tips [22]. For the following crack initiation and growth, acidic methanol SCC of Ti-6Al-4V was explained by anodic dissolution on preferential slip planes [77], and methanol SCC of Ti-24Al-11Nb is governed by the anodic dissolution and dislocation emission [78].

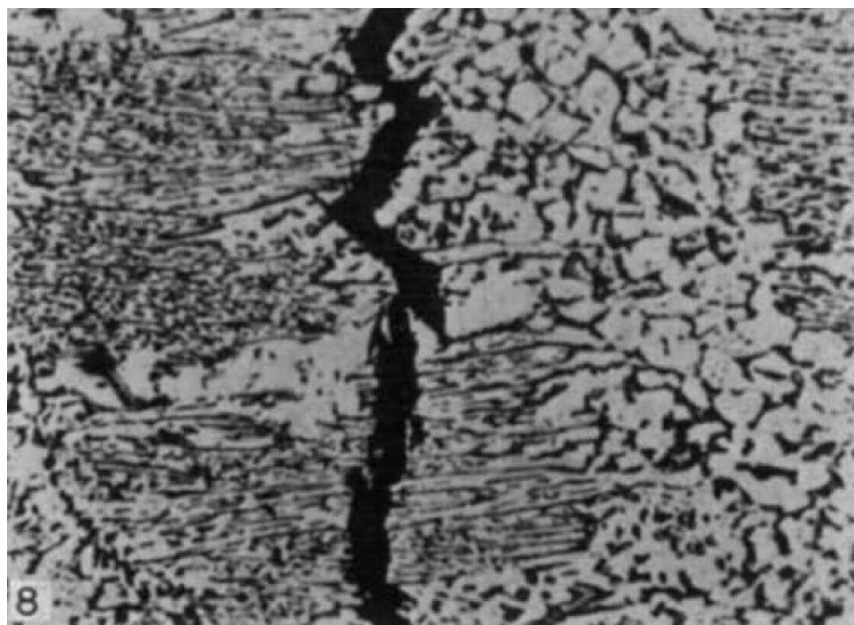


Fig. 1.24 Transgranular SCC crack of Ti-8Al-1Mo-1V tested in aqueous NaCl solution [16]

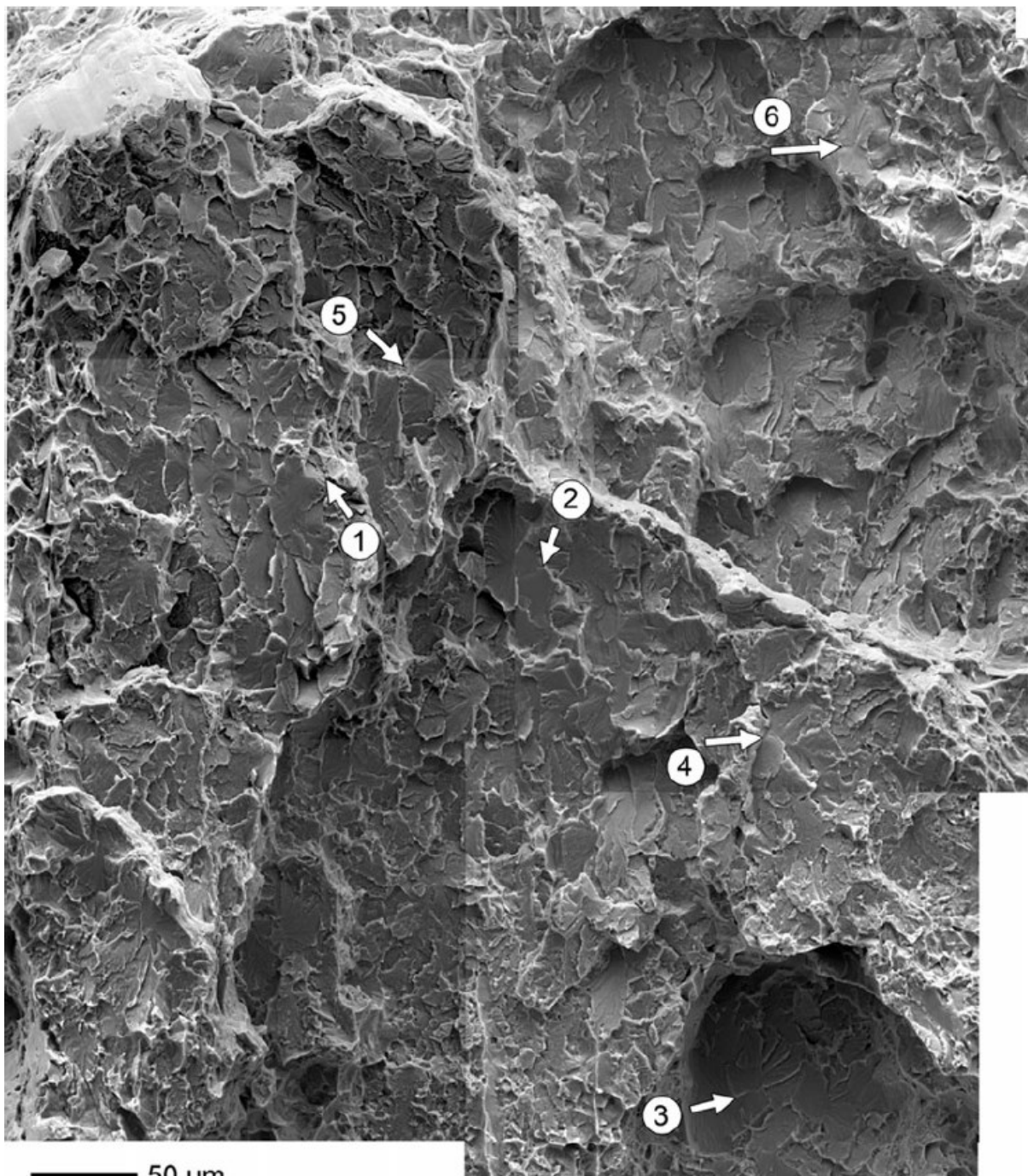


Fig. 1.25 SCC initiation facets on the fracture surface of Ti-8Al-1Mo-1V tested in 3.5% NaCl solution at 95% yield strength, 1 indicates the primary initiation site and 2-6 are the secondary initiation sites [75]

In a quantitative tilt fractography study of crystallographic orientations of facets, it has been observed that some fracture planes are inclined 5° - 15° away from basal plane, which are close to $\{10\bar{1}7\}$ planes corresponding to hydride habit planes (see Fig. 1.27) [13, 75]. Although it seems that SCC mechanism could be related to hydride formation in Ti-8Al-1Mo-1V, there are two key facts to note. Firstly, the first hydride formation takes about 14 min in an environment

cell with 16 kPa H₂ atmosphere in a Ti-4Al alloy which is much slower than the SCC crack propagation [67]. Secondly, the SCC fracture is transgranular crack in Ti-8Al-1Mo-1V, while hydride formation and fracture mechanism leaves an intergranular fracture. Therefore, mechanism involving hydride formation is not feasible for aqueous SCC mechanism of Ti-8Al-1Mo-1V. Therefore, the active SCC mechanism is still an open question.

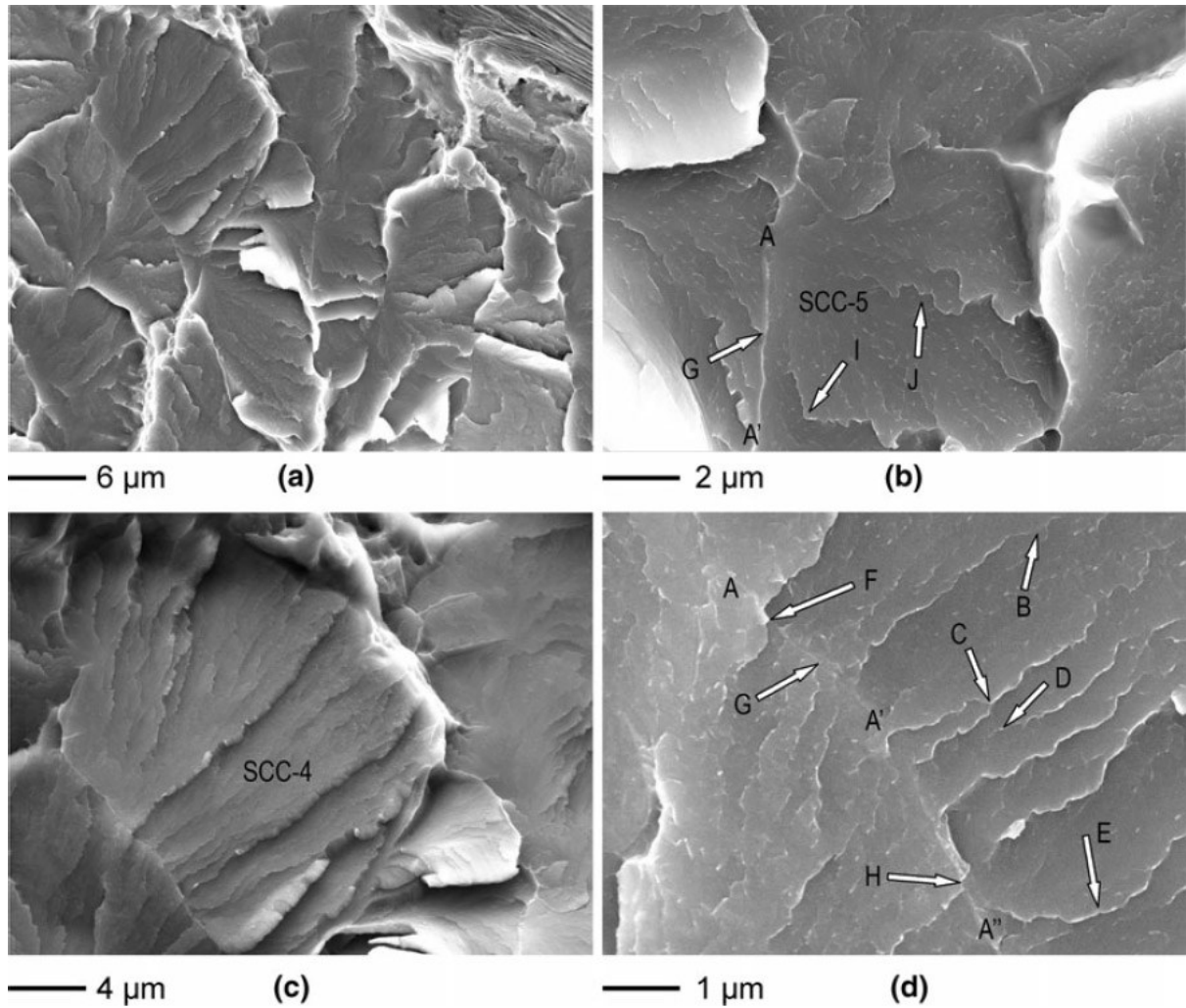


Fig. 1.26 SCC Propagation facets on the fracture surface of Ti-8Al-1Mo-1V tested in 3.5% NaCl solution at 95% yield strength [75]

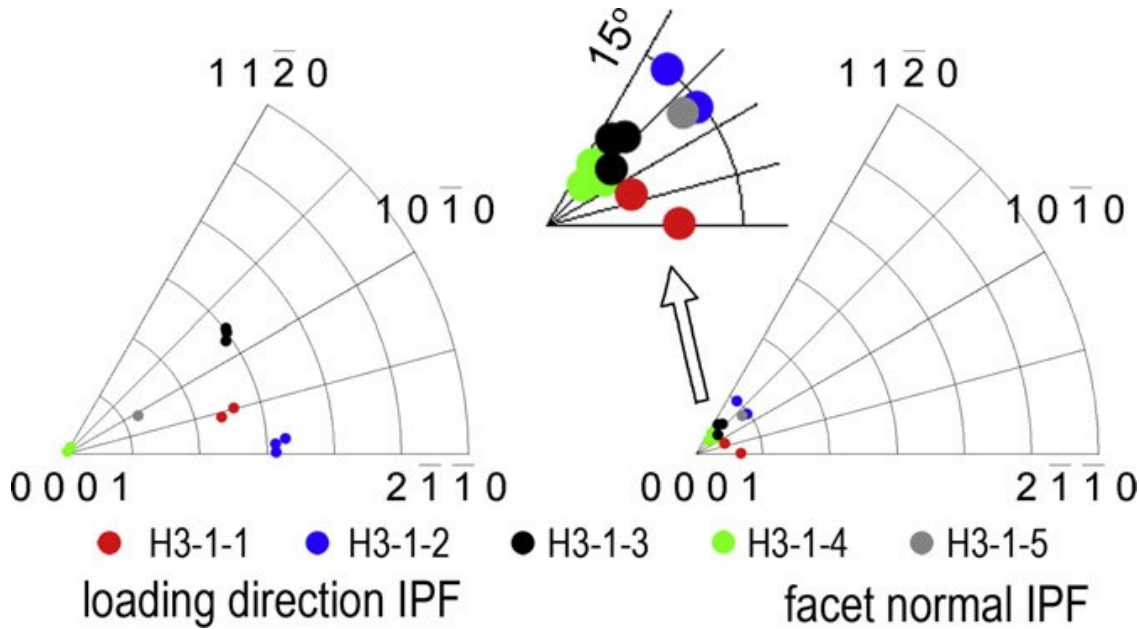


Fig. 1.27 Facet crystallography of as-received Ti-8Al-1Mo-1V in aqueous 3.5% NaCl solution [13]

Effect of Ion Additions and Concentration

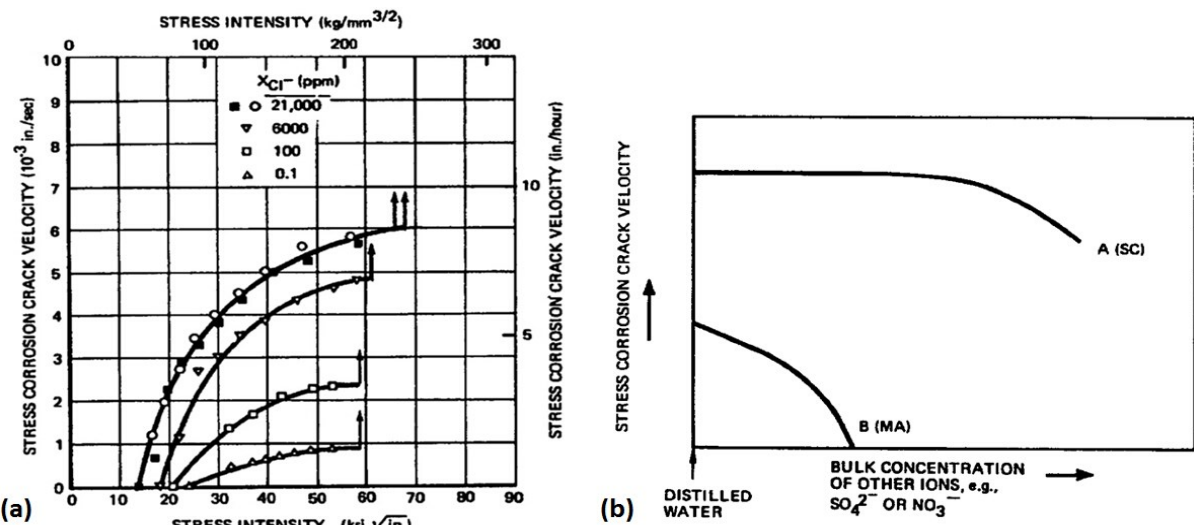


Fig. 1.28 Effect of ions in solution, (a) effect of Cl^- concentration on crack propagation rate of Ti-8Al-1Mo-1V, (b) Effect of SO_4^{2-} or NO_3^- on SCC crack propagation [36]

The addition of halide anions into solution, like Cl^{-1} , Br^{-1} , and I^{-1} , increases the SCC susceptibility. Fig. 1.28a shows that the propagation velocity increases and K_{ISCC} is slightly decreased with increasing Cl^{-1} addition for Ti-8Al-1Mo-1V [36]. Another halide anion F^{-1} has effects of either increasing or decreasing SCC susceptibility in concentrated or diluted solution respectively. For the rest anions, most of them have a neutral effect on SCC susceptibility, but they may prohibit SCC in some cases (see Fig. 1.28b) [36]. The effects of cations are depended

on whether the added cation is more noble than Ti, for example, Na, K, and Li do not have any influences on SCC behaviours in titanium alloys [36].

Fig. 1.29 shows the effect of three different microstructures on SCC properties of Ti-8Al-1Mo-1V. Ti-8Al-1Mo-1V exhibits a typical regions I and II type crack propagation in both neutral and acidic solutions. In contrast to the neutral solution, the SCC resistance is weaker (higher crack velocity and lower threshold stress intensity) in a 10 M HCl solution. In the three different microstructure, SCC susceptibility increases significantly in the sample with α_2 precipitation (SC condition) [36]. Fig. 1.30 illustrates that the SCC susceptibility increases dramatically with hydrogen concentration when pH value below 3.

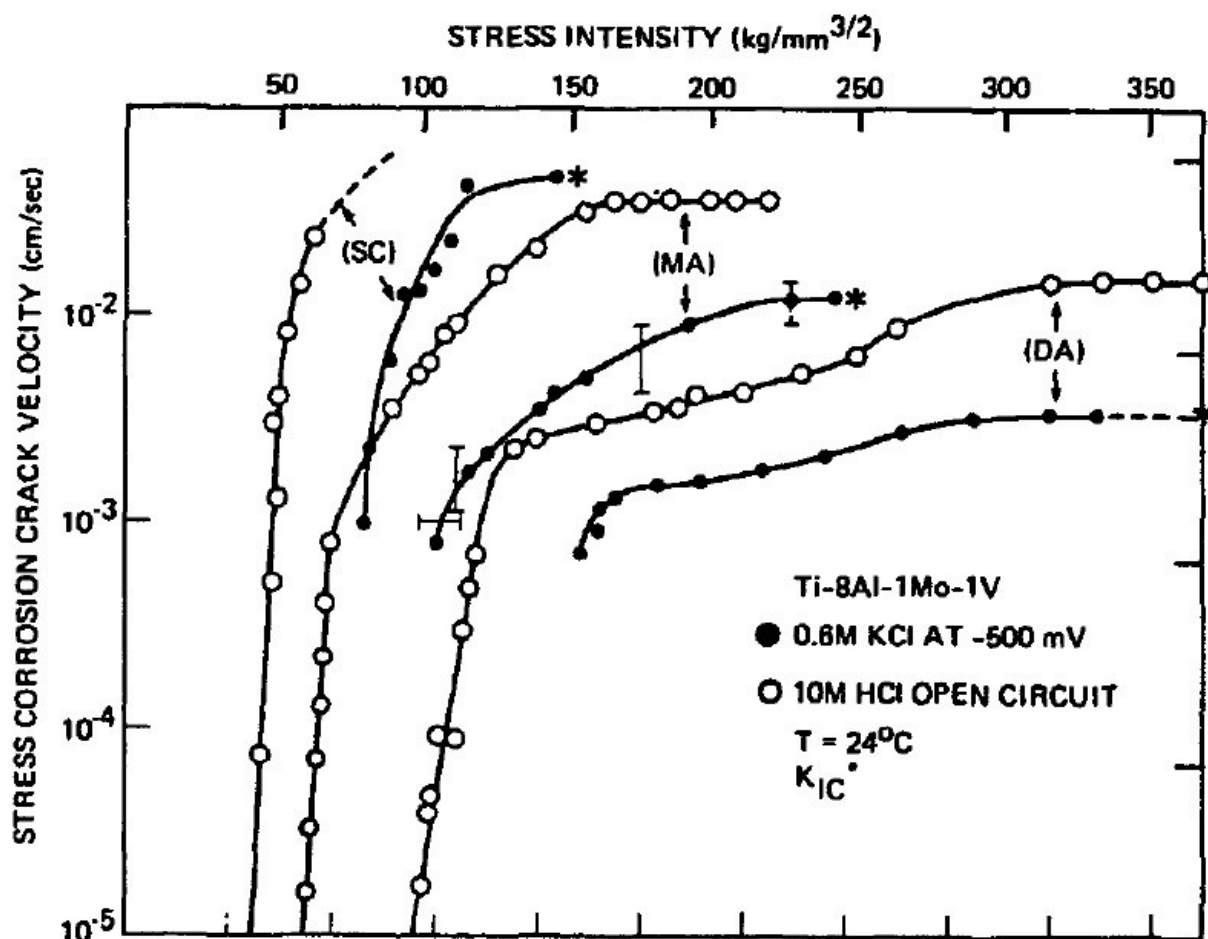


Fig. 1.29 Effect of microstructure on SCC susceptibility of Ti-8Al-1Mo-1V with different microstructures, SC (step cooled - solution treated at 820°C and then step-cooled to 450°C): designed to promote α_2 precipitation, MA (wrought annealed - solution treated at 820°C and then furnace-cooled): equiaxed microstructure with α_2 precipitates formed during the cooling , DA (duplex annealed - solution treated at 820°C and then water-quenched): bi-modal microstructure with no α_2 precipitates [36].

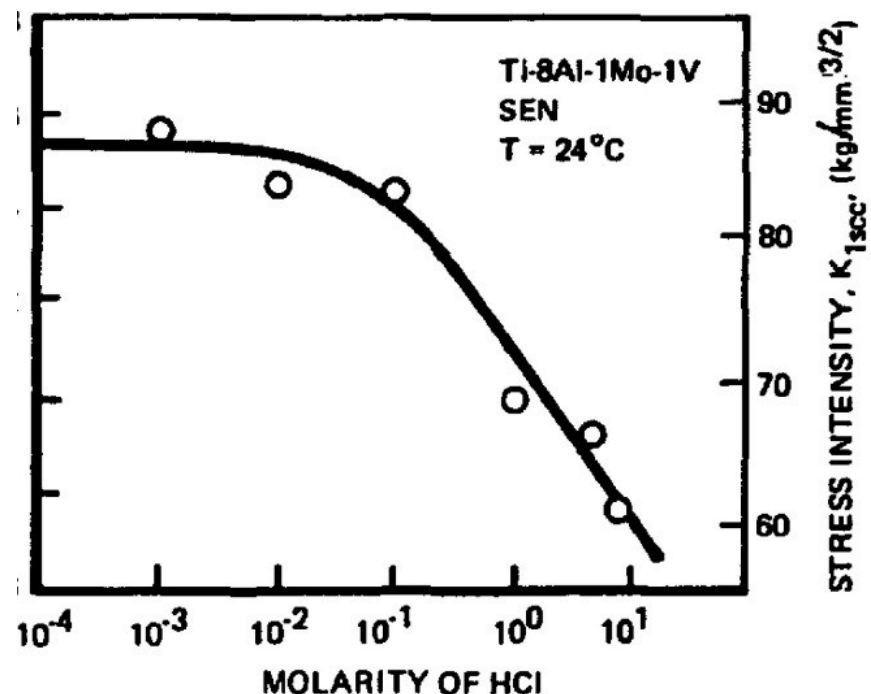


Fig. 1.30 Effect of hydrogen ion concentration in solution on SCC susceptibility of Ti-8Al-1Mo-1V [36]

Effect of Crystallographic Orientations

In titanium alloys, texture is physically originated from the anisotropy of HCP α phase, which has a limited number of slip systems [8, 9, 24, 79]. SCC sensitivity is related to the orientation between crystallographic texture and stress axis in Ti-6Al-4V [79] and Ti-8Al-1Mo-1V alloys [36, 80].

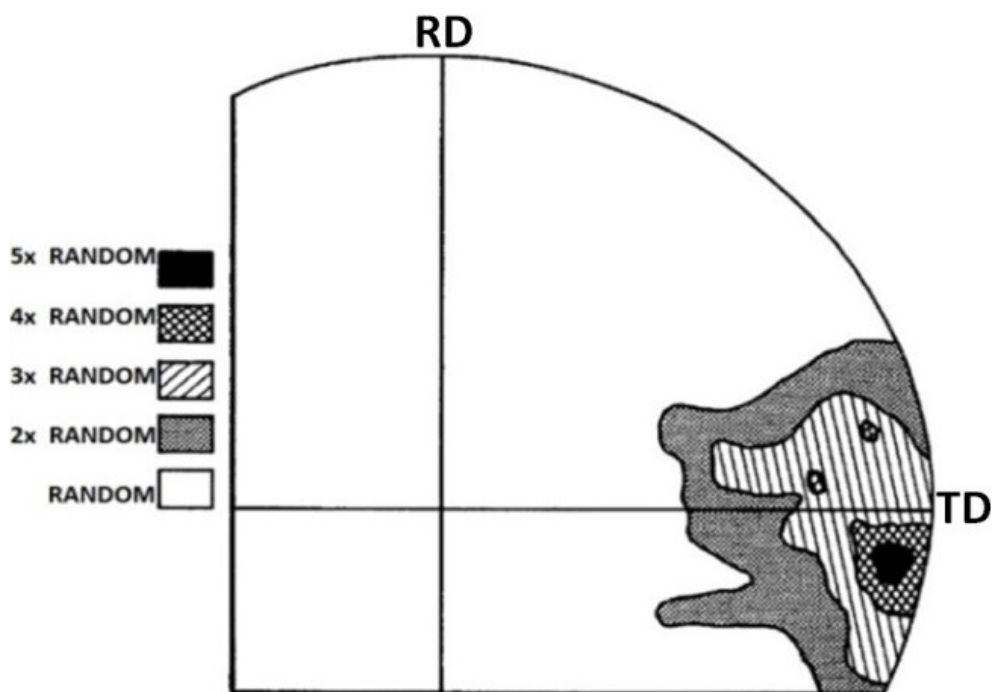


Fig. 1.31 Basal pole figure of hand wrought Ti-8Al-1Mo-1V plate [36]

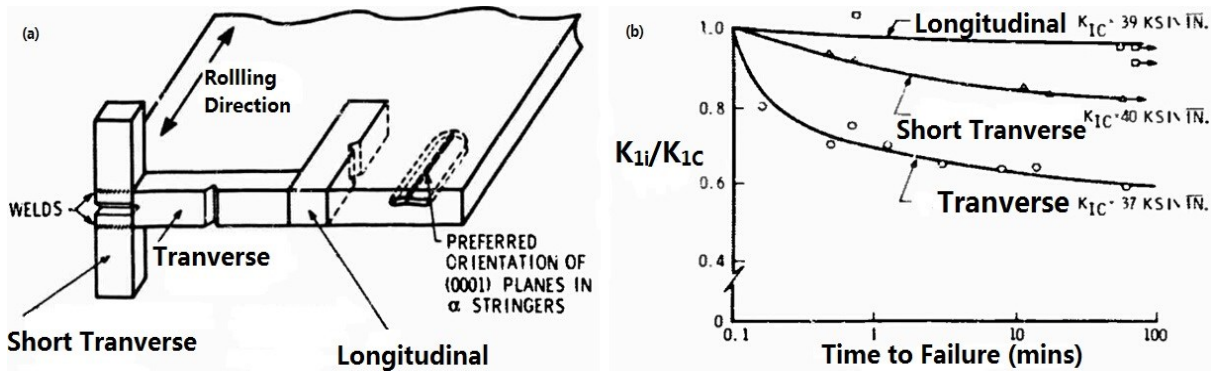


Fig. 1.32 (a) SCC specimen orientations, (b) stress-corrosion susceptibility as a function of specimen orientations in 0.6 M aqueous NaCl solution [36, 80].

In Ti-8Al-1Mo-1V, an intense transverse texture is presented in a rolled plate (Fig. 1.31), and the basal plane of α phase is aligned in the rolling direction and the c -axis is parallel to the transverse direction. Fig. 1.32a shows three SCC samples with different orientations from the rolled plate with texture illustrated in Fig. 1.31. In the longitudinal sample, the notch plane is normal to basal plane of α phase. However, it is parallel to the basal planes in the transverse sample. For the short transverse orientation, although the notch plane is perpendicular to the basal planes, its orientation is in the stage between that of the longitudinal and transverse samples. The relationship between SCC sensitivity and specimen orientation is described in Fig. 1.32b. It shows that SCC susceptibility is the highest when the notch plane has a parallel relationship with the basal planes (transverse sample). While there is no SCC susceptibility in the longitudinal sample with a perpendicular relationship between the notch plane and basal planes. The SCC sensitivity of the short transverse orientation lies in-between of the longitudinal and transverse samples [36, 80].

In addition to SCC susceptibility, the crack propagation direction has been reported to be related to the crystallographic texture in Ti-8Al-1Mo-1V. As illustrated in Fig. 1.33, crack propagation was found to be parallel to basal planes of α phase in double cantilever beam (DCB) samples. The parallel relationship is even observed in the sample with the notch plane perpendicular to $(0001)_\alpha$ plane.

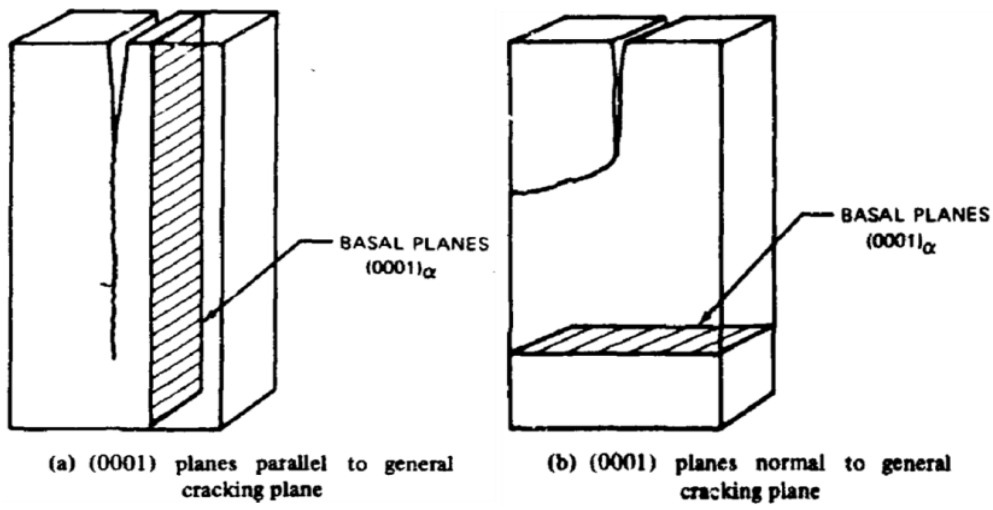


Fig. 1.33 SCC crack propagates parallel to the basal planes of α phase [36, 80].

Similar study of effect of texture has been conducted in Ti-6Al-4V [79]. A quantitative correlation of the crystallographic texture and SCC sensitivity in 0.6 M aqueous NaCl solution is shown in Fig. 1.34. There are two groups of microstructures, where EQ and CL represent equiaxed and coarse lamellar respectively, with five different processing/heating treating conditions. All the testing conditions have the tensile axis parallel to the c -axis of α phase [79]. The critical stress intensity factor (K_{ISCC}) is attenuated to be about one-half of K_{IQ} (fracture toughness in non-standard specimens) when the relative basal pole intensity is larger than 1 (random texture) [79]. It indicates that the SCC susceptibility increases with basal pole intensity, and attained relative SCC sensitivity of K_{ISCC}/K_{IQ} is close about 0.55.

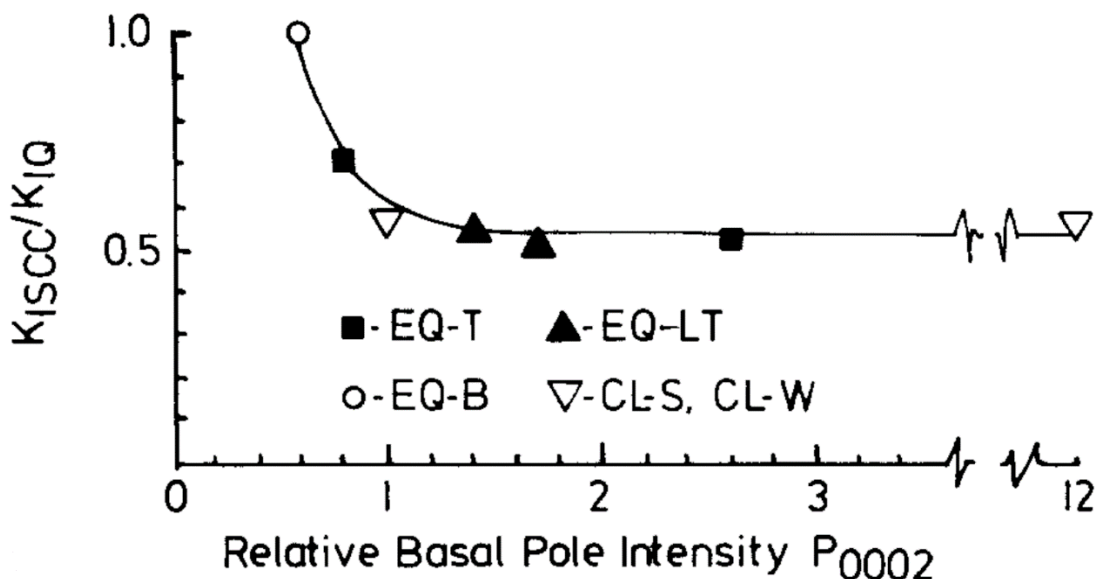


Fig. 1.34 Stress-corrosion susceptibility relative to basal pole intensity in tensile axis [79]

Effect of Presented Phases and Microstructure

Section 1.2.4 describes the possible phases in Ti-8Al-1Mo-1V, and they include α , β , martensite (α' and α''), and α_2 phases. Each phase has a different response to SCC, for example martensite is almost immune to SCC [36].

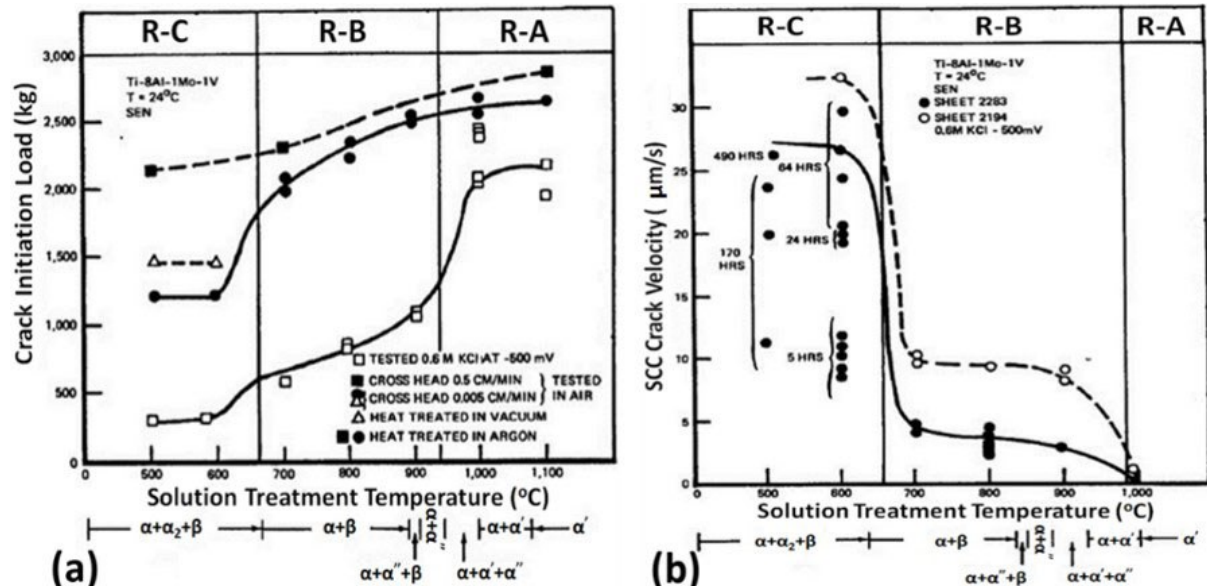


Fig. 1.35 Effect of presented phases on stress-corrosion cracking of Ti-8Al-1Mo-1V: (a) Crack initiation load, (b) Crack propagation velocity [36, 81]

A group of SCC tests was carried out on Ti-8Al-1Mo-1V with different solution heat treatment temperatures (see Fig. 1.35). R-A is the martensite microstructure quenched from high temperatures, and R-C is the microstructure with α_2 precipitates promoted by low temperatures aging treatment. It shows that martensite structure (R-A) was immune to SCC, while Ti-8Al-1Mo-1V with α_2 precipitates (R-C) had the highest SCC susceptibility [36, 81]. Ti-8Al-1V with a bi-modal microstructure (R-B) lies in the range of intermediate susceptibility, and the SCC susceptibility decreases with increasing amount of β phase [36, 64, 81]. J. C. Williams showed that in Ti-8Al-1Mo-1V aging treated at 260 °C for 10,000 hrs, ω precipitations are present and the SCC crack velocity was doubled compared to the parent material without aging [25, 36]. Therefore, both ordered α_2 and ω phases increase the SCC susceptibility in Ti-8Al-1Mo-1V.

Quenching of Ti-8Al-1Mo-1V from high temperatures leads to massive martensites or “packet martensites” (α') with a hexagonal symmetry, and massive martensites contains parallel martensite plates with a same burgers orientation [8, 36]. SCC immunity of α' martensites is attributed to the martensite boundaries and small martensite dimension associated with rapid cooling. The distribution of dislocation in α' martensite of Ti-8Al-1Mo-1V is planar slip, and the martensite boundaries are strong barriers for dislocation, which cannot be penetrated by glide bands [36]. In a study of longitudinal boundaries of hexagonal martensites [82], the interface consists of $1/3 <2\bar{1}\bar{1}3>$ type dislocations and the separated martensite plates consist of $1/3 <11\bar{2}0>$ type dislocations. This indicates that the glide dislocations cannot directly slip across the martensite boundaries. Therefore, martensites provide a much shorter effective slip length for planar slip, and prevent the SCC to occur.

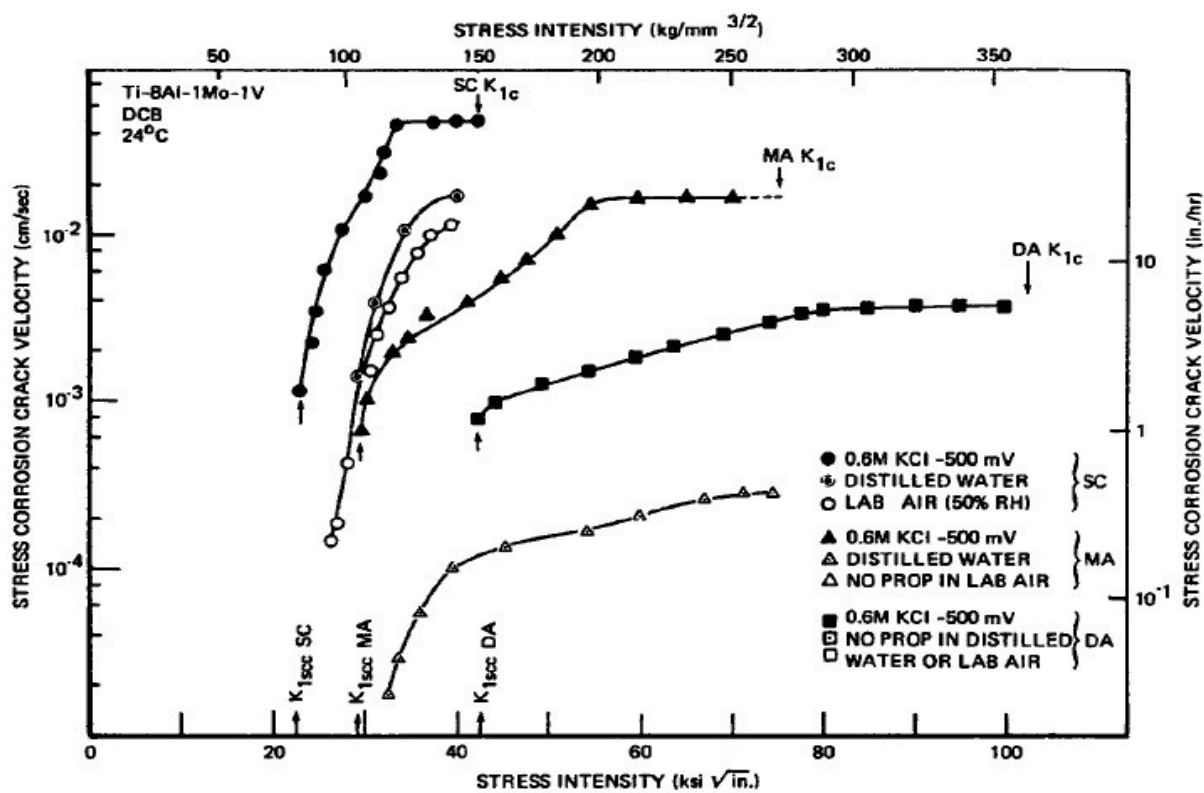


Fig. 1.36 Crack propagation velocity versus stress intensity factor for Ti-8Al-1Mo-1V with 3 different processing routes, SC (step cooled - solution treated at 820°C and then step-cooled to 450°C): designed to promote α_2 precipitation, MA (wrought annealed - solution treated at 820°C and then furnace-cooled): equiaxed microstructure with α_2 precipitates formed during the cooling , DA (duplex annealed - solution treated at 820°C and then water-quenched): bi-modal microstructure with no α_2 precipitates [36].

Alloy additions also have influences on the response to SCC. The SCC susceptibility is enhanced with increasing Al and O content, which is attributed by the stabilizing effects of α_2 precipitates [11, 13, 83]. As described in section 1.2.4, the precipitation of ordered α_2 phase occurs in Ti-8Al-1Mo-1V when aging at appropriate temperatures. From the corrosion point of view, α_2 precipitates also influence the electrochemical reaction at the crack tip [13]. Coherent and fine α_2 precipitates can be sheared by moving dislocation, and then continuous slip will happen on the active slip plane, which is easier compared to initiating a new slip on other ordered planes. Ordering suppresses cross slip and promotes planar slip, and the slip localization decreases the degree of crack tip blunting and maintains a sharp crack tip with a large stress concentration during the SCC crack propagation [8, 13, 83, 84].

Fig. 1.36 illustrates SCC crack propagation velocity of Ti-8Al-1Mo-1V with three different microstructures. Threshold stress intensity (K_{ISCC}) is a critical value, below which there is no SCC crack propagation. It shows that SC has the highest stress-corrosion susceptibility due to the presence of α_2 precipitations [36]. MA (fully equiaxed) has a lower K_{ISCC} than DA (bi-modal). This may be attributed by the interconnected primary α grain in fully equiaxed microstructure, which provide a longer effective slip distance for dislocations.

1.5.4 Role of Hydrogen in SCC of Titanium Alloys

According to the SCC mechanisms in section 0, there are several mechanism involves hydrogen. Hydrogen may be also involved in SCC of Ti-811. An indication is the R-B region in Fig. 1.35, the SCC susceptibility decreases with increasing amount of β phase in Ti-8Al-1Mo-1V with a bi-modal microstructure [36, 81]. As hydrogen has a much higher solubility and diffusivity in β phase due to the open BCC crystal structure than those in HCP α phase, SCC susceptibility decreases with increasing β phase volume fraction.

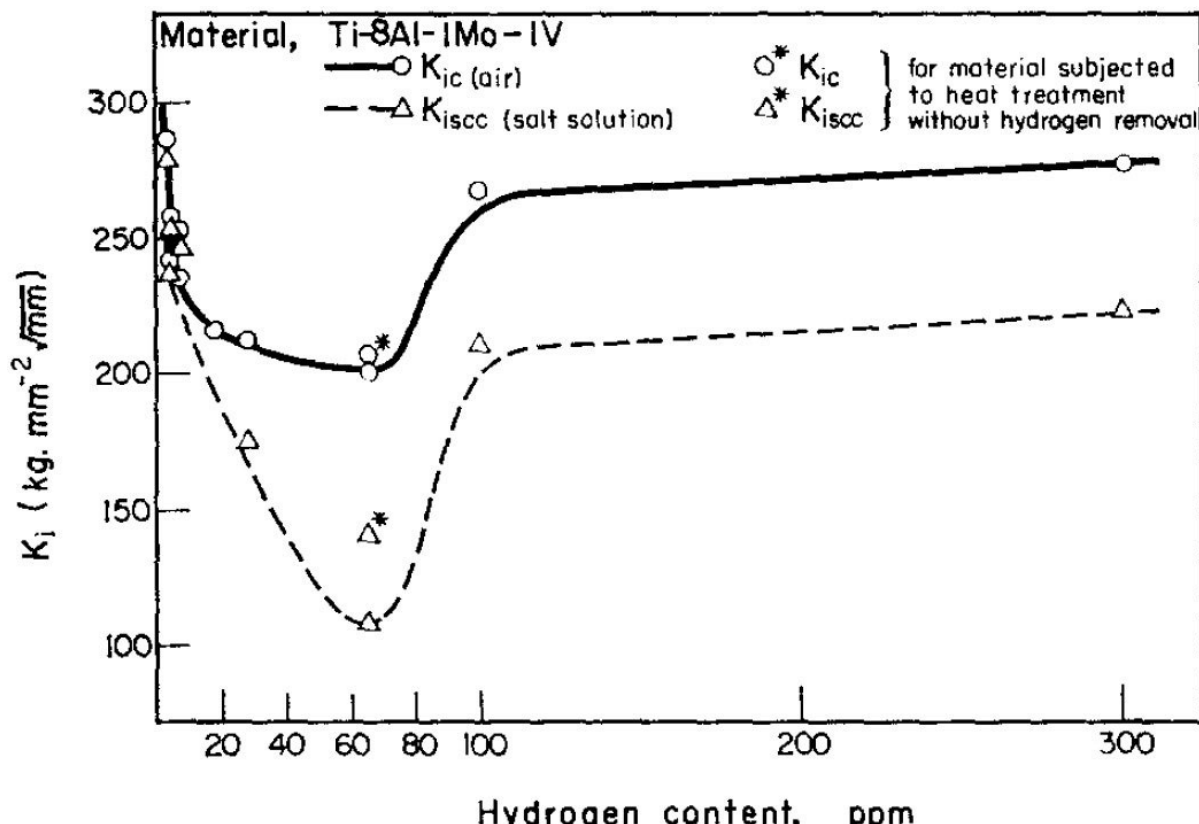


Fig. 1.37 Fracture toughness (K_{Ic}) and threshold SCC stress intensity (K_{ISCC}) of Ti-8Al-1Mo-1V with various hydrogen contents [16].

Another example is a fracture toughness study of Ti-8Al-1Mo-1V in Fig. 1.37 (equiaxed microstructure). Hydrogen content has an influence on the fracture toughness (K_{Ic}) in air and threshold SCC stress intensity (K_{ISCC}) in salt solution. Ti-8Al-1Mo-1V is not susceptible to NaCl SCC when it has hydrogen concentrations below 5 ppm. However, it is quite interesting that there is a transition in hydrogen effect at 65 ppm. Both of K_{Ic} and K_{ISCC} firstly decrease to the transition and then increase with increasing hydrogen content [16, 22]. There is no satisfying explanation for the above phenomenon in the published work [16]. A hypothesis could be that there is a fracture mode transition at 65 ppm. The effects of hydrogen pre-charging have been investigated in Ti-6Al-4V [22]. The crack propagation was found to be transgranular at low hydrogen concentrations, but intergranular crack along α/β interface was observed at high hydrogen concentrations. As α titanium has a low hydrogen solubility compared to that of β phase. The susceptible location of α/β interface is due to either the hydrides formation or hydrogen supersaturation at the interface [22]. Similar results have been published in a HE

study of Ti-4Al [67], it has been observed that hydride formation and fracture is the mechanism at low crack propagation rate conditions, while hydrogen enhanced localized plasticity at high crack velocities [67]

As mentioned in section 1.1, the SCC issue is related to a localized planar slip due to the presence of ordered Ti_3Al (α_2) precipitates in α phase of Ti-8Al-1Mo-1V [10, 11, 14, 15]. As shown in Fig. 1.38, interstitial hydrogen has been found to have interaction with dislocations. The dislocation velocity is increased by the hydrogen pressure in an in-situ TEM study. They also found that hydrogen reduce the critical stress for dislocation motion [67]. G. Lu [74] found that hydrogen promotes dislocation emissions at the crack tip and increases dislocation (including the edge, screw, and mixed dislocations) velocity significantly in aluminium. According to his calculation, Peierls-Nabarro stress of dislocation has been reduced by more than an order of magnitude when hydrogen is presented, and hydrogen has a strong binding to dislocation cores. The hydrogen binding energy is a function of dislocation characters, the edge dislocation or edge component in mixed dislocation has a high hydrogen binding energy. Therefore, it will cost much more energy for an edge dislocation to cross slip into a screw dislocation, and it is the same story for the edge component in the mixed dislocation. As a result, hydrogen inhibits cross-slip and promotes planar slip [74]. The concept of interaction between hydrogen with dislocations described above is similar to what happened in SCC for $\alpha+\beta$ titanium alloys, and it is an indication that the operating mechanisms involving hydrogen.

The hydrogen source could be either external absorbed or internal solute hydrogen. As illustrated in Fig. 1.15, the titanium oxide film is stable in neutral pH solution at OPV range from -0.38 V to 0.12V (SHE). As a result, hydrogen absorption seems to be not feasible in neutral NaCl SCC solution.

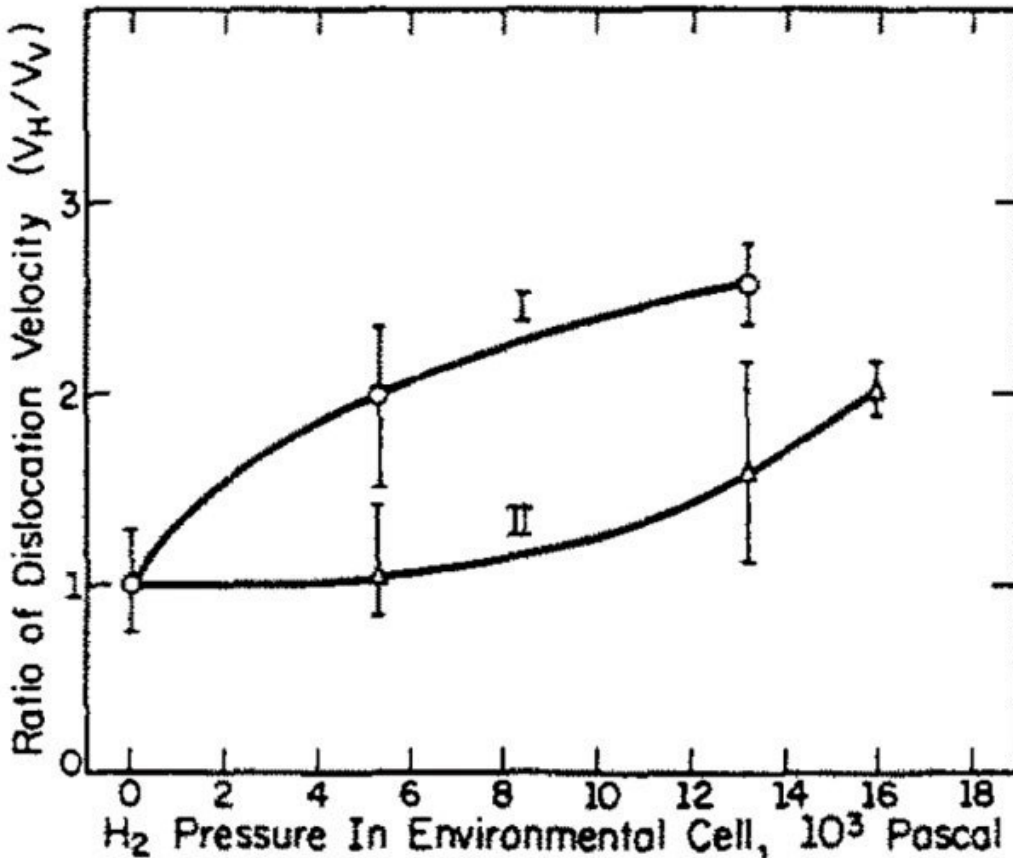


Fig. 1.38 The effect of hydrogen on dislocation velocity, I: the first introduce of hydrogen into the environment cell, II: hydrogen introduced by stage I has been removed and then re-introduced into the environment cell [67].

However, the local corrosion environment within the SCC crack may be different to that of bulk solution. A similar electrochemistry situation is the crevice corrosion, which is also a differential aeration cell. Fig. 1.39 shows that there is a dramatic decrease in the potential and pH within the crevice after 3 hours in a CP titanium alloy. The pH can be as low as 1, and the crevice potential is about -0.4V (SHE) [85]. In another aqueous SCC study of Ti alloys [64], pH is below 2 at the tip zone for a neutral bulk solution (see Fig. 1.40). The low pH (high hydrogen ion concentration) is a result of oxygen depletion in the vicinity fluid around crack tip, anodic reaction of titanium and subsequent hydrolyzation of titanium ions. Therefore, titanium oxide film is not stable at the SCC crack tip region [64].

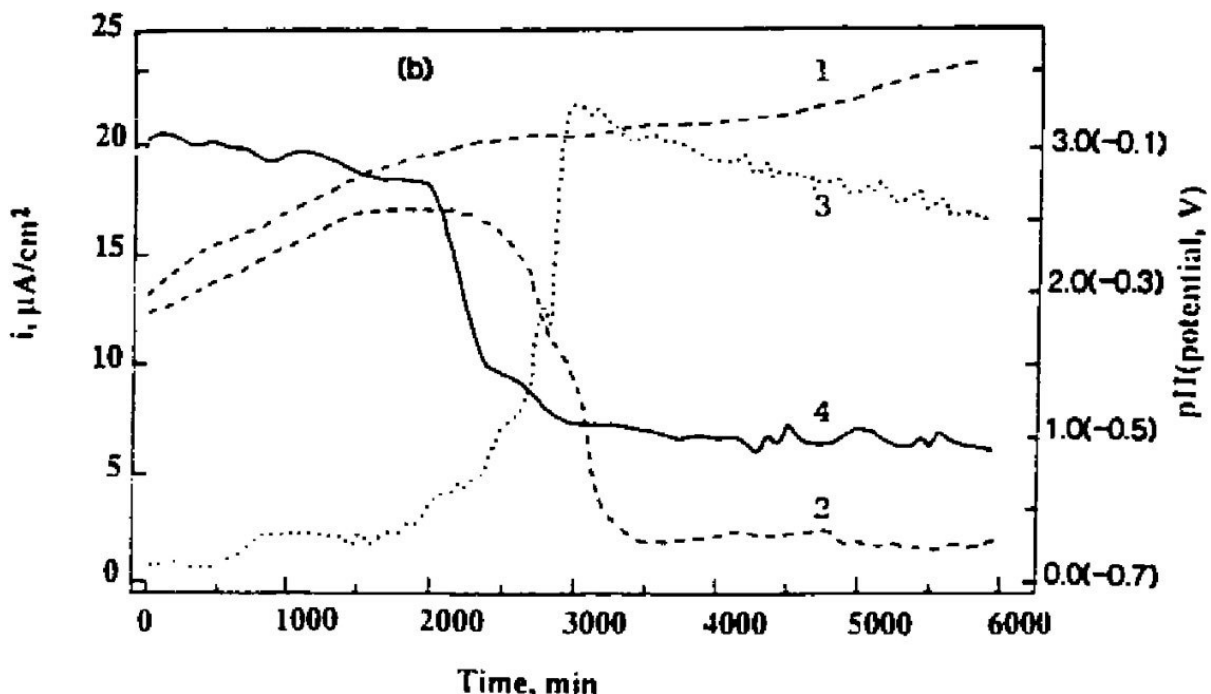


Fig. 1.39 Current, pH, and potential distribution of the fluid within crevice as a function of time for a CP titanium alloys in neutral solution, (1) potential of the Ti sample outside the crevice, (2) potential of the Ti sample inside the crevice, (3) corrosion current, (4) crevice pH. The electrode potential is referenced to the Ag/AgCl (0.1 M KCl) electrode [85].

In order to balance the charge of positive titanium cations created by the anodic dissolution, Cl⁻ will diffuse into the tip region and increase the local Cl⁻ concentration [64, 85]. As described in section 1.5.3, the SCC susceptibility increases with the Cl⁻ concentration [36]. In addition, the presence of Cl⁻ reduces the crack tip potential which facilitates the hydrogen absorption [64].

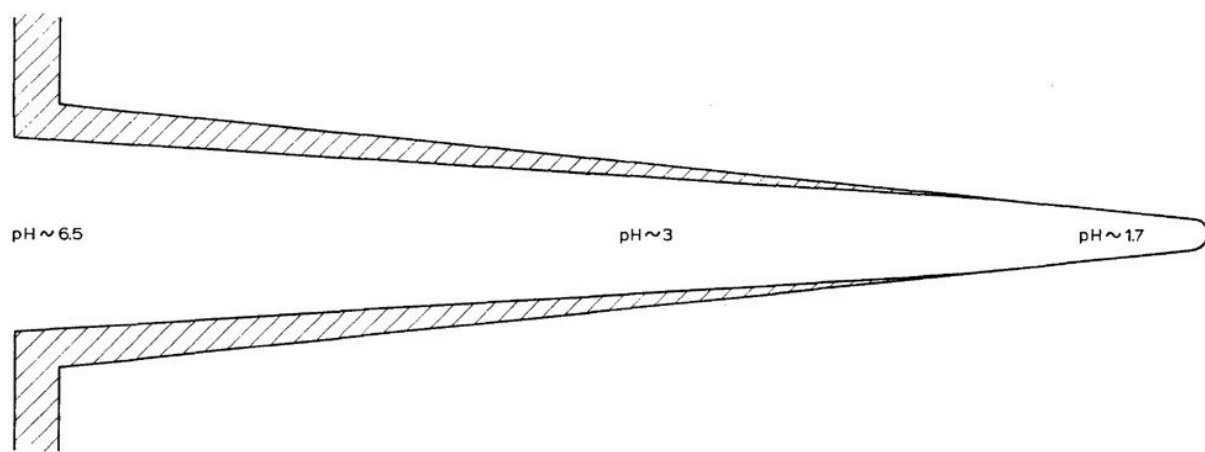


Fig. 1.40 pH distribution of the fluid within the aqueous SCC crack for titanium alloys in neutral solution [64].

Hydrogen is an interstitial element in Ti alloys, and its solubility and diffusivity are much higher in β phase compared to in α phase due to the low pack density of BCC crystal. As a result, a more rapid diffusion of absorbed hydrogen can be achieved by the interconnected β phase “highway”[22]. In addition, there will be a hydrogen concentration gradient developed around the crack tip during SCC [86]. Following equation describes the diffusion Coefficient [87]:

$$D_H = D_{H0} \cdot e^{(-Q/RT)} \quad (1.4)$$

where D_{H0} is the frequency factor, Q is the activation energy and R is the gas constant at 8.314 J/(mol·K). Tab. 1.3 are references of the frequency factor and activation energy for two titanium alloys [87, 88], and it includes the calculation of diffusion coefficients at 300K based on Equation 1.4. The results shows that the β -titanium has a two orders of magnitude higher diffusion coefficient than that of a near α titanium (IMI 834) alloy.

Tab. 1.3 The frequency factor (D_{H0}) and activation energy (Q) for α and β titanium alloys [87, 88].

	Frequency factor (D_{H0})	Activation energy (Q)	Diffusion coefficient (D_H) at 300K
IMI 834	$274 \times 10^{-9} \text{ m}^2/\text{s}$	40.3 kJ/mol	$2.63 \times 10^{-14} \text{ m}^2/\text{s}$
β -titanium	$200 \times 10^{-9} \text{ m}^2/\text{s}$	27.8 kJ/mol	$2.89 \times 10^{-12} \text{ m}^2/\text{s}$

In addition to lattice diffusion, pipe diffusion is possible when there are slip bands in the materials. Hydrogen diffusivity can be increased by transportation through dislocations [30, 89], especially for the presence of planar slip bands which allow longer slip length [30, 90, 91]. Moreover, the hydrogen atmosphere around the dislocations is able to be dragged by the moving dislocations [92]. Hydrogen transport through slip bands has been reported in various systems including steel [93], Al [90], and Ti [30, 92]. Pipe diffusion is kinetically preferred to volume diffusion, and the hydrogen diffusion rate was increased by orders of magnitude through the pipe diffusion [89, 90].

CHAPTER II: RESEARCH OBJECTIVES

The literature reviewed in Chapter II described the effect of Ti_3Al (α_2) precipitates and texture on SCC properties for Ti-8Al-1Mo-1V. An interesting phenomenon in literature review (Chapter II) is that those effects of α_2 , microtexture, and α' martensite are related to dislocations in either promoting the planar slip or influencing the effective slip length for glide bands. Therefore, Powder hot isostatic pressed (HIPped) materials without crystallographic microtexture provides a unique way to evaluate the effect of slip length on SCC sensitivity.

However, all previous studies were conducted in conventionally processed materials (eg. rolled plate) with an intrinsic texture. The effect of α_2 precipitates can be ambiguous in a textured material. The independent study of effects of α_2 can be conducted on powder hot isostatic pressed (HIPped) materials without crystallographic microtexture.

In the current study, the main aims are:

- (i) to determine the individual effect of microtexture and the independent effect of α_2 precipitates on SCC properties by comparing the following samples:
 - a. Wrought Ti-811 sample: Wrought Ti-8Al-1Mo-1V bar, which has α_2 precipitates and a pronounced microtexture.
 - b. Wrought Ti-811 + HT860 sample: The wrought Ti-8Al-1Mo-1V bar is heat treated in a designed scheme to suppress α_2 phase transformation, and it has microtextured regions but no ordered α_2 precipitates.
 - c. HIPped Ti-811 sample: Powder hot isostatic pressed (HIPped) Ti-8Al-1Mo-1V, which has a microstructure containing α_2 precipitates without crystallographic microtexture.

- d. HIPped Ti-811 + HT860 sample: Powder Hot HIPped Ti-8Al-1Mo-1V is heat treated in a designed scheme to suppress α_2 phase transformation, and it does not have any ordered α_2 precipitates and crystallographic microtexture.
- (ii) to improve the SCC resistance of Ti-8Al-1Mo-1V alloy by manipulating the α_2 precipitation and microtexture.
- (iii) to understand and identify the SCC mechanism(s) in Ti-8Al-1Mo-1V alloy by reveal the difference of dislocations substructure between the pre-crack (fractured in air) and SCC crack (failed in 0.1M NaCl aqueous solutions) regions.

The study aims to test following hypothesis:

- (i) Both α_2 precipitates and microtexture play a role in SCC of Ti-8Al-1Mo-1V. The effect of α_2 precipitates is promoting planar slip, and microtexture influences the SCC crack propagation.
- (ii) Removal of both α_2 and microtexture is necessary for the inhibition of SCC in Ti-8Al-1Mo-1V.
- (iii) The deformation mode (eg. types of dislocation) in the formation of SCC facets should be different to that for ductile dimples formation.

Experimental methods used to investigate the above aims were standard. A wide range of techniques are used to investigate the effect of α_2 precipitates and microtexture on SCC. It was hoped that the results provide new insights into the SCC mechanism(s) for Ti-8Al-1Mo-1V alloy. It is believed that this work is important for the research in the SCC of near α and $\alpha+\beta$ Ti alloys. The used experimental techniques include:

- SEM to characterise grain sizes and morphologies, and to exam the SCC fracture surfaces.
- EBSD to characterise the texture and microtexture.

- Tensile tests to measure the mechanical properties in samples with different processing methods and post heat treatments.
- FIB lift-out technique to extract small volumes of material underneath the fracture surfaces.
- “Transmission”-EBSD (T-EBSD) to characterise the grain orientations and Schmid factors of the FIB lift-out lamellae.
- TEM to characterise the α_2 precipitation in samples with different heat treatment conditions, and to analyse the dislocation substructure in α grains underneath fracture surfaces.

CHAPTER III: EXPERIMENTAL METHODS

3.1 Materials and Heat treatment

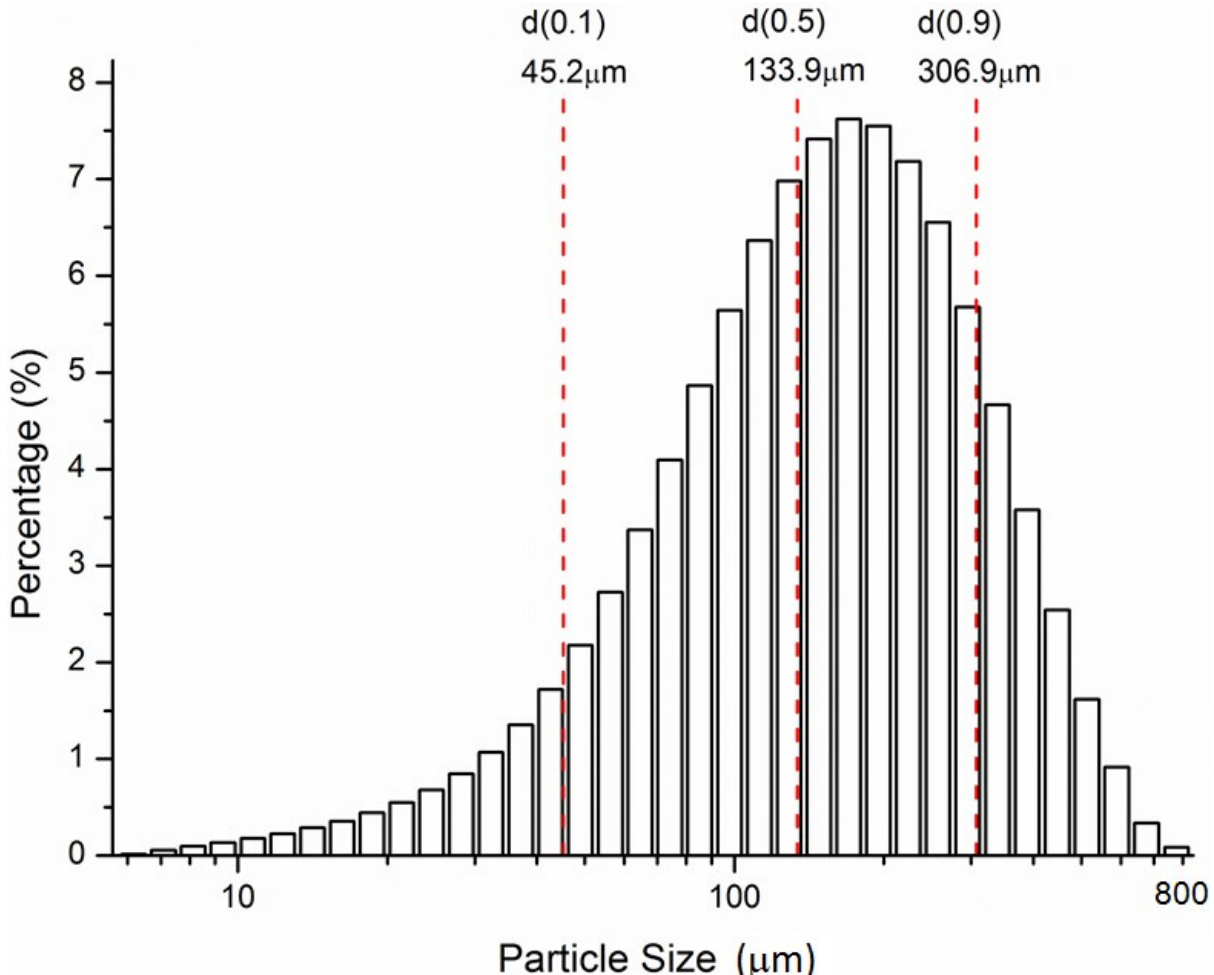


Fig. 3.1 Ti-8Al-1Mo-1V pre-alloyed powder particles size distribution.

Two materials were used in this study. One was wrought Ti-8Al-1Mo-1V bar with a diameter of 80 mm, which was obtained from Timet UK Limited. The other was powder hot isostatic pressed (HIPped) Ti-8Al-1Mo-1V, in which electrode induction melting gas atomization (EIGA) pre-alloyed Ti-811 powder was provided by IMR, Chinese Academy of Science. Powder size distribution was measured by Mastersize 2000 particle sizer analyzer. In the particle size measurement, the used refractive index was 2.22 for titanium alloys [94-96]. The

pre-alloyed powders had a wide particle size distribution from 5 μm to 832 μm , with 90% having a diameter less than 307 μm . (see Fig. 3.1).

Fig. 3.2a illustrates the morphology of the pre-alloyed powders. Size of these round Ti-811 particles are in the range of the distribution measured by the Mastersize analyzer (Fig. 3.1). Most of particles have a smooth surface except a few with satellites attached. Fig. 3.2b reveals a fine fully lamellar microstructure within pre-alloyed particles. The α lath thickness is less than 2 μm , which is a result of a high cooling rate during the gas atomization process.

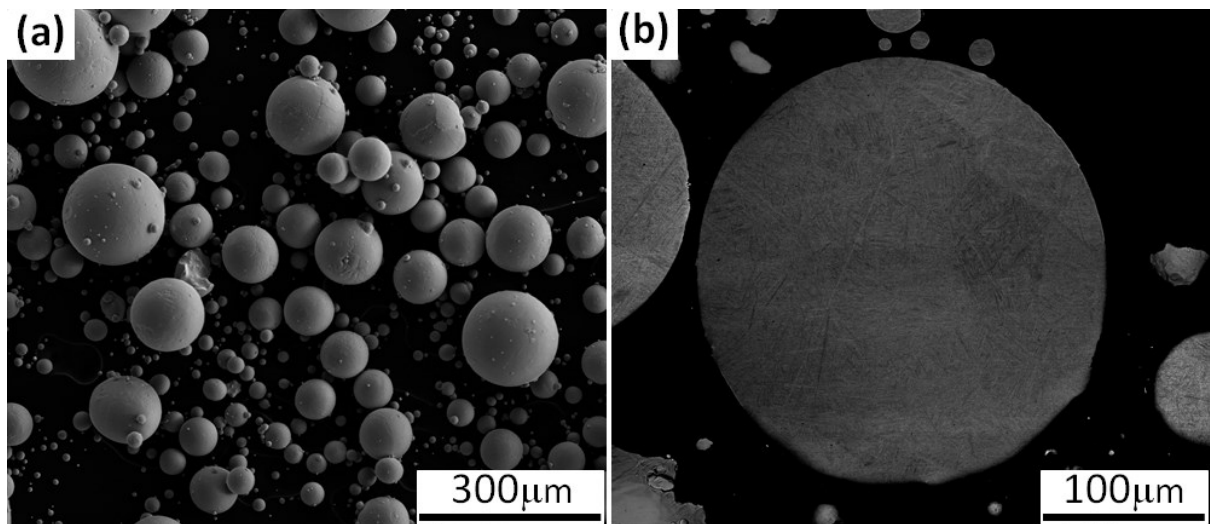


Fig. 3.2 Ti-8Al-1Mo-1V pre-alloyed powder: (a) secondary electron (SE) image of an overview for powder size distribution, powders were attached to a conductive carbon tape, (b) backscatter electron (BSE) image shows the Ti-8Al-1Mo-1V pre-alloyed powder with a fully lamellar microstructure, powders were mounted in conductive resin.

A phase diagram calculation of Ti-Al-Mo-V alloy system was carried out by PANDATTM software. An isopleth was obtained with the weight percentage of Mo and V being fixed at 1 Wt. % (Fig. 3.3). The intersection points of red dashed lines show that the ordering transformation temperature of α_2 (Ti_3Al) phase starts from 837 °C, and the β transus is at 1028 °C for Ti-8Al-1Mo-1V.

In a study of HIPped Ti-6Al-4V [97], it was found that a better balance of properties had been obtained at hot isostatic pressing (HIPping) temperatures, which are slightly lower than the β transus. Therefore in the current study, the pre-alloyed powders were encapsulated in mild steel

cans and HIPped by Avure QIH-9 Hot Isostatic Press at 100 MPa and 990 °C (the β transus at 1028 °C) for four hours with a ramp rate of 5 °C/min.

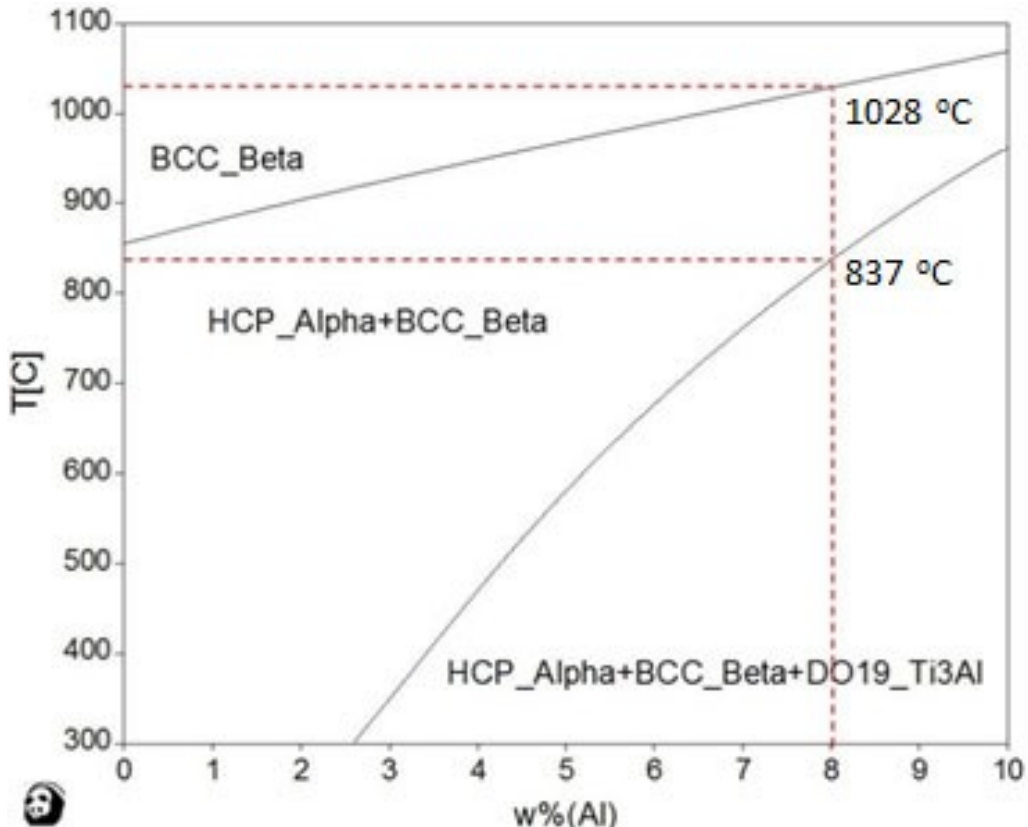


Fig. 3.3 Calculated isopleth of Ti-Al-Mo-V alloys with weight fraction of Mo and V being fixed at 0.01.

Hot isostatic pressing (HIPping) is a powder metallurgy technology, in which isostatic pressure and high temperature are applied simultaneously to give a uniform shape reduction and achieve a density up to 99.99% (see Fig. 3.4). HIPping is suitable to produce complex shape components for materials, including tooling steels, superalloys, titanium alloys, and ceramics [8, 10, 23, 98-101]. HIPped parts have fine, homogeneous and isotropic microstructures with no crystallographic texture [23, 98, 102, 103]. Therefore, HIPped Ti-8Al-1Mo-1V provides the opportunity to investigate the effect of texture or rather the absence of it on SCC.

In Fig. 3.5, a post heat treatment of 30 minutes at 860 °C followed by water quench (WQ) was designed to suppress α_2 phase formation. As the martensitic transformation start temperature (M_s , the black dashed line) and α_2 ordering transformation temperature (the blue dashed line) are

about 900 °C [11] and 837 °C (see Fig. 3.3) respectively. WQ from 860 °C would prevent both the martensitic and α_2 transformation. Martensite microstructures have been identified as immune to SCC in Ti-8Al-1Mo-1V [36, 81]. Therefore, it was important to avoid the formation of martensite in the study. The temperatures were monitored by using a K-type thermocouple with COMARK N9002 thermometer (COMARK Instruments, Norwich, UK) during the post heat treatment on all samples, and the temperature variations were limited to ± 3 °C. All the samples had been encapsulated in vacuum before the heat treatment to avoid oxidation.

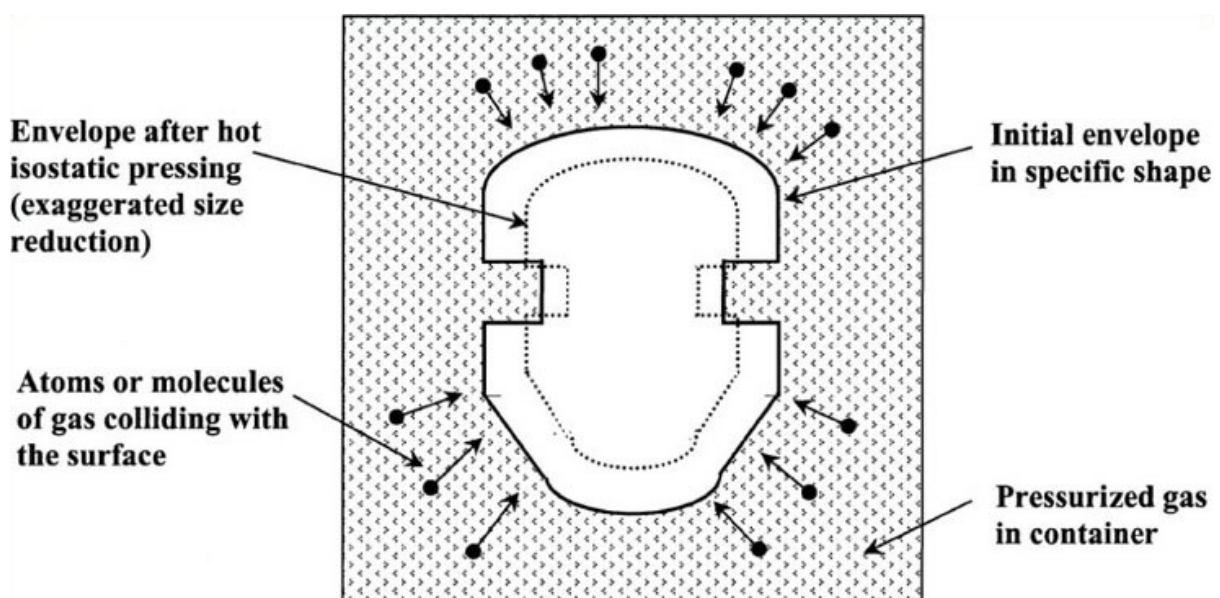


Fig. 3.4 Illustration of hot isostatic pressing (HIPping) [99]

The description and chemical composition of the four different sample conditions employed in this study are presented in Tab. 3.1 and Tab. 3.2. The orientation of double cantilever beam (DCB) specimens for SCC tests is also described in Tab. 3.1 for the wrought bar (includes the post heat treated samples). As the powder HIPped Ti-8Al-1Mo-1V sample has a random texture, there is no specific orientation in the DCB sample for SCC tests. The wrought Ti-811 and HIPped Ti-811 samples had a similar composition in Al, Mo, V, O and H. As the post heat treatment was conducted in vacuum atmosphere, a chemical composition change was not expected for samples wrought Ti-811 + HT860 and HIPped Ti-811 + HT860.

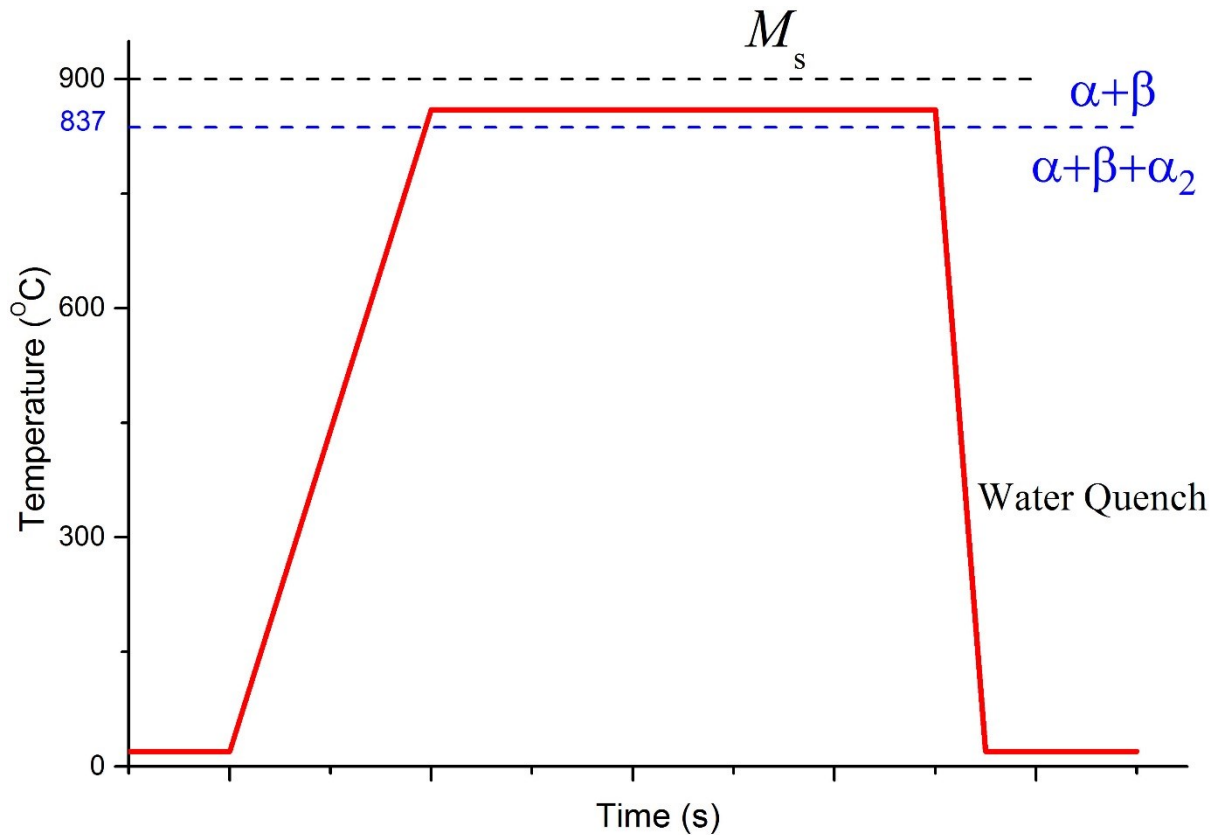


Fig. 3.5 Illustration of a post heat treatment: 30 minutes at 860 °C followed by water quench (WQ). The black dashed line is the martensitic transformation start temperature (M_s) at 900 °C [11], the blue dashed line is the α_2 ordering transformation temperature at 837 °C.

Tab. 3.1. Descriptions of various Ti-811 samples studied.

Samples ID	Description
Wrought Ti-811	Sample with a C-L orientation in the wrought Ti-811 bar was used for SCC tests. C-L indicates the loading direction-crack opening direction in the Double Cantilever Beam (DCB) specimen (Fig. 1). In the Ti-811 bar, R: radial direction, C: circumferential direction, and L: longitudinal direction. (see Fig. 3e)
Wrought Ti-811 + HT860	Wrought Ti-811 was subjected to a post heat-treatment at 860 °C/30 min + water quench (WQ). DCB samples with the same C-L orientation was used for SCC tests.
HIPped Ti-811	Powder HIPped Ti-811 at 100 MPa, 990 °C for four hours with a ramp rate of 5 °C/min.
HIPped Ti-811 + HT860	HIPped Ti-811 was subjected to a post heat-treatment at 860 °C/30 min + WQ.

Two DCB specimens (Fig. 3.7) were prepared for SCC tests in all the four conditions as listed in Tab. 3.1.

Tab. 3.2. The chemical composition of various tested samples.

	Wrought Ti-811 and wrought Ti-811 + HT860	HIPped Ti-811 and HIPped Ti-811 + HT860
Al (Wt.%)	7.94	7.97
Mo (Wt.%)	1.04	0.99
V (Wt.%)	0.99	0.99
C (ppm)	60	90
O (ppm)	950	760
H (ppm)	34	24
Ti	Bal	bal

The inert gas fusion method was used for measuring O (ASTM E 1409-13 [104]) and H (ASTM E 1447-09 [105]) contents, and the direct current plasma method was applied to the composition measurement of all the other elements

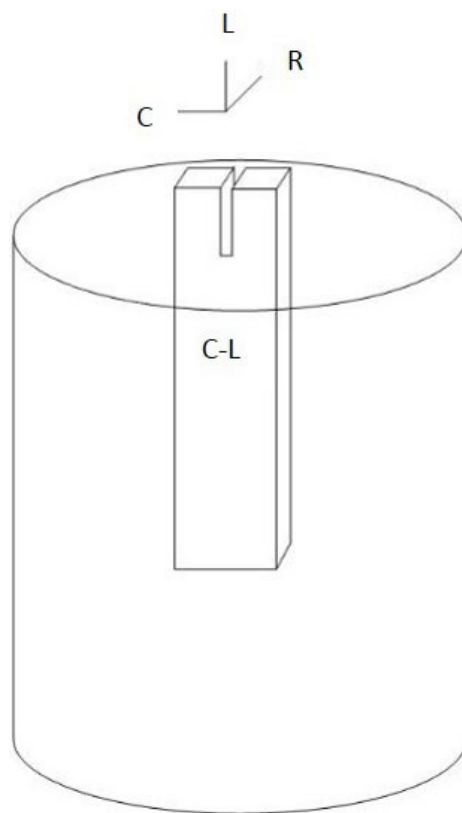


Fig. 3.6 Illustration of a DCB sample with a C-L orientation in the wrought Ti-8Al-1Mo-1V bar.

3.2 SCC Tests and Mechanical Tests

According to the SCC test standard ASTM G168-00 [106], Double Cantilever Beam (DCB) samples were pre-cracked by mechanical overloading in air before immersing them into the test solution. The constant displacement was produced by tightening two stainless steel bolts in the DCB specimen (see Fig.A3 in appendix and Fig. 3.7). In order to conduct a study of sample orientations (which is not included in this paper), DCB samples were sectioned from the wrought Ti-811 bar with different orientations. Therefore, sample length (76 mm in Fig. 3.7) was limited by the wrought Ti-811 bar diameter at 80 mm.

For each condition as shown in Table 1, two tests were carried out. The test solution (pH 5.7) was 0.1 M NaCl, made from distilled water and Analar grade reagent NaCl. The solution volume was 150 ml and open to air at room temperature. A fresh solution was used for each individual test. The specimen potential was allowed to remain at the open circuit potential for the duration of SCC tests. The interim crack length (a_i in Equation 3.1) was measured periodically by marking the crack front on both surfaces of a specimen using a scalpel under an optical microscope. The measurement frequency was higher during the initial stage of a test as the crack propagation rate was high. The stress intensity and crack propagation rate decrease during constant displacement SCC tests with increasing crack length, so the measurement frequency was reduced. The crack propagation velocity was then calculated from the increase in crack length and time interval. The stress intensity factor, K_{Ii} , is a function of a_i , and it was calculated using the following Equation 3.1 [106]:

$$K_{Ii} = \frac{[1.732EV_{LL}]}{\left[4H^{0.5}\left(\frac{a_i}{H}+0.673\right)^2\right]} \quad (3.1)$$

where a_i is the interim crack length (m), K_{li} is the stress intensity factor (MPa· \sqrt{m}), V_{LL} is the crack opening distance on the loading axis (m), H is the sample half height (m), and E is the Young's Modulus (MPa). As shown in Equation 3.1, the stress intensity factor (K_{li}) decreases as a function of increasing crack length during crack propagation. After the SCC tests, polynomial curve fittings were applied to the SCC crack velocity and corresponding stress intensity factor based on a previous work [107], and associated confidence bands (95 confidence level) were generated to evaluate the accuracy of curve fitting. In this work, the K_{ISCC} is defined as the stress intensity factor when crack velocity is 10^{-10} m/s, and K_{ISCC} is computed based on the curve fitting function.

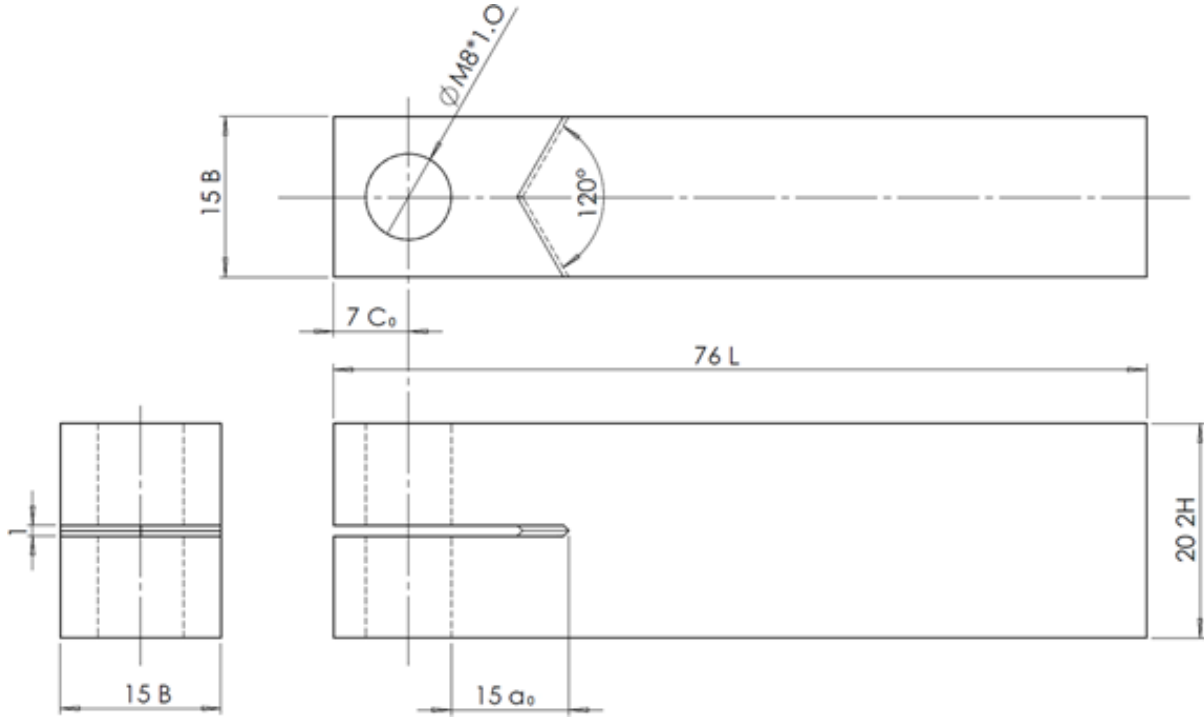


Fig. 3.7. Schematic diagram of Double Cantilever Beam (DCB) samples with dimensions (mm), a_0 – starting crack length, B – width, c_0 – distance from sample edge to loading axis, $2H$ – height, L – length.

In order to obtain a value of Young's modulus for use in Equation 3.1, round tensile specimens following ASTM E8/E8M–11 [108] standard with a diameter of 4 mm and a length of reduced section of 23 mm were prepared for all the sample conditions in Tab. 3.1. For wrought Ti-811 and wrought Ti-811 + HT860 conditions, the axial direction of tensile samples is parallel to the longitudinal direction of the Ti-811 bar. As there would be no texture in the

powder HIPped Ti-811, tensile samples do not have a specific orientation. Tensile tests were conducted for specimens loaded to fracture at a crosshead speed of 1 mm/min. Three repeated tests were carried out for all sample conditions. During the tensile tests, an extensometer was used to ensure the accuracy in strain measurement.

3.3 Microstructure and Fracture Surface Characterization

For microstructure characterization by scanning electron microscopy (SEM) and EBSD, all the samples were abraded with SiC paper to a 2400-P finish, and then polished with a mix of 15% (vol.) H₂O₂ and 85 % OP-S (Oxide Polishing Suspension) on a MD-Chem polishing plate. Post data analysis of microstructure, which includes grain size and volume fraction of presented phases, were processed by a Fovea ProTM plug-in of Photoshop.

Fractography study was carried out on the fractured DCB samples in SCC. Microstructure characterization and fractography examination were conducted by using a FEI Quanta 3D FEG microscope. Texture analysis were carried out by EBSD in a Quanta 3D FEG and JEOL JSM-7001F FEGSEM microscope. EBSD scan along the crack path was conducted at the sample half width, because the crack front was expected at half width due to the stress concentration produced by the chevron notch in the middle of each DCB specimen.

3.4 TEM Sample Preparation and Analysis

For the α_2 precipitation investigation, samples (wrought Ti-811, HIPped Ti-811, HIPped Ti-811 + HT860) were mechanically thinned down to 120 μm , and then electropolished by a twin jet polisher in the electrolyte containing 57 vol.% methanol, 40 vol.% n-butanol, and 3 vol.% perchloric acid. The electropolishing settings were 40 V and -32 °C. The foils were examined to obtain Selective Area Diffraction (SAD) patterns, Bright Field (BF) images, Dark Field (DF)

images, and High Resolution TEM (HRTEM) images in a FEI Tecnai G2 T20 TWIN TEM at 200 KV.

For the dislocation contrast analysis, Focused Ion Beam (FIB) was used to lift-out TEM foils perpendicular to both the fracture surface and crack growth direction from the pre-crack and SCC crack regions of wrought and HIPped Ti-811 samples by a FEI Quanta 3D FEG microscope with a dual (FIB-SEM) beam system (Fig. 3.8). The gallium (Ga) ion beam column was 52° tiled away from the vertical, thus sample was tiled to 52° during the milling process.

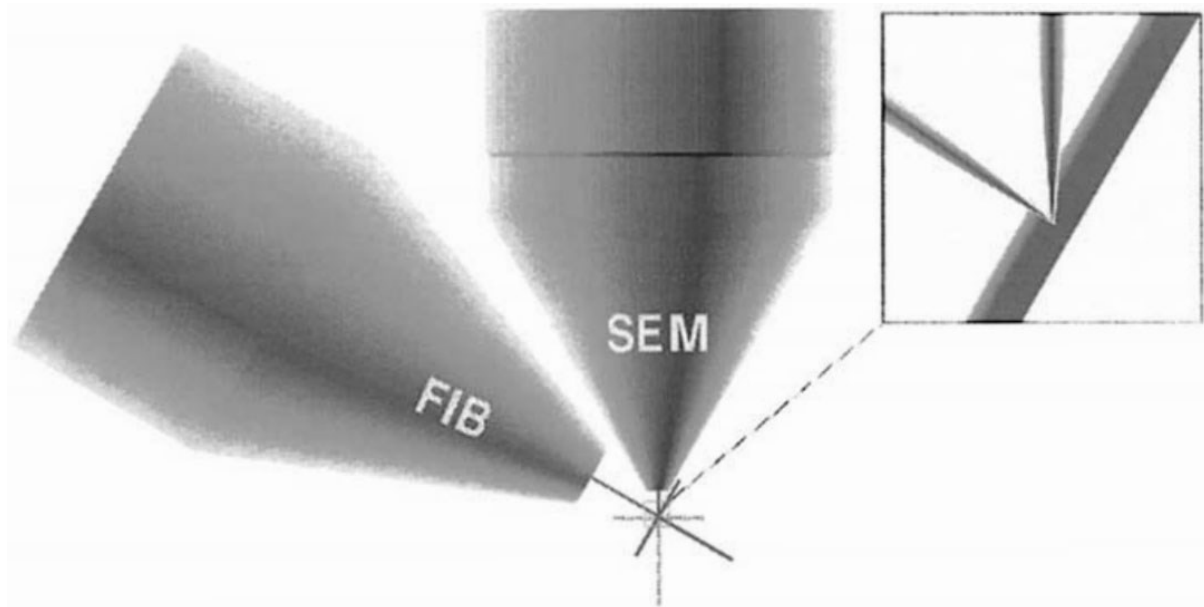


Fig. 3.8. Illustration of a dual (FIB-SEM) system, which is able to provide real-time SEM imaging during the FIB milling processes [109].

As shown in Fig. 3.9, fractures surface consists of pre-cracked region failed in air (highlighted by the blue arrow) and SCC faceted region failed in NaCl solution (highlighted by the red arrow). The pre-crack region is from the chevron notch to the crack arresting front in air (the blue dashed line). The SCC faceted region is between the crack arresting front in air (the blue dashed line) and in NaCl solution (the red dashed line). The convex fracture front is a result of the stress concentration caused by the chevron notch. Three FIB lift-out lamellae were prepared from the fracture surface in this study. According to Fig. 5.2, regions 1 and 2 were sectioned from the dimpled and faceted fracture surfaces of wrought Ti-811, and another lamellae

containing regions 3 and 4 was obtained from the faceted fracture surface of HIPped Ti-811 sample. For region 1 from the pre-crack dimples, the location of FIB lift-out is in the dimpled region close to the fracture mode transition border (the blue dashed line) in Fig. 3.9. For region 2, 3, and 4 from the SCC facets, the lift-out sites are 3 mm away from the final SCC crack arresting (the red dashed line). By considering the crack propagation velocity and stress intensity factor in Fig. 4.9 and Fig. 4.10, 3 mm away from the SCC crack arresting front is in stage II SCC crack propagation for both wrought and HIPped Ti-811 samples.

For all lamellae, a Pt deposition about 2.5 μm was left on the fracture surface to reduce the ion beam damage. A sequentially reduced FIB energy was applied from thinning to polish stages, and the final polish was conducted at 2kV and 27pA to remove a layer of material with a depth at 40 nm.

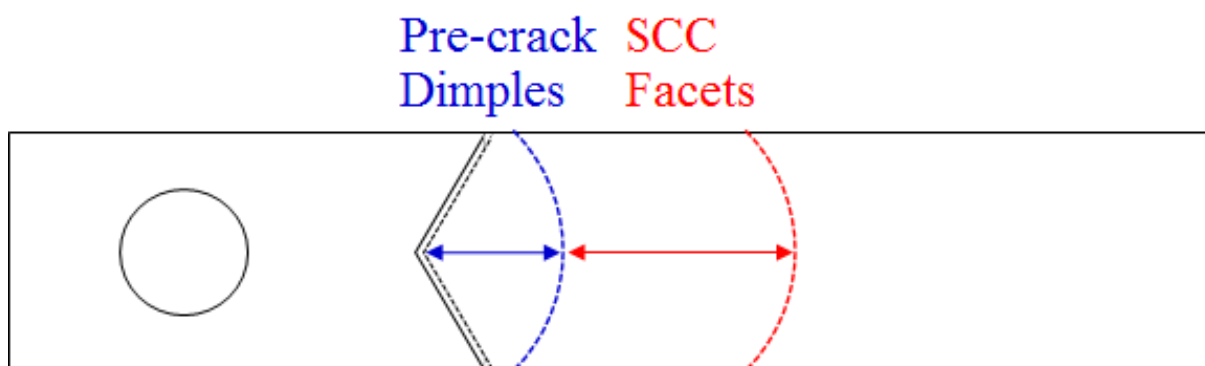


Fig. 3.9. Illustration of fractured SCC samples in the top view of the DCB sample in Fig. 3.7.

A correlation between operating slip systems and the critical tensile stress was studied in the regions of interest based on Schmid's law. Crystallographic orientations and Schmid factor calculations of all FIB foils were studied by using "Transmission"-EBSD (T-EBSD) in a FEI Quanta 3D FEG microscope at 25 keV (accelerating voltage) and 23 nA (electron current), and post data analysis were conducted by AZtecHKL and OIMTM software packages. In order to determine active slip systems, dislocation contrast experiments were based on a scalar product $g \cdot b$ invisibility criterion by using a 200 keV FEI Tecnai G2 T20 TWIN TEM. Dislocation

invisibility under two beam condition is generally controlled by the $g \cdot b = 0$, where g is the reciprocal lattice vector of the activated reflection and b is the Burgers vector of dislocations [110-112]. Therefore, the burgers vector (b) of dislocations can be determined by using different g vector.

As the nature of dislocation and dislocation density will be discussed in this work, one may suspect that they could be affected by the ion beam damage during the FIB lift-out sample preparation stage. Previous studies [113-115] reported defects, including dislocation, related to high energy Ga^+ ion damage in FIB lift-out foils. However, a recent study on a near α Titanium alloy showed that a FIB lamella with a sequentially reduced ion energy thinning and final polishing voltage and current at 2 kV and 28 pA did not affect the dislocation contrast analysis compared to an electropolished foil [116]. In the current study, a sequentially reduced ion energy milling and a final polishing process at low energy beam of 2 kV and 27 pA was used. Therefore, it is not expected to affect the dislocation analysis.

CHAPTER IV: STRESS-CORROSION CRACKING: EFFECT OF VARIABLES

The literature review described the influence of Ti_3Al (α_2) precipitates and texture on SCC properties in Ti-8Al-1Mo-1V. As mentioned in the research aims, the previous studies were investigated in textured materials. In this chapter, HIPped Ti-8Al-1Mo-1V without texture was used to elucidate more clearly the effect of α_2 precipitates. In previous research, microtexture or ‘macrozones’, region of grains with a similar crystallographic orientation, have been found to affect the fatigue and dwell fatigue properties in titanium alloys [19, 41, 45-48]. To the authors’ knowledge, there has been no investigation into the effects of microtexture on SCC. Therefore, the effect of microtexture on SCC in Ti-8Al-1Mo-1V is another aim of this chapter.

This chapter presents microstructure characterizations and SCC test results of the wrought Ti-811, wrought Ti-811 + HT860, HIPped Ti-811, and HIPped Ti-811 + HT860 samples (See Tab. 3.1). The effect of α_2 precipitates and microtexture was investigated by a constant displacement SCC test on double cantilever beam (DCB) samples. Key results including microstructure, microtexture, and determination of α_2 precipitation were obtained by using SEM, EBSD and TEM selective area diffraction (SAD) pattern techniques. Mechanical properties were provided by tensile tests for all the conditions.

4.1 Experimental Results

As described in the experimental methods (Chapter III), various Ti-8Al-1Mo-1V specimens were prepared by different material processing techniques and heat treatments. These would have different microstructural features and texture. This section shows the result of microstructure and microtexture of a series of Ti-8Al-1Mo-1V samples. Mechanical and SCC properties are also presented.

4.1.1 Microstructure and Texture

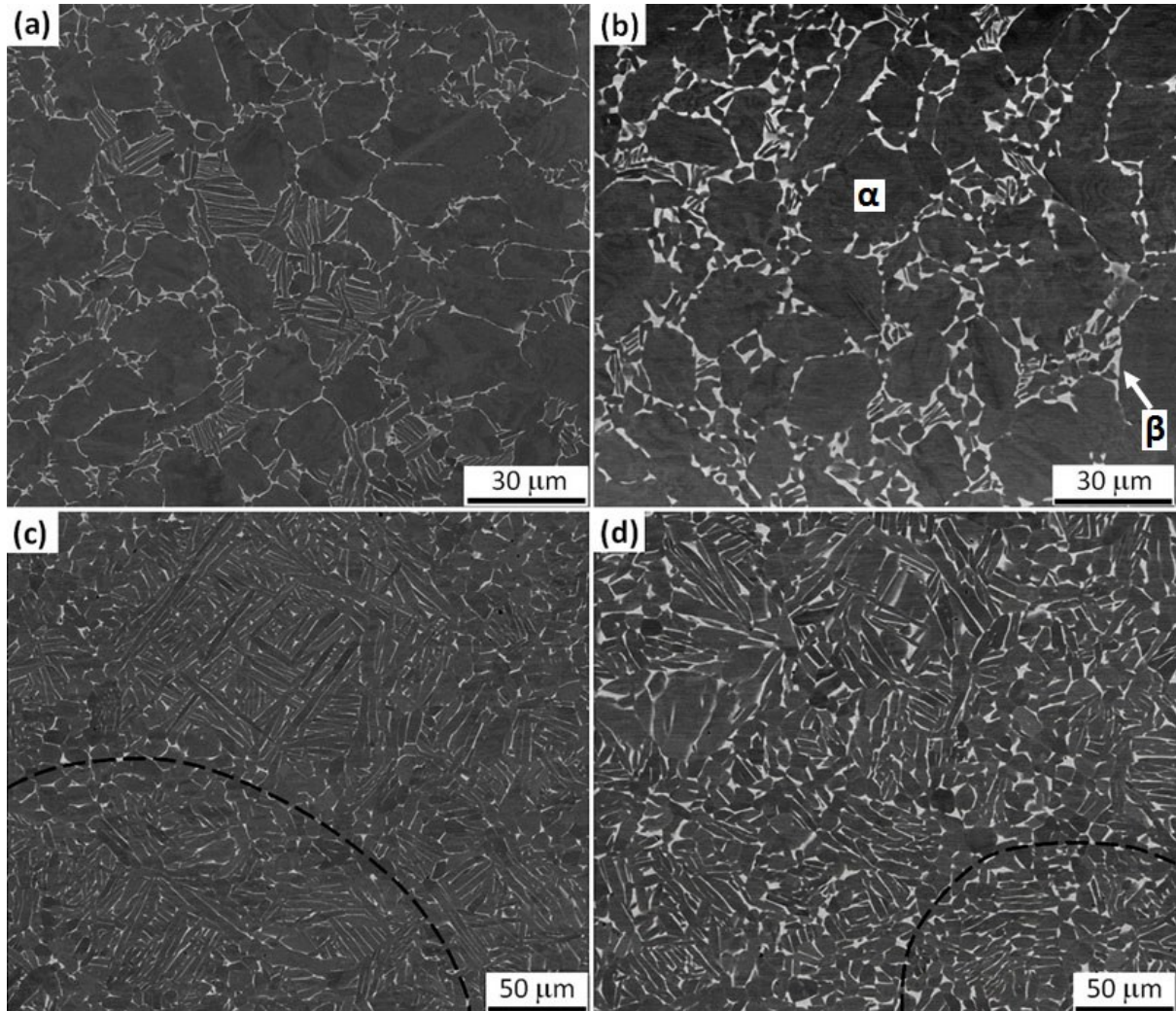


Fig. 4.1 Backscattering electron (BSE) images showing the microstructure of (a) wrought Ti-811, (b) wrought Ti-811 + HT860, (c) HIPped Ti-811, and (d) HIPped Ti-811 + HT860. Prior particle boundaries are denoted by black dashed lines in (c) and (d). In all images, dark area is α phase and bright area indicates β phase.

Microstructures of wrought and HIPped Ti-8Al-1Mo-1V should be different due to the different process techniques, therefore SEM was used to characterize the microstructures of different samples. Fig. 4.1 shows the microstructures of wrought Ti-811, wrought Ti-811 + HT860, HIPped Ti-811, and HIPped Ti-811 + HT860. The sizes of globular α grains and transformed β grains were in the range from 20 to 30 μm for wrought Ti-811 sample (Fig. 4.1a). HIPped Ti-811 consisted of recrystallized equiaxed α grains (along the black dashed lines) with a size range from 5 to 10 μm , and α laths with a thickness of 2 μm (Fig. 4.1c). After a 30 mins post heat treatment at 860 °C followed by water quench (WQ), both the wrought Ti-811 +

HT860 (Fig. 4.1b) and HIPped Ti-811 + HT860 (Fig. 4.1d) samples showed slightly larger grains and thicker lamellae than the materials before the heat treatment. There was approximately 10 vol.% β phase in wrought Ti-811 and HIPped Ti-811 samples, and approximately 11.7 vol.% β after the heat-treatment at 860 °C followed by WQ. During the HIPping process, preferential recrystallization occurred at prior particle boundaries due to the highly localized deformation, and examples are illustrated by equiaxed grains denoted by red dashed lines in Fig. 4.1c and d. The microstructure of the HIPped material shows that it is a fully dense material without porosity.

Based on the Ti-Al binary phase diagram (Fig. 1.2), α_2 phase can form in Ti-811 alloy when the Al content is high. As the ordering transformation temperature is about 837 °C (Fig. 3.3), a post heat treatment at 860 °C for 30 minute followed by water quench was designed to suppress the α_2 precipitation. Ordering alters the lattice parameter, which is double that in α phase on the basal plane, but it remains the same in the *c*-axis. TEM analysis was employed to investigate the α_2 precipitation. TEM images of wrought Ti-811, HIPped Ti-811, and HIPped Ti-811 + HT860 samples are respectively shown in Fig. 4.2a, b and c. Interestingly, superlattice spots in the SAD patterns indicated that ordered α_2 precipitates existed in the wrought and HIPped Ti-811 samples. The corresponding dark field (DF) TEM images were also taken from the superlattice reflection, and bright particles are α_2 precipitates in Fig. 4.2a and b. The distribution of α_2 precipitates are homogeneous in α matrix for both wrought and HIPped Ti-811 samples. The size of precipitates was less than 5 nm, but the wrought Ti-811 sample had slightly larger precipitates than those in the HIPped Ti-811 sample. In contrast, the SAD pattern in Fig. 4.2c did not show the existence of α_2 precipitates, which verifies that α_2 precipitation was suppressed after the designed post heat treatment.

As the superlattice reflections were faint in the SAD pattern taken from HIPped Ti-811, High Resolution TEM (HRTEM) was further employed to investigate the α_2 precipitation. Fig. 4.3a

illustrates a high resolution atomic image in HIPped Ti-811. Fig. 4.3b is an enlarged view from the region b in Fig. 4.3a, which shows that basal planes are aligned horizontally. Fig. 4.3c and d are fast Fourier transforms (FFT) taken from regions c and d. An α_2 spot is marked by the red circle in Fig. 4.3d, which implies ordered D₀₁₉ clusters presented in region d. While according to the FFT in Fig. 4.3c, region c is normal α titanium matrix. Therefore, the HRTEM image and FFT further prove that α_2 precipitates exist in the powder HIPped Ti-811 sample.

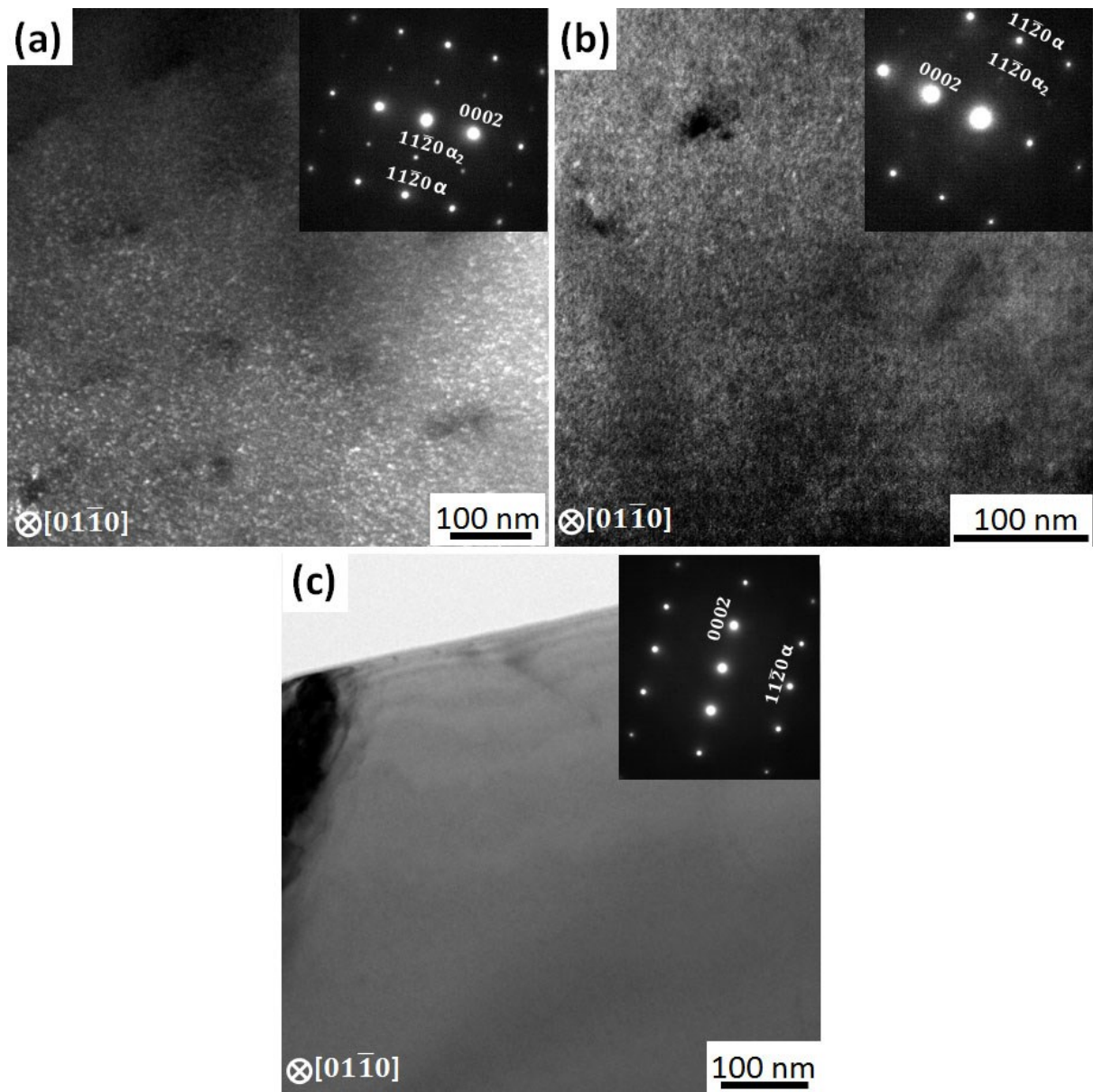


Fig. 4.2 (a) Dark field (DF) TEM image of wrought Ti-811 bar, (b) DF TEM image of HIPped Ti-811, (c) Bright field TEM image of HIPped Ti-811 + HT860 – suppressing α_2 ordering transformation; beam parallel to $[01\bar{1}0]_\alpha$.

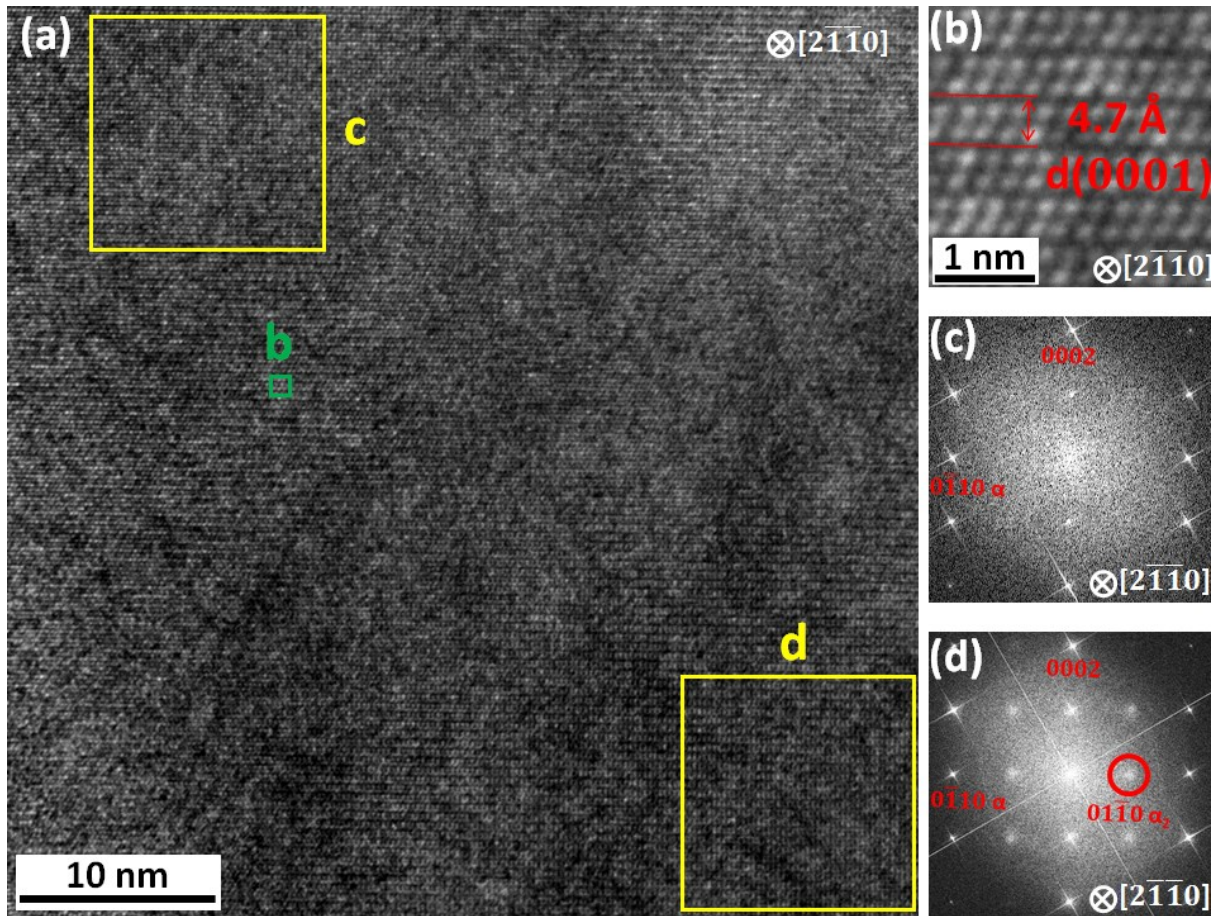


Fig. 4.3 (a) High resolution TEM (HR-TEM) image of ordered and disordered regions in HIPped Ti-811 sample, (b) HR-TEM image from box b, (c) and (d) $[2\bar{1}\bar{1}0]$ fast Fourier transforms (FFT) pseudo-diffraction patterns processed from boxes c and d, and (d) HRTEM image from box d, beam parallel to $[2\bar{1}\bar{1}0]$.

As the microstructures of wrought and HIPped Ti-8Al-1Mo-1V (Fig. 4.1) are different due to the different process techniques, it is necessary to study the difference in texture by EBSD. The volume fraction of β phase was low (about 10% to 12% for all samples in Fig. 4.1), therefore pole figures and orientation maps were only computed for α phase. Inverse pole figure (IPF) microstructure maps and their associated pole figures of wrought Ti-811 bar are presented in Fig. 4.4. On the cross section surface 1 (Fig. 4.4c), the overall peak intensity of 1.66 indicates the global texture was not strong. However, the IPF microstructure map shows microtextured regions of clusters of grains with a similar orientation (examples are indicated by black arrowheads in Fig. 4.4a). On circumferential surface 2 (Fig. 4.4b), there is a heterogeneous orientation distribution of α grains. Bands of grains with a similar crystallographic orientation (microtextured regions) are aligned in the L (axial) direction, and the peak intensity is 10.23

suggesting a strong microtexture (Fig. 4.4d). The two (0001) pole components in Fig. 4.4d are the main crystallographic orientations corresponding to the top and bottom microtextured regions in Fig. 4.4b. Based on the two associated pole figures in Fig. 4.4c and d, there are six main (0001) poles, which are 60 degrees to each other, with the c-axis approximately aligned in R (radial) directions.

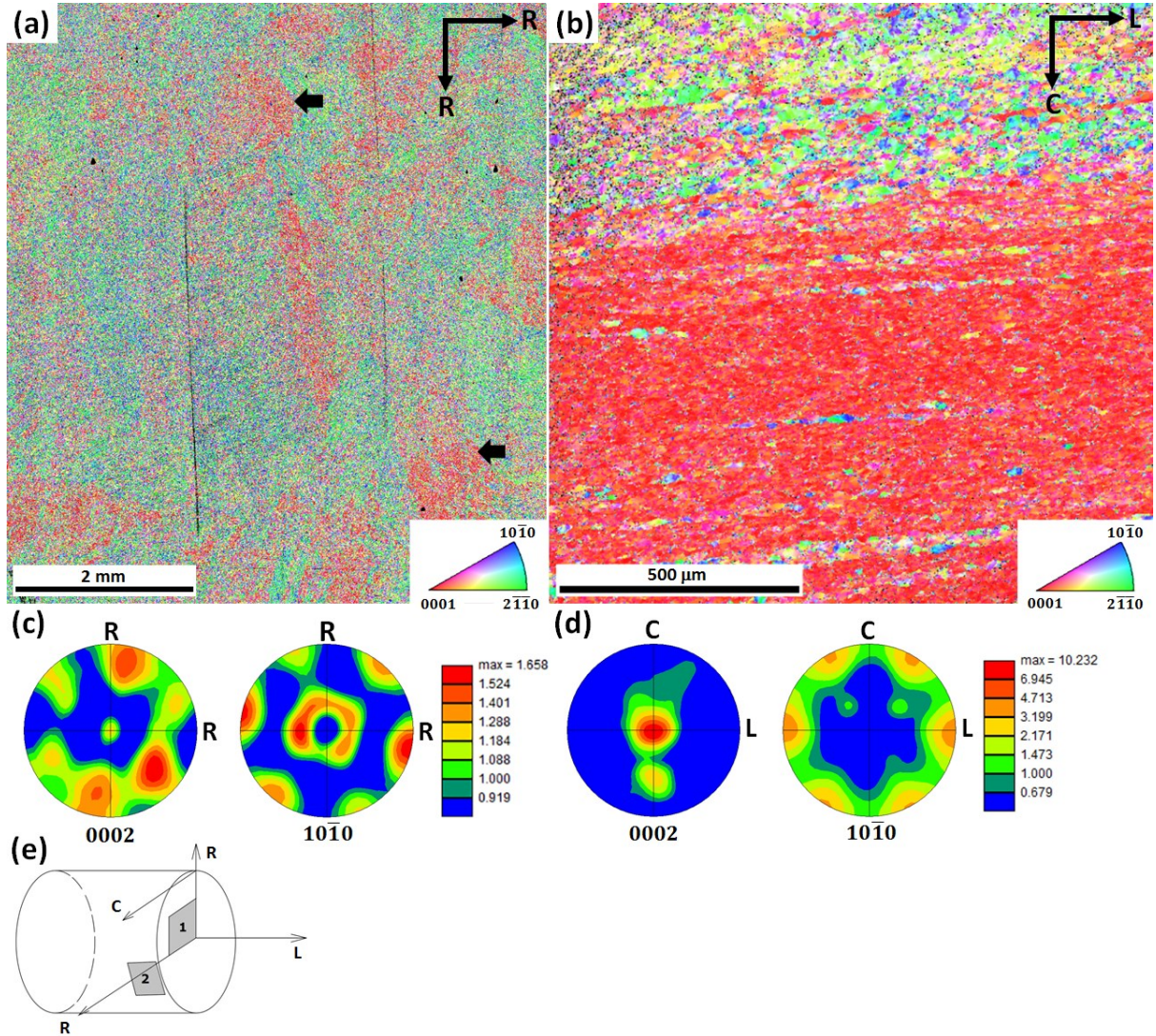


Fig. 4.4 The Inverse Pole Figure (IPF) maps and associated pole figures of α -Ti phase for as-received Ti-811 bar: (a) and (c) transverse to longitudinal direction – surface 1, (b) and (d) circumferential surface parallel to longitudinal direction – surface 2. Schematic illustration of surfaces 1 and 2 in Ti-811 bar is depicted in (e). R: radial direction, C: circumferential direction, and L: longitudinal direction.

In $\alpha+\beta$ Ti alloys, texture type and intensity are mainly correlated with deformation type and degree [8]. The heat treatment at 860 °C followed by WQ is not expected to change the texture

in wrought Ti-811. Therefore, crystallographic texture of wrought Ti-811 + HT860 is likely to be similar to that of wrought Ti-811.

Fig. 4.5a and c illustrate the orientation maps and associated pole figures of HIPped Ti-811 at 990 °C. Fig. 4.5c shows that the peak intensity of (0001) pole was 2.32, and it might be regarded as a slightly textured material. However, there were not any microtextured regions in the HIPped sample unlike in the wrought Ti-811 sample. All equiaxed α grains and laths were randomly orientated, and they do not share a similar crystallographic orientation to their neighbouring α grains. After a 30 mins post heat treatment at 860 °C (Fig. 4.5b and d), the peak intensity of (0001) was 1.72, and there was no trace of microtexture. Therefore, both HIPped Ti-811 and HIPped Ti-811 + HT860 samples are regarded as microtexture-free conditions.

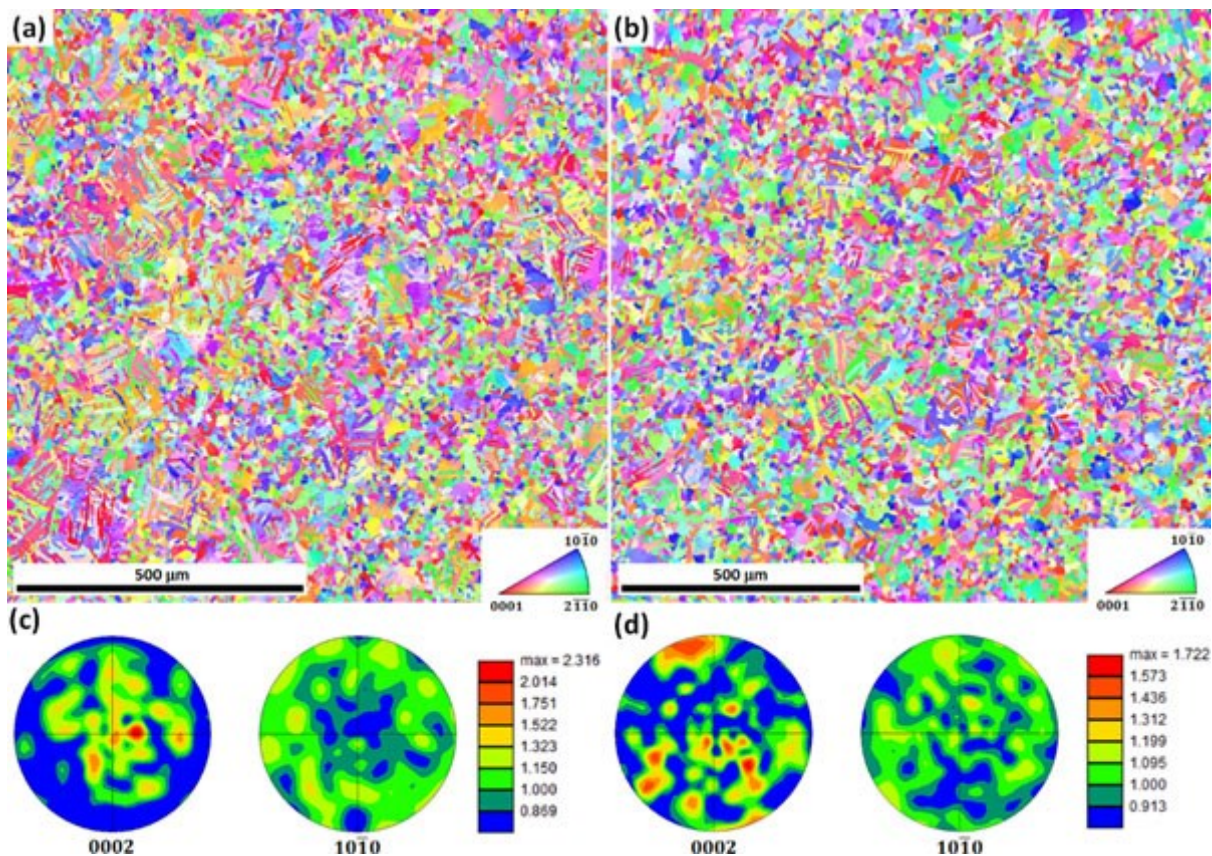


Fig. 4.5. IPF images and associated pole figures of α -Ti phase, (a) and (c) HIPped Ti-811, (b) and (d) HIPped Ti-811 + HT860.

4.1.2 Mechanical Properties

Previous sections describe that the microstructure and microtexture are different in different samples. It is expected that the mechanical properties will be different. Tensile tests were conducted on the wrought Ti-811, wrought Ti-811 + HT860, HIPped Ti-811, and HIPped Ti-811 + HT860 at room temperature with the test crosshead speed at 1 mm/min. For each condition, three tensile samples were tested to ensure the reproducibility. The true stress-strain curves for all samples are illustrated in Fig. 4.6. As illustrated, true stress-strain curves overlap closely for each condition, which means that the results are reproducible. The wrought Ti-811 (red curves) has the highest yield strength, while HIPped Ti-811 (blue curves) has the best ductility.

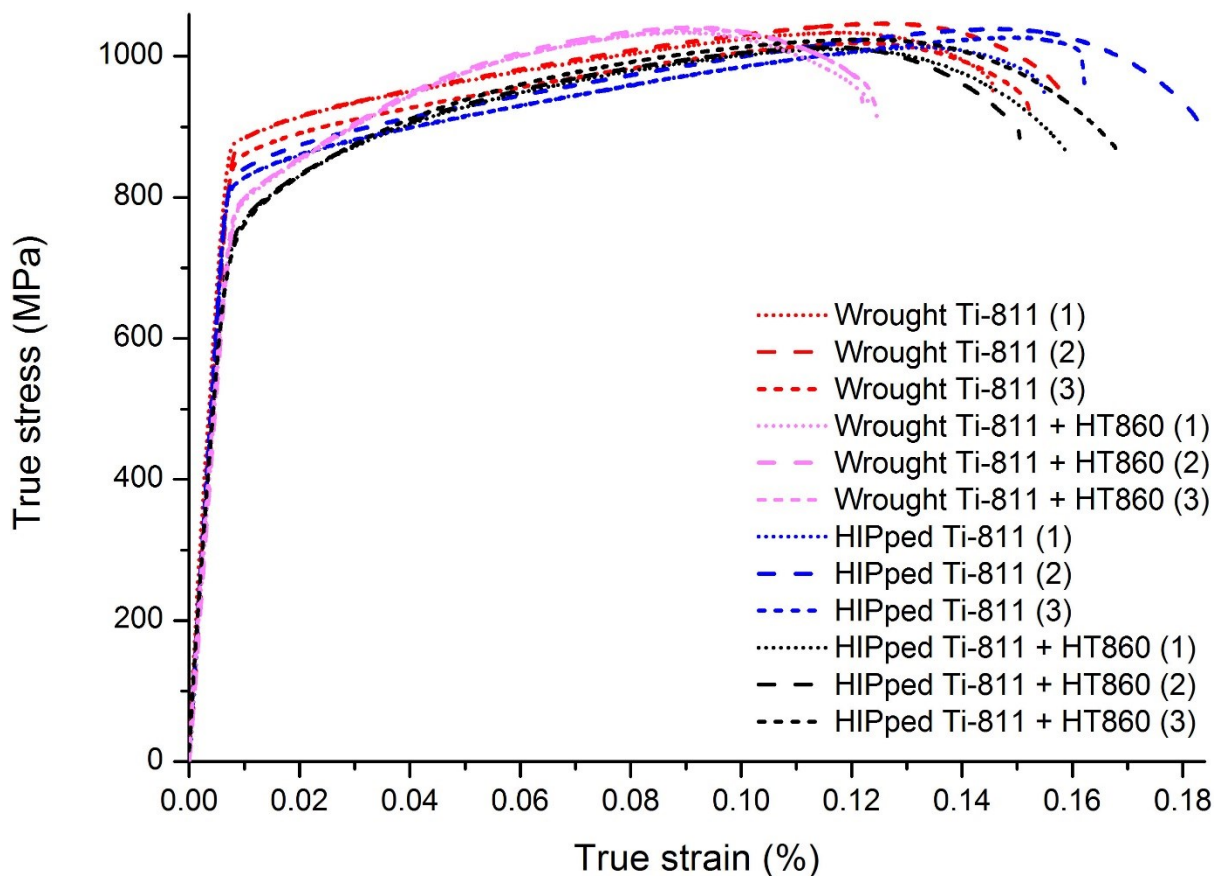


Fig. 4.6. True stress-strain curves of the wrought Ti-811 (red), wrought Ti-811 + HT860 (pink), HIPped Ti-811 (blue), and HIPped Ti-811 + HT860 (black). Three repeat tests were carried out for all samples.

The mechanical properties for all four samples are summarized in Tab. 4.1. The table shows that the as-HIPped condition (HIPped Ti-811) had comparable mechanical properties to those of wrought Ti-811 product. The heat treated samples (wrought Ti-811 + HT860 and HIPped Ti-811 + HT 860), which did not have ordered and coherent α_2 precipitates, had a 10% reduction in both Young's Modulus and yield strength than those of as-received wrought bar and as-HIPped conditions. However, the ductility (El.) was observed to be slightly lower after the post heat treatment, which seemed to be counter to the effects of larger grain sizes with the absence of precipitation hardening. The reduction in ductility may be related to the residual stress associated with the water quench during the post heat treatment.

Tab. 4.1 Summary of tensile properties for various Ti-8Al-1Mo-1V samples.

Samples	E (GPa)	0.2% YS (MPa)	El. (%)
Wrought Ti-811	120.7 ± 1.3	869.9 ± 14.3	15.2 ± 0.6
Wrought Ti-811 + HT860	106.3 ± 2.0	783.7 ± 1.9	12.3 ± 0.1
HIPped Ti-811	122.7 ± 1.8	817.5 ± 7.8	16.7 ± 1.4
HIPped Ti-811 + HT860	110.7 ± 4.5	741.0 ± 3.8	15.9 ± 0.8

Notes: E , 0.2% YS, and El. are abbreviations of Young's Modulus, yield strength, and elongation respectively. Three replicates were tested for all sample conditions, and standard deviations are shown in the above table.

Fig. 4.7 illustrates the tensile fracture surfaces of various Ti-8Al-1Mo-1V samples tested at room temperature. Although there are some differences in the orientation of ductile dimples, the main feature remained as ductile dimples in all the specimens. It is clear that all the fracture processes were ductile, which is consistent with good ductility (large elongation) in the true stress-strain curves of all samples (Fig. 4.6).

As the fracture surface characteristics are related to the local microstructure and grain orientations, the SEM images only represents the response of local microstructure to the tensile deformation in Fig. 4.7. The fracture surface of wrought Ti-811 (Fig. 4.7a) contains dimples of different sizes, which are formed in grains with different orientations. On the fracture surface

of the post heat treated wrought Ti-811 (wrought Ti-811 + HT860 in Fig. 4.7c), the dimples are mainly aligned and have a similar orientation. While dimples are formed in different orientations at various heights in the powder HIPped sample (HIPped Ti-811 in Fig. 4.7e). In the post heat treated HIPped Ti-811 (HIPped Ti-811 + HT860 in Fig. 4.7g), the dimples have two main orientations. The dimples at the top are arranged in the direction of shear fracture, however the bottom features are mainly tear dimples.

As illustrated in the low magnification images (Fig. 4.7), there are dimples located in the shear and tear zones. Close-up images of these two distinct zones are observed as Fig. 4.8a and b, the shallow elongated dimples and deep equiaxed dimples are corresponding to the shear and tear regions respectively. It shows that elongated dimples are arranged in the shear direction, and failure is dominated by the shear process along grain boundaries in Fig. 4.8a. The formations of shear and tear dimples mainly depend on the grain orientations and loading conditions [117].

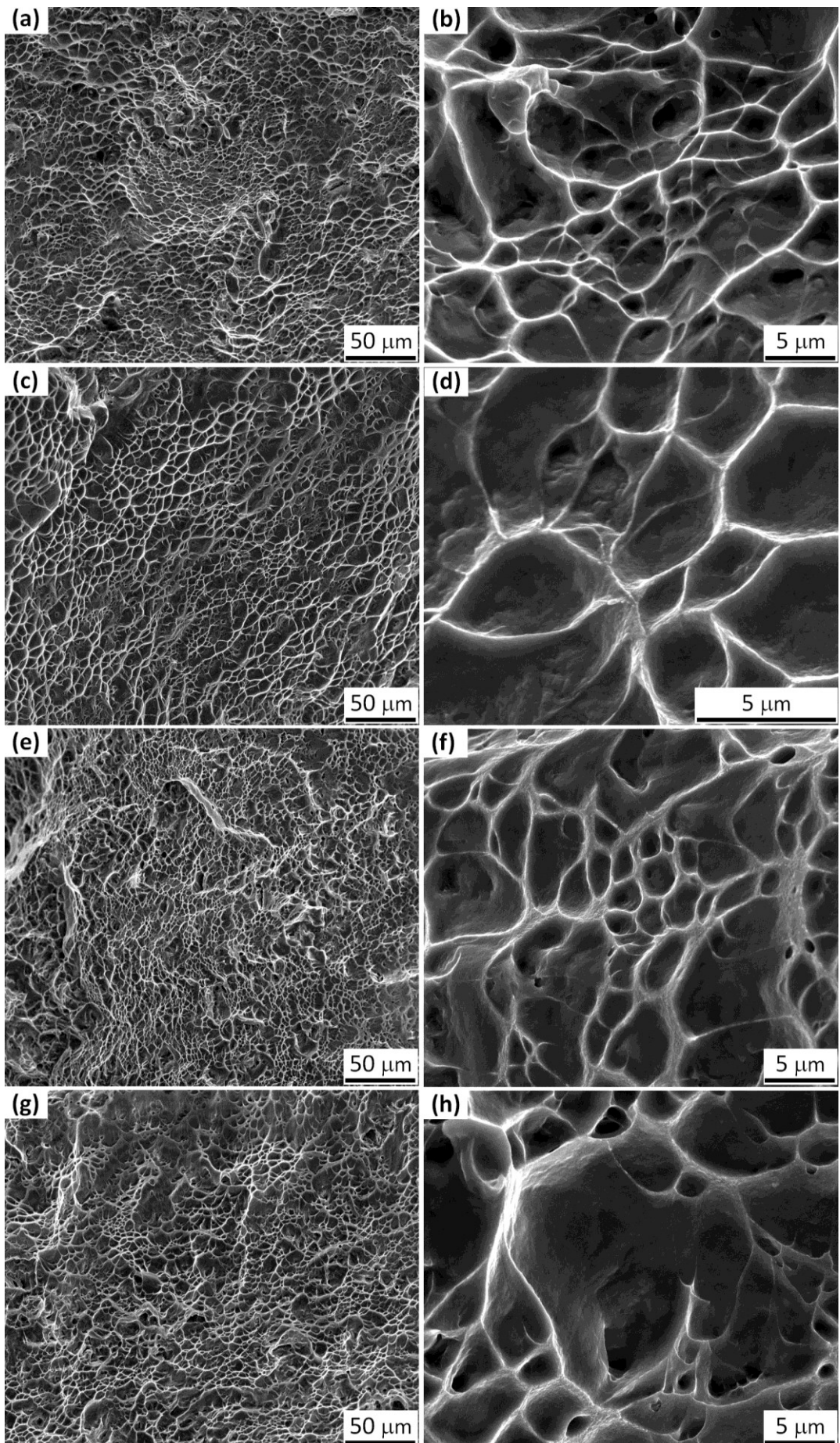


Fig. 4.7. SEM secondary electron images of fracture surface of tensile test specimens at low and high magnifications: (a) and (b) wrought Ti-811, (c) and (d) wrought Ti-811 + HT860, (e) and (f) HIPped Ti-811, (g) and (h) HIPped Ti-811 + HT860. Ductile dimples are main characteristics on the fracture surface in all cases.

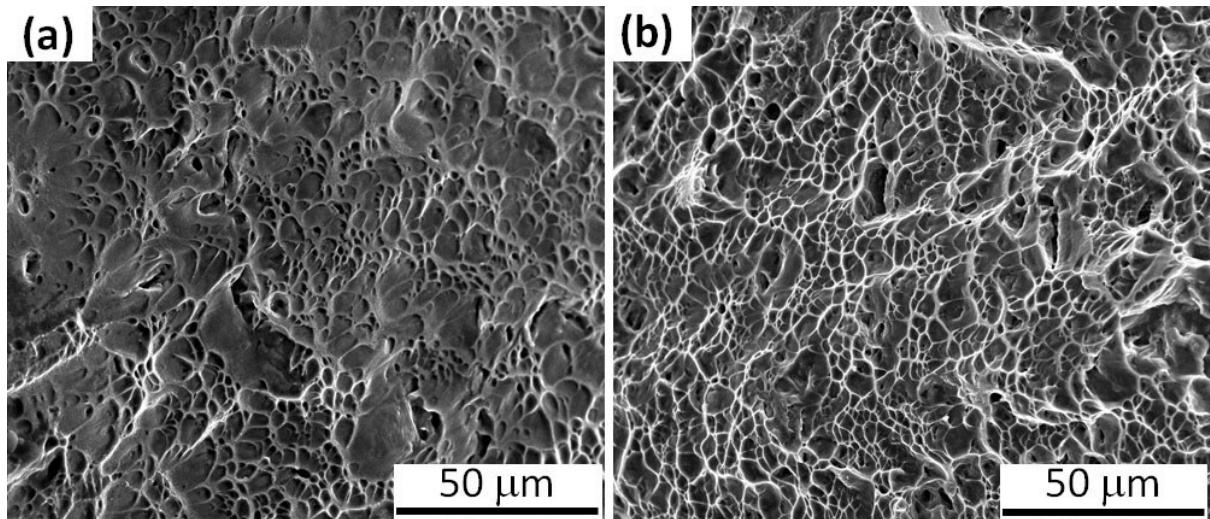


Fig. 4.8. SEM secondary electron images of fracture dimples of tensile test specimen of HIPped Ti-811 sample: (a) shear zone, (b) tear zone.

4.1.3 Stress-corrosion Cracking Properties

A major research objective is to investigate the effect of ordered α_2 precipitates and microtexture on SCC susceptibility of Ti-8Al-1Mo-1V. The results describe the influence of these two factors in this section.

A constant displacement SCC test on double cantilever beam (DCB) specimens was conducted in 0.1 M aqueous NaCl solution (pH at 5.7) by applying two stainless steel bolts against each other for all the sample conditions in Tab. 3.1. The solution was open to air and no potential was applied to the specimens. As presented in the Equation 3.1, the stress intensity factor (K) has an inverse relationship with the interim crack length. Therefore, the K value was decreasing during the SCC crack propagation.

Fig. 4.9 illustrates the interim SCC crack length as a function of testing time for various Ti-811 samples in 0.1 M NaCl solution. Generally, it shows the SCC crack velocities (slope) are lower in HIPped Ti-811 than those of wrought Ti-811. The interim SCC crack length was measured from the end of pre-crack, which was introduced by manual loading during the SCC test. Loading condition was slightly different in various samples, which leaded to a series of pre-crack lengths in them. As the inverse interrelationship between the stress intensity factor and

crack length described in Equation 3.1, the stress intensity factor (K_{10}) at SCC starting point was also expected to be different. However, stress intensity factor has an influence on the crack propagation velocity and overall crack length. Therefore in Fig. 4.9, crack propagation length vs. time curves are distinct even for the same sample condition. Raw data of Fig. 4.9 was used to calculate the SCC crack velocity and corresponding stress (related to the interim crack length) intensity factor for Fig. 4.10.

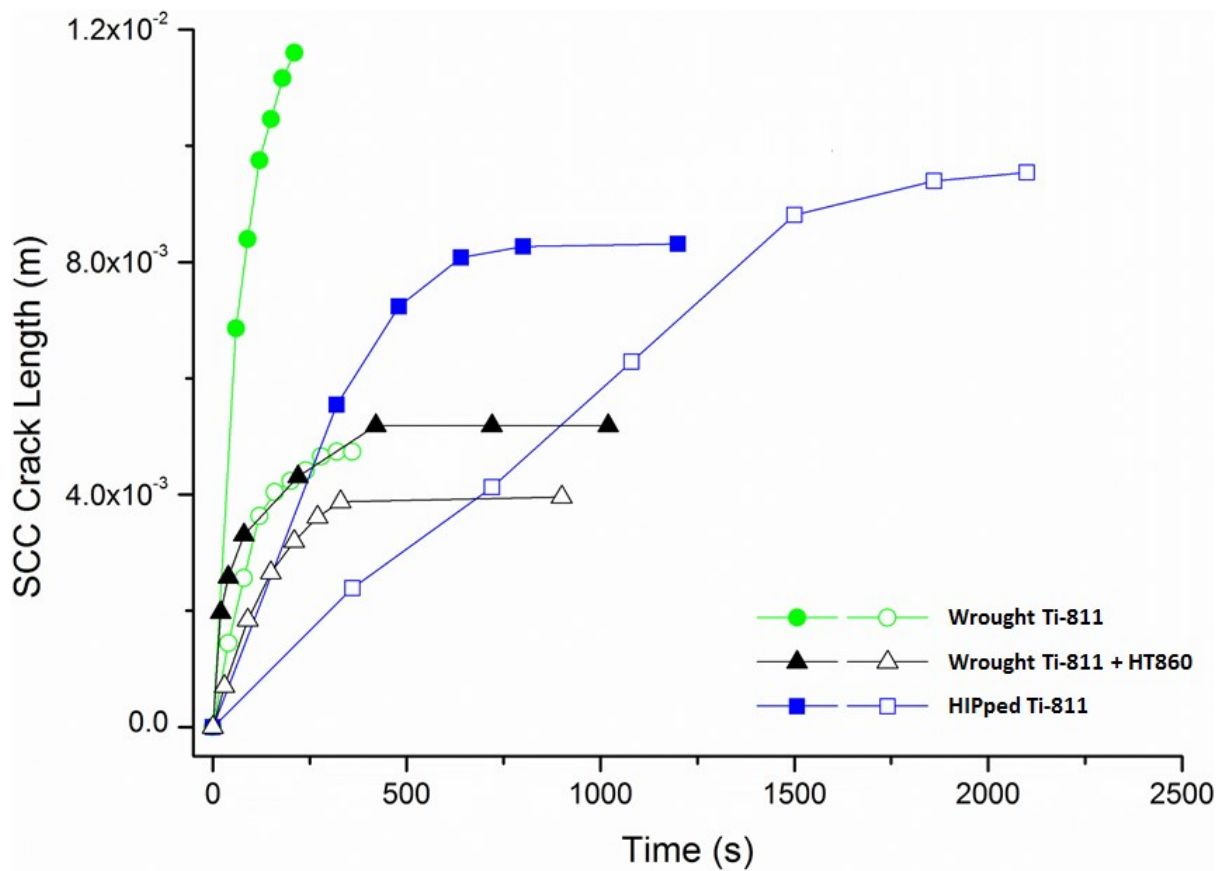


Fig. 4.9. The interim SCC crack length versus time for various Ti-811 conditions in 0.1 M aqueous NaCl solution. Two repeated tests (the solid and hollow data points) for each conditions.

The crack growth rates associated with stress intensity levels at particular crack lengths for all four conditions are plotted in Fig. 4.10. Polynomial curve fittings were applied to the SCC data for the various sample conditions. These are presented by solid lines. In addition, confidence bands (95% confidence level) were presented by the dashed line. Most of the data points are located within the confidence bands. Based on the curve fitting functions, values of K_{ISCC} were computed corresponding to SCC crack velocity at 10^{-10} m/s. These are summarized for

the various sample conditions in Table 4. The HIPped Ti-811 shows a typical Region I/Region II SCC behaviour. Samples without α_2 precipitates (wrought Ti-811 + HT860) had a slightly higher K_{ISCC} and slower propagation velocity than those of wrought Ti-811. The data also shows that microtexture-free HIPped Ti-811 condition had an order of magnitude lower SCC crack velocity and 2.4 times higher K_{ISCC} than for the wrought Ti-811 condition. For HIPped Ti-811 + HT860 samples, no SCC crack propagation was detected even at stress intensity factors of approximately 156 MPa $\cdot\sqrt{m}$.

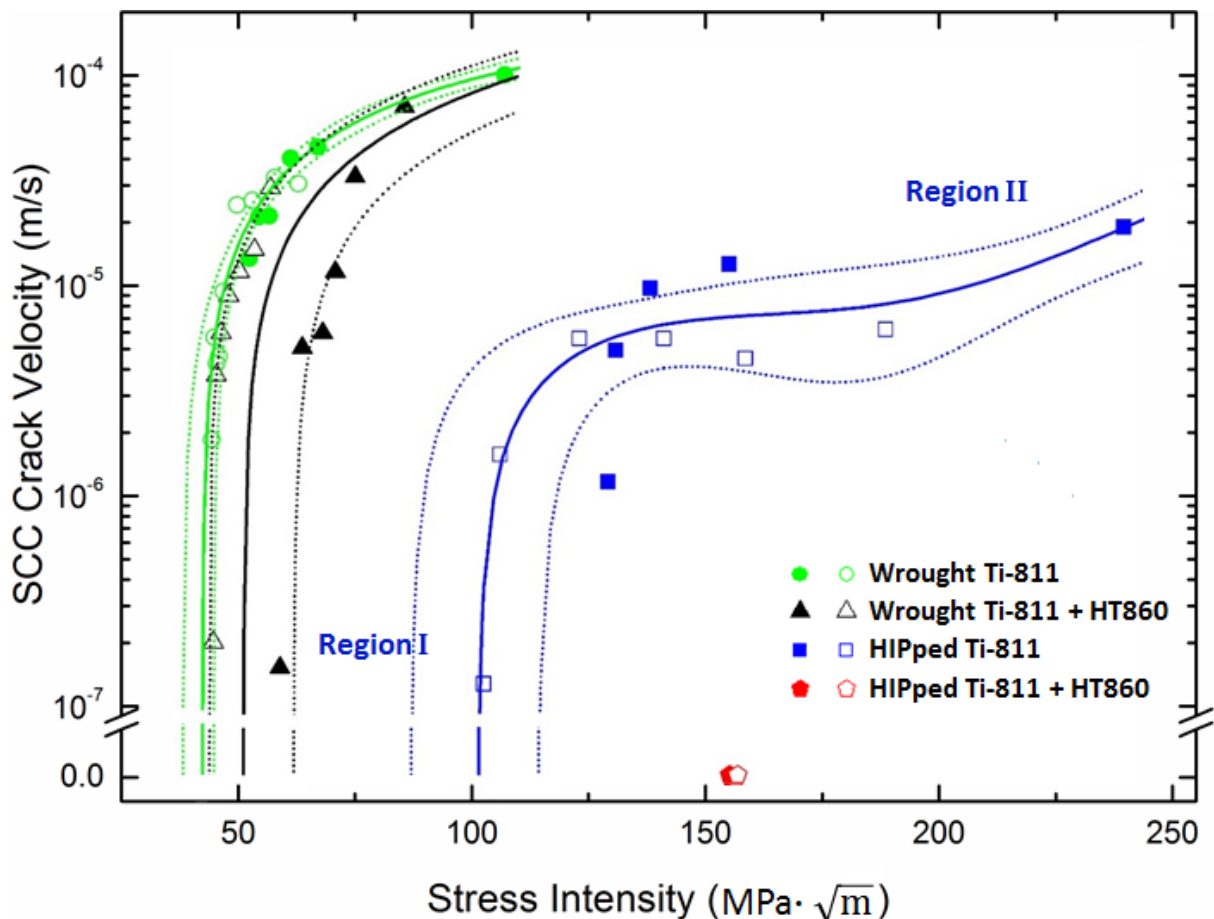


Fig. 4.10. Crack propagation velocities as a function of stress intensity factors for various Ti-811 conditions in 0.1 M aqueous NaCl solution. Two repeated tests (the solid and hollow data points) were conducted for each condition. Solid lines are polynomial fitted curves for SCC data points of different sample conditions, corresponding dashed lines indicate a band of 95% confidence level (For all solid and dashed lines, blue - HIPped Ti-811, black - Wrought Ti-811 + HT 860, green - wrought Ti-811).

Tab. 4.2 Threshold stress intensity for various Ti-8Al-1Mo-1V samples.

Samples	K_{ISCC} (MPa· \sqrt{m})
Wrought Ti-811	42.4
Wrought Ti-811 + HT860	51.5
HIPped Ti-811	101.3

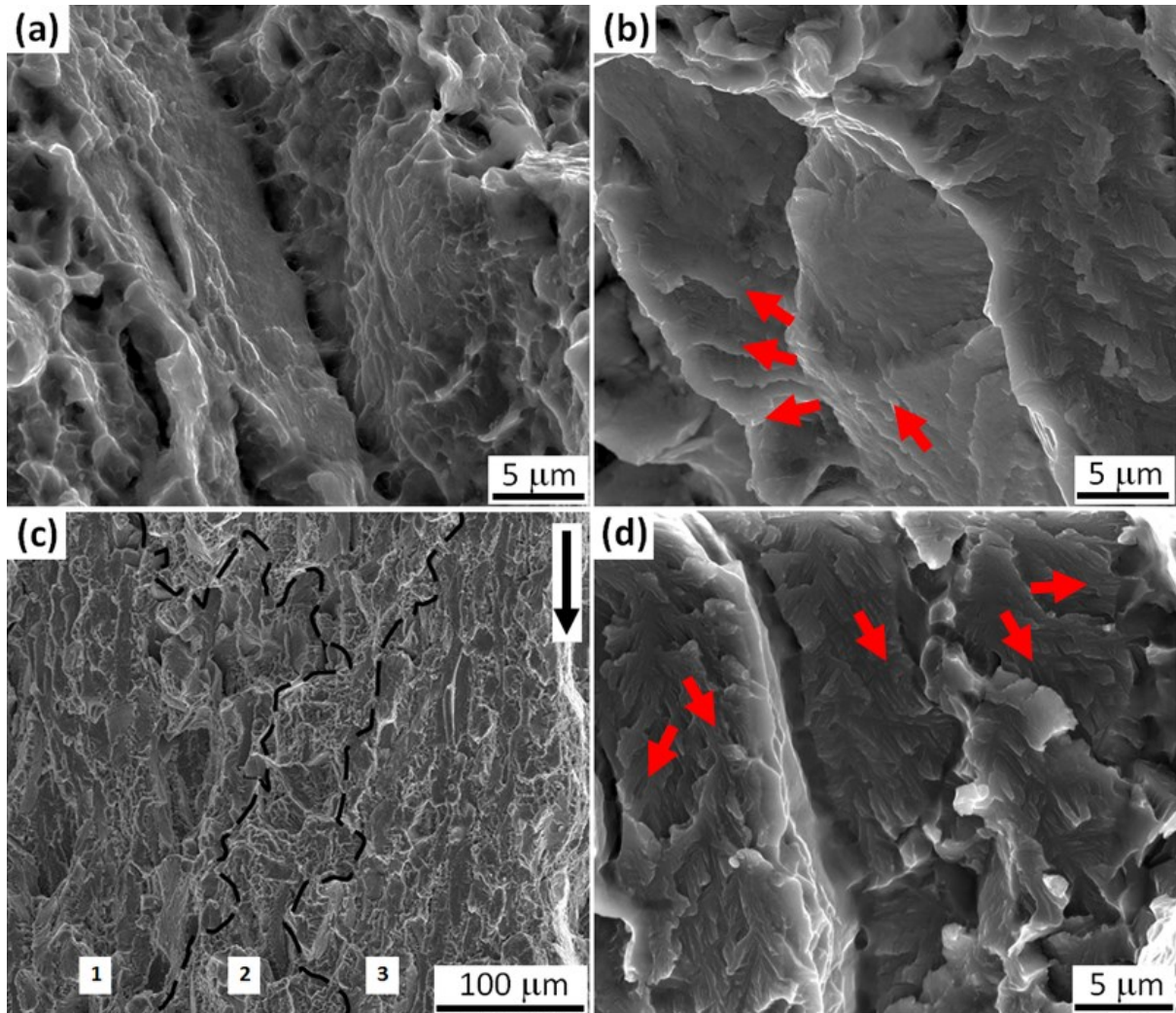


Fig. 4.11. Fractography on crack surface of wrought Ti-811 sample (a-c): (a) High magnification secondary electron (SE) image of dimpled fracture from the pre-crack in air, (b) high magnification SE image of SCC faceted fracture, (c) low magnification SE image of SCC fracture, and the overall propagation direction is shown by the black arrow; of wrought Ti-811 + HT860 sample, and (d) high magnification SE image of SCC fracture. All the red arrowheads indicate the local crack propagation direction on SCC propagation facets.

When SCC cracks stopped propagating, the specimens were broken open by tightening the bolts and increasing load. The fractography of wrought Ti-811 sample illustrated in Fig. 4.11a and 4.11b, reveals that ductile dimples, resulting from micro-void coalescence, were a

dominant feature in the precrack fracture in air, while flat transgranular facets appeared in SCC cracking region. An overview of the SCC fracture surface of wrought Ti-811 sample is showed at low magnification in Fig. 4.11c. There were regions of flat facets (regions 1 and 3) aligning along the propagation direction as indicated by the black arrow, which is also the longitudinal (L) direction in the Ti-811 bar. A region containing ductile dimples (region 2) is located between the two faceted regions. Fig. 4.11d is a high magnification image of SCC fracture surface for the wrought Ti-811 + HT860 sample, showing propagation facets with similar features to those seen on the wrought Ti-811 (Fig. 4.11b). Those similar features are terraces at various heights and tear ridges on the facets.

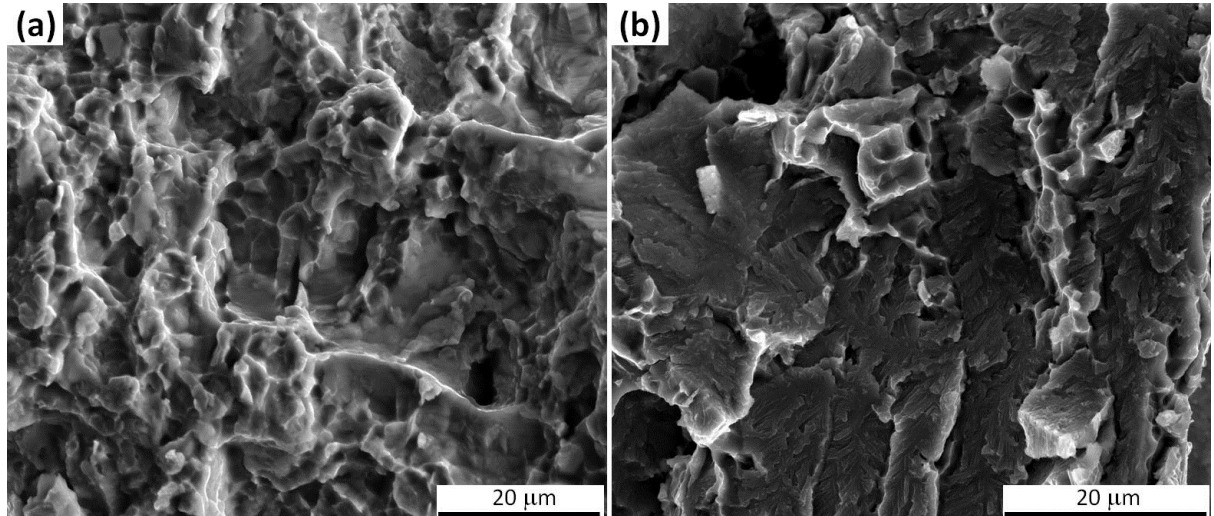


Fig. 4.12. SCC fractography of wrought Ti-811 + HT860 sample: (a) SE image of dimpled region fracture during the initial overload in air, (b) SE image of SCC faceted fracture surface failed in 0.1M NaCl aqueous solution.

Fig. 4.12a and b shows the fracture surface of a wrought Ti-811 + HT860 sample failed during the pre-loading in air and SCC in NaCl solution respectively. The fractography is like that of wrought Ti-811 sample (Fig. 4.11), it consists of pre-crack dimples and SCC facets.

Fig. 4.13a illustrates a ductile dimple fracture (I) to faceted fracture (II) transition at the beginning of SCC test (indicated by the black arrow) in HIPped Ti-811 sample. The transition border (black dashed line), was at the half convex fracture front due to the stress concentration caused by the chevron notch in DCB specimens.

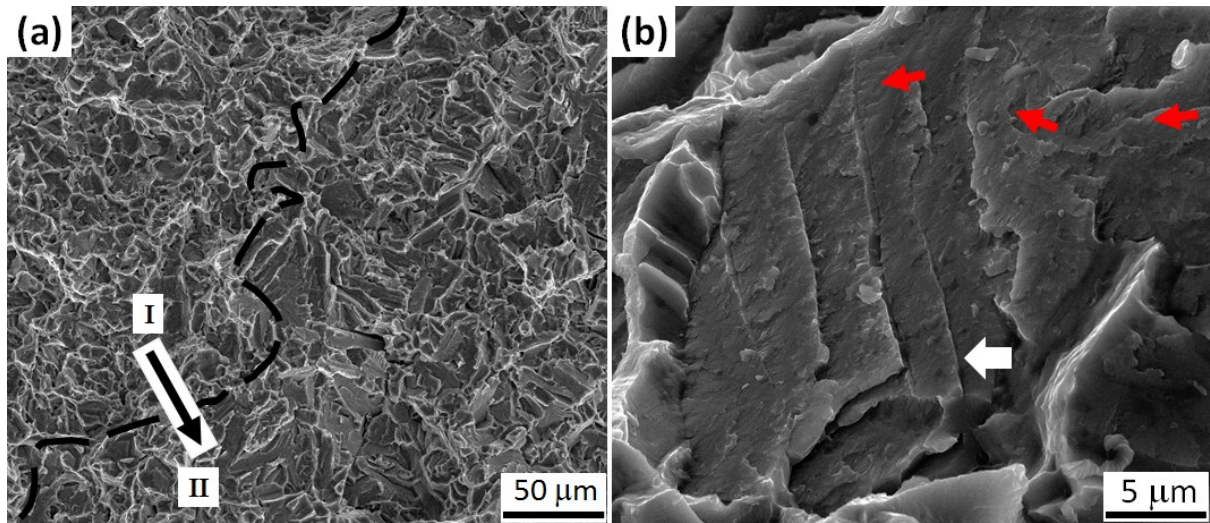


Fig. 4.13. Secondary images of crack surface for HIPped Ti-811 condition: (a) Ductile dimpled fracture to faceted failure transition at the beginning of SCC test in 0.1 M aqueous NaCl solution, and (b) high magnification image of a facet with slip bands formed steps, which are indicated by white arrowhead. All the red arrowheads indicate the local crack propagation direction on a SCC propagation facet.

For all high magnification secondary electron (SE) images of SCC propagation facets in Fig. 4.11b, Fig. 4.11d, Fig. 4.12b and Fig. 4.13b, tear ridges were observed and the local crack propagation directions were denoted by red arrowheads. These ridges were formed during plastic flow of α phase in SCC. They were also aligned with the local crack propagation direction [50, 75].

Previous research illustrated the slip bands on SCC facets of Ti-811 [13]. In the present study, planar slip bands with spacing of 2 μm were also present on facets as shown in Fig. 4.13b. The slip bands formed steps at different heights, indicating localized planar plastic deformation. Comparing the facets in wrought Ti-811 (Fig. 4.11c) and HIPped Ti-811 samples (Fig. 4.13a), the facets aligned in the propagation direction and formed in a similar fashion for wrought Ti-811, while the facets in the HIPped sample were more randomly orientated.

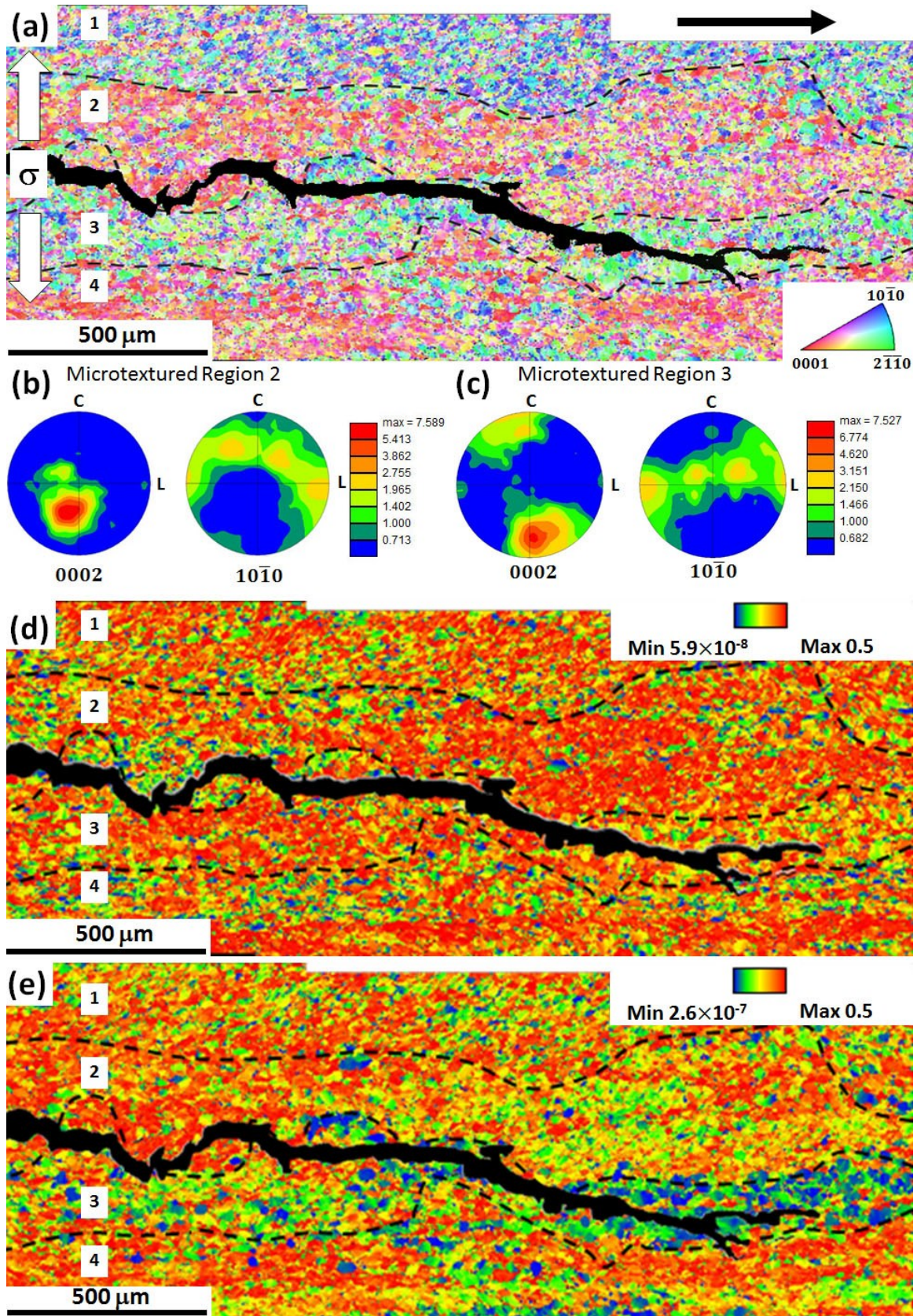


Fig. 4.14. (a) IPF map of α -Ti phase collected along the SCC crack path in a wrought Ti-811 sample, four microtextured regions are labeled as 1, 2, 3 and 4. In (a), the crack propagation direction is denoted by black arrow in the longitudinal direction (L) of the bar and loading direction is indicated by white arrows. (b) and (c) are associated pole figures for microtextured regions 2 and 3; Schmid factor distribution map for (d) basal $<\mathbf{a}>$, and (e) prismatic $<\mathbf{a}>$ slip systems of same area in (a). The four microtextured region are demarcated by black dashed lines.

Multiple orientation maps were recorded along the SCC crack in a wrought Ti-811 sample (Fig. 4.14a), and four elongated microtextured zones were observed with different crystallographic orientations. These zones were approximately 200 μm wide and more than 2 mm in length. The SCC crack mainly propagated in microtextured region 3 except for a small fraction in microtextured region 2. EBSD data were extracted for further texture analysis in regions 2 and 3, and the corresponding pole figures are given in Fig. 4.14b and c. Both regions were characterized by a strong basal texture around 7.55 with *c*-axis approximately oriented in R (radial) directions of wrought Ti-811 bar, which is similar to the microtexture shown in Fig. 4.4b.

As the Critical Resolved Shear Stress (CRSS) of the $\langle c + a \rangle$ slip systems is approximately 4 times as high as that of $\langle a \rangle$ slip in α -Ti [28], $\langle c + a \rangle$ slip will be favourably activated only when Schmid Factor (SF) of $\langle c + a \rangle$ slip is 4 times the SF of $\langle a \rangle$ slip. As shown in Fig. 4.14d and e, the highest SF of $\langle a \rangle$ slip is 0.5 in regions 2 and 3, which means that $\langle a \rangle$ slip is more readily activated than $\langle c + a \rangle$ slip. Therefore, the SF was only calculated for the basal $\langle a \rangle$ and prismatic $\langle a \rangle$ slip systems. Such a calculation showed that most grains had a much higher SF of basal $\langle a \rangle$ than that of prismatic $\langle a \rangle$ slip in microtextured region 3. In α -Ti, the CRSS ratio of prismatic $\langle a \rangle$ and basal $\langle a \rangle$ slips is approximately 0.9:1.0 [28]. Therefore, SCC crack propagated in the microtextured region 3 with most grains oriented favourably for basal $\langle a \rangle$ slip.

4.2 Discussions

The obtained results in section 4.1 illustrate that those Ti-8Al-1Mo-1V conditions have various responses to the aqueous NaCl SCC due to the difference in the microtexture and α_2 precipitates. This section mainly discusses the effect of the microtexture and α_2 precipitates on the SCC properties.

4.2.1 Effect of the Microtexture

In the present study, wrought Ti-811 and wrought Ti-811 + HT860 samples had the same DCB sample orientation when sectioned from the bar material, but the only difference was the presence of α_2 precipitates in wrought Ti-811, which is suppressed by the post heat treatment in wrought Ti-811 + HT860 (see Fig. 4.2). It is important to note here that there is a minor grain growth after the post heat treatment. As the crack propagation is related to the effective slip length of dislocations in titanium alloys [8], the increased grain size may influences the effective slip length. However, there are microtextured regions with a size scale of a few mm in these samples, and grains with similar crystallographic orientation will act like one grain in a microtextured region. It has been reported that the size of microtextured regions has a profound effect on the fatigue crack propagation [47]. Therefore, the effect of microtexture on crack propagation will be more significant than that of grain size.

Based on the IPF maps and associated pole figures in Fig. 4.4 and Fig. 4.5, the bar material (wrought Ti-811 and wrought Ti-811 + HT860) had a much stronger texture on both global or localized (microtexture) scale than the powder HIPped material. These microtextured zones with a size larger than 2 mm, were aligned along the longitudinal (L) direction of Ti-811 bar, which is also the crack propagation direction for wrought Ti-811 and wrought Ti-811 + HT860 samples. The aligned microtextured regions in the propagation direction may explain the alternative faceted region (region 1) /ductile region (region 2) /faceted region (region 3) on the fracture surface in Fig. 4.11c. Microtextured regions contained α grains with a similar orientation, and these grains behaved as a ‘single grain’ during SCC. As a result, the active slip length is much longer for a microtextured region compared to a single grain. The microtextured regions 1 and 3 might be favourably oriented for activation of certain slip systems, and then two micro-cracks are formed and aligned in the propagation direction.

Region 2 failed by ductile rupture due to the coalescence of the two micro-cracks afterwards. Such fracture features as appeared in Fig. 8c were not observed in the HIPped Ti-811 sample, in which the facets were randomly oriented due to the absence of microtexture.

As shown in Fig. 4.10, wrought Ti-811 and wrought Ti-811 + HT860 samples have an order of magnitude higher SCC crack velocity than HIPped Ti-811 samples. This is because α grains have similar crystallographic orientations inside a single microtextured region, and deformation behaviours are similar inside a microtextured region. Therefore, the effective slip distance is limited by the size of the microtextured region rather than α grain size in the wrought Ti-811 and wrought Ti-811 + HT860 samples. This is similar to the case of SCC immunity in martensite, in which slip cannot penetrates the boundaries of fine martensite [36]. The size of martensite plates in the previous work [36] is much smaller than the size of α grains and laths in this study, which means the effective slip length is even shorter in martensite.

The presence of microtexture results in a quick fracture in the form of aligned facets in a microtextured region. Multiple EBSD maps along SCC cracks in a wrought Ti-811 sample (Fig. 4.14) revealed the crystallographic orientation of α grains along the SCC crack path. It shows that the crack indeed propagates within a microtextured region orientated favourably for basal $<\alpha>$ slip. Therefore, the above discussion suggests that the presence of microtextured regions increased the effective slip length for dislocations, and subsequently accelerated the SCC crack velocity by one order of magnitude in wrought bar material (wrought Ti-811 and wrought Ti-811 + HT860).

K_{ISCC} in the HIPped sample is approximately 2.4 times that of wrought Ti-811. As K_{ISCC} is related to crack initiation susceptibility, which increases with effective slip length of dislocations. Thus on a whole, the HIPping process increases K_{ISCC} and reduces SCC crack velocity of Ti-811 considerably by the absence of microtexture.

4.2.2 Effect of the α_2 Precipitates

In materials having the same intrinsic texture (wrought Ti-811 and wrought Ti-811 + HT860), it is shown that the absence of α_2 precipitates only slightly decreased the SCC crack velocity by one to four times (Fig. 4.10). This observation is consistent with the previous work [59] on a rolled Ti-811 plate where the K_{ISCC} was decreased and SCC crack propagation velocity was found to increase by four times in a sample with α_2 precipitates compared to sample without those precipitates.

For the powder HIPped materials (HIPped Ti-811 and HIPped Ti-811 + HT860), Fig. 4.10 shows that the α_2 precipitates had a significant effect. There was no detected SCC crack propagation in the HIPped Ti-811 + HT860 sample without α_2 precipitates. This clearly shows that the effect of α_2 precipitates is different for the samples with (wrought bar) and without (HIPped material) microtexture.

In a previous deformation investigation of a Ti-6.6Al alloy, slip was restricted on basal planes, on which slip bands formed and destroyed the α_2 precipitates [28]. The coherent and fine α_2 precipitates can be sheared by moving dislocations, allowing continuous slip to happen on the active slip plane, which is easier than initiating a new slip on other planes [11, 13, 83]. Therefore, planar slip occurs and a reduction of the SCC resistance are observed in Ti-811. As previous study has identified slip bands on SCC facets of Ti-811 [13]. In the present study, evidence of slip planarity is the slip bands on the SCC facet observed in Fig. 4.13b.

The above paragraph explains why α_2 precipitates are detrimental to the SCC properties. However, it does not explain why they have a more pronounced effect in samples without microtexture (HIPped materials) compared to samples containing microtexture (wrought bar). It seems that the presence of microtexture overrides the effect of α_2 precipitates in wrought samples. Role of α_2 precipitates is promoting planar slip during SCC in both wrought and

HIPped conditions. In wrought Ti-8Al-1Mo-1V with microtexture present, microtexture also promotes planar slip. In addition, dislocations can slip across the grain boundaries and microtexture provides much longer effective slip length at orders of mm. The longer effective slip length increases the local stress at the head of a dislocation pile-up. Hence the effect of α_2 is small in the wrought condition due to the presence of microtexture. While in HIPped condition where microtexture is absent, α_2 is the only initiator for planar slip. Grain boundaries are strong barriers for dislocations, and the effective slip length is limited by α grain size (grain size is about 20 μm). Then new planar slip bands will be activated by α_2 precipitates in neighbouring grains.

Longer slip lengths provided by microtexture could result in a stronger slip planarity and localization [30, 118], which overweighs the effect of slip localization promoted by α_2 precipitates in wrought Ti-811. Therefore, α_2 precipitates have a significant effect when microtextured regions are absent.

4.2.3 Reduction and Elimination of Stress-corrosion Cracking

Susceptibility

Therefore, both microtexture and ordered α_2 precipitates have an effect on the SCC behaviour of Ti-811. Elimination of either one will increase the SCC resistance, and SCC susceptibility can only be totally eliminated when both of them are absent.

It is difficult to remove microtexture from wrought Ti alloys, because these microtextured regions originate from the prior β grains [44, 45] during thermomechanical processing. Therefore, HIPping alone without heat treatment can reduce the SCC susceptibility significantly (see Fig. 4.10) without affecting the property of elastic modulus (see Tab. 4.1). Although HIPped Ti-811 + HT860 samples without both microtexture and α_2 precipitates,

showed no SCC crack propagation at a high stress intensity factor approximately $156 \text{ MPa}\cdot\text{m}^{1/2}$ (see Fig. 4.10), it does have inferior mechanical properties in terms of lower elastic modulus and yield strength (see Tab. 4.1). In this work, it has been demonstrated for the first time that SCC can be suppressed totally when both crystallographic microtexture and α_2 precipitates are eliminated by using a powder HIPping process combined with the heat-treatment, but it comes with inferior mechanical properties in terms of reduced elastic modulus, yield strength and ductility as shown in Tab. 4.1. The post heat-treatment followed by WQ resulted in grain growth, suppressed α_2 precipitation, and an increased volume fraction of β phase, which reduced the yield strength and elastic modulus. However, the decrease in ductility seemed to oppose the effects of larger grain sizes with no precipitation hardening. It may be related to the residual stress associated with the WQ during the post heat-treatment.

4.2.4 Mechanism of Propagation Stress-corrosion Cracking Facets Formation

In Ti-811, the most favourable SCC fracture crystallographic planes identified as either parallel to or $5^\circ - 15^\circ$ from $(0002)_\alpha$, close to $\{10\bar{1}7\}_\alpha$ [13, 17, 59, 75]. Both (0002) and $\{10\bar{1}7\}$ planes are hydride habit plane [13, 15, 17, 64, 68, 75]. The hydride formation mechanism has sluggish kinetics and results in intergranular cracks [13, 67, 69]. However, the plateau SCC crack velocity was found to be high (at the order of 10^{-6} to 10^{-5} m/s in Fig. 4.10) and SCC crack was transgranular in this study. Therefore in Ti-811, the SCC mechanism in aqueous NaCl does not involve hydride formation in Ti-8Al-1Mo-1V.

There was a transition from ductile dimples to flat facets in the fracture modes for the pre-load in air to the SCC in aqueous NaCl solution. Transgranular facets are typical SCC fracture features in $\alpha+\beta$ Ti alloys [13, 63]. The transition happened in all of the wrought bar, wrought Ti-811 + HT860, and HIPped Ti-811. Ordered α_2 precipitates are present in wrought and

HIPped Ti-811, the only difference is that wrought Ti-811 had an intense microtexture aligned in the crack propagation direction and HIPped sample had a homogeneous microstructure without any microtexture. There was no α_2 precipitation in wrought Ti-811 + HT860 sample, but the characteristics of the facets on the fracture surface were similar to that of wrought Ti-811. Therefore, α_2 precipitates should not be the main driving force for the facet formation. Tear ridges and slip bands on the facets indicate that it was not a ‘brittle’ failure, and there was evidence of localized plastic deformation underlying the facets. These ductile features support the concept of Hydrogen Enhanced Localized Plasticity (HELP), in which hydrogen reduces the critical stress of dislocation motion and increases the dislocation velocity in the crack-tip region [67].

In HELP, solute hydrogen interacts with dislocations and promotes dislocation movement in the hydrostatic stress region with a high hydrogen concentration around the crack-tip [22, 57, 58, 65, 119]. However, solute hydrogen concentrations were measured at 34 ppm and 24 ppm for the wrought and HIPped Ti-811 samples, which are considered as low hydrogen levels. Therefore, external hydrogen absorbed as a result of electrochemical activity at the crack-tip may play a significant role in the SCC propagation.

As the SCC tests were conducted in neutral NaCl solution, hydrogen production and absorption seem not to be possible if a stable Ti oxide film is present at the crack tip due to the spontaneous passivation of Ti. However, the local corrosion environment within the SCC crack could be different to that of bulk solution. In an aqueous SCC study of Ti alloys [64], the pH was found to be below 2 at the crack-tip zone for a neutral bulk solution. The low pH value (high hydrogen ion concentration) is a result of oxygen depletion, anodic reaction of Ti, and $TiCl_3$ saturated solution at crack-tip zone [64]. Therefore, Ti oxide film is not stable at crack-tip region due to the low pH and loading in SCC [64]. In order to balance the charge of positive Ti cations created by the anodic dissolution, Cl^- anions diffuse into the crack-tip region and increase the

local Cl^- concentration [64, 85]. The SCC susceptibility increases with the Cl^- concentration in Ti alloys [36]. In addition, the presence of Cl^- reduces the crack-tip potential by anodic depolarization, which then facilitates the hydrogen absorption [64]. As a result, the main hydrogen source is speculated as externally absorbed hydrogen resulting from the reduction of H ions as the cathodic reaction at the crack-tip.

A previous study [13] proposed a facet formation mechanism including hydrogen promoted dislocation motion on rational planes of α phase in the hydrostatic stress region around crack-tip, which results in strain accumulation and subsequent nucleation of secondary cracks. Then the β phase, at the grain boundaries, between α grains failed by ductile rupture. The SCC crack propagates in a repetitive manner as it encounters each new β grain boundary [13]. However, there is no fractographic evidence for the proposed hypothesis in the previous study.

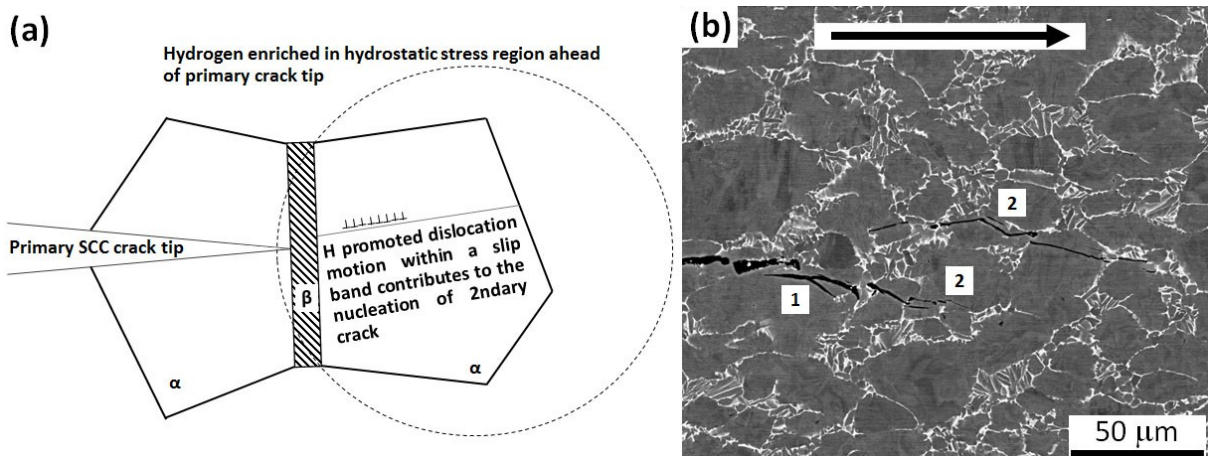


Fig. 4.15. (a) Proposed facets formation mechanism involve hydrogen enhanced localized plasticity (HELP); (b)SE image of cross section view of SCC crack tip in the wrought Ti-811 sample, feature 1 is the primary SCC crack and feature 2 is the secondary SCC cracks. The black arrow indicates the crack propagation direction.

A schematic illustration of the facet formation mechanism is visualized in Fig. 4.15a based on the hypothesis from reference [13]. The cross section view of SCC crack tip, at the test ending point in the wrought Ti-811 sample, is illustrated in Fig. 4.15b. It revealed that secondary cracks (feature 2) were nucleated in α grains ahead of primary crack (feature 1) tip, which encountered grain boundaries containing β phase. The primary SCC crack was continuous, and

secondary cracks were only observed ahead of the primary crack. This is probably because the stress intensity factor was too low (at K_{ISCC}) to join the secondary cracks with the primary crack when the crack arresting happened. This suggests the propagation mechanism, illustrated in Fig. 4.15a, which depicts the nucleation of the secondary crack ahead of the primary crack tip. Also, the nucleation of the secondary crack is attributed to the hydrogen promoted localized dislocation motion in the hydrostatic stress region around crack tip [13].

4.3 Summary

- i. Tear ridges and slip bands on SCC propagation facets indicate a heavily localized plastic deformation in the microstructure adjacent and below the fracture surface, which aligns well with the concept of HELP as the SCC mechanism. The SCC propagation is speculated to be the result of joining the primary with the secondary SCC cracks formed by HELP in α grains ahead of the primary crack-tip. The hydrogen source is mainly provided through externally absorbed hydrogen from the environment at the crack-tip.
- ii. The presence of both α_2 precipitates and microtexture is detrimental to the SCC resistance in Ti-8Al-1Mo-1V. The slip bands on SCC facets are evidence of localized planar slip, which is promoted by α_2 precipitates in the material and HELP mechanism during SCC test, therefore the SCC process is accelerated. The presence of microtextured regions increases the SCC crack propagation velocity significantly, and the SCC crack propagation direction is correlated to the microtexture according to the EBSD maps.
- iii. Ti-8Al-1Mo-1V made from powder by HIPping without any post heat-treatments reduces the SCC susceptibility significantly compared to wrought products prepared by the conventional thermomechanical processing. The HIPped material exhibited minimal microtexture compared to the wrought product.

- iv. A Ti-8Al-1Mo-1V alloy with zero SCC susceptibility can be obtained by combining the HIPping process and appropriate heat-treatment used in the study.

CHAPTER V: STUDY OF THE AQUEOUS SCC MECHANISM(S) IN Ti-8Al-1Mo-1V

Although several hypotheses state that hydrogen is involved in the SCC of Ti-811 [22, 57, 58, 65], there is no published evidence of interrelationships between microstructure, dislocation substructure and the aqueous SCC mechanism for Ti-811. In a study based on Chapter IV [120], a fracture mode transition from dimples to facets was presented at the starting point of aqueous NaCl SCC tests in both wrought Ti-8Al-1Mo-1V bar and powder hot isostatic pressed (HIPped) Ti-8Al-1Mo-1V materials. An understanding of the transition between the pre-crack region (fractured in air) and SCC crack region (failed in 0.1M NaCl aqueous solutions) is needed to reveal the mechanism. The basic aim of this chapter is to reveal the SCC mechanism in Ti-811. This section will investigate the differences in dislocation type and density underlying the dimples and facets, as well as the formation mechanism of SCC facets in Ti-811. Focused ion beam (FIB) provides the means to extract a small volume of material underneath the fracture surface, then transmission electron backscatter diffraction (T-EBSD) and transmission electron microscope (TEM) examination can be conducted to elucidate the SCC mechanism.

5.1 Experimental Results

5.1.1 Fractography

The DCB samples were pre-loaded in air to a length of 3 mm on both side surfaces before immersing in the aqueous NaCl solution. Ductile dimples were found to be the characteristic fracture mode in the pre-crack region of the wrought Ti-811 condition (Fig. 5.1a). Fig. 5.1b shows a typical SCC fracture surface where a dimpled region was observed between transgranular facets indicated by the black arrowhead. The facets were formed at different heights, and their surfaces were covered by aligned ductile tear ridges. The size of facets was about 20 μm , which is similar to that of α grains in the wrought Ti-811 shown in previous

chapter. This suggests that the facets correspond to different α grains. Such a transgranular faceted fracture containing tear ridges is typical for SCC in $\alpha + \beta$ Ti alloys. The observed fracture mode transition indicates a deformation mechanism change in the SCC.

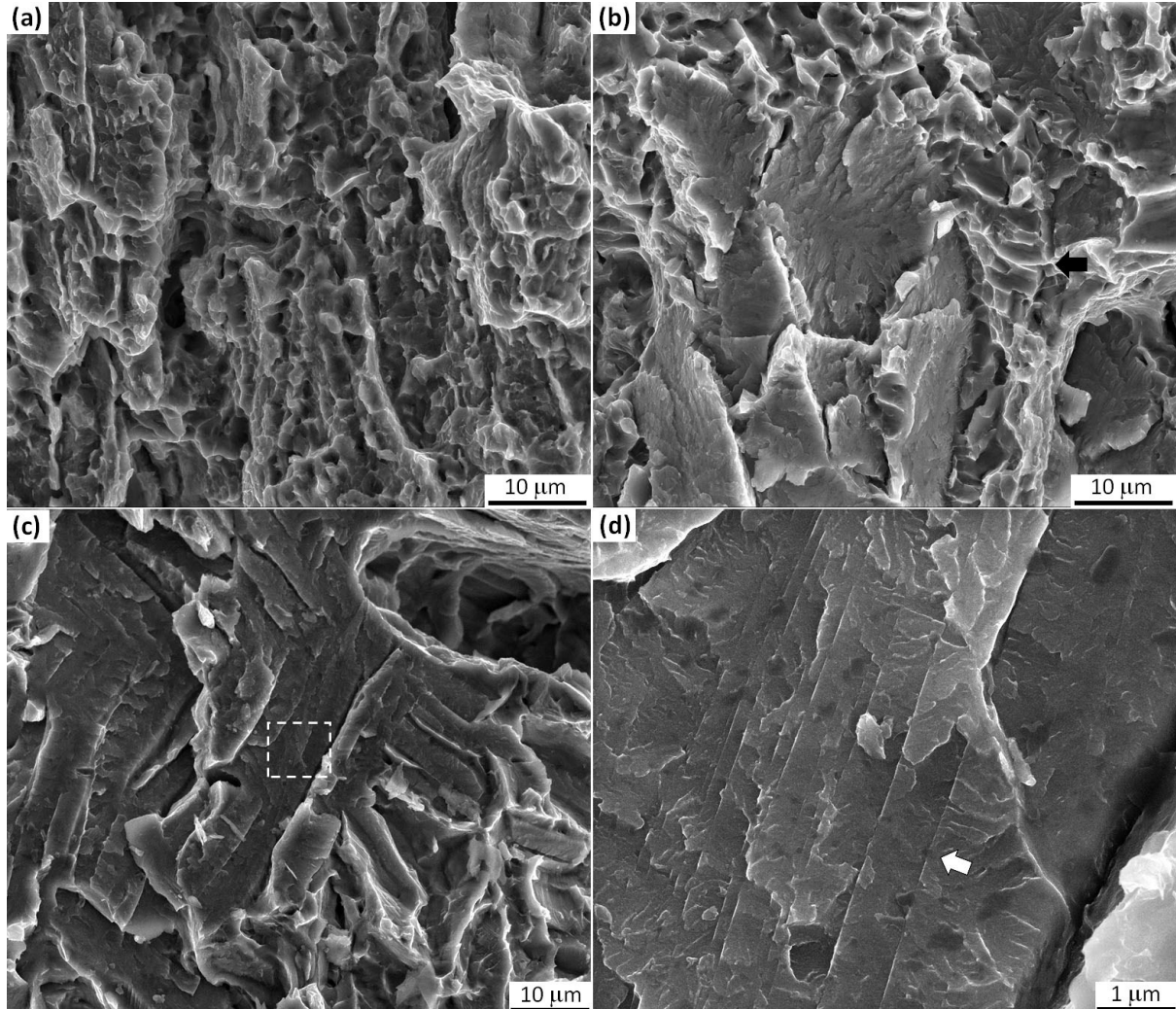


Fig. 5.1. Fractography, (a-b) of wrought Ti-811 (a) dimples on pre-crack failed in air and (b) propagation SCC facets fractured in 0.1M aqueous NaCl solution; (c-d) of HIPped Ti-811 sample (c) propagation SCC facets fractured in 0.1M aqueous NaCl solution and (d) localized slip band observed on facets in white dashed line box in (c).

Similar to the SCC facets of the wrought sample, the fracture characteristics are pre-crack dimples and SCC facets in the HIP-Ti-811 sample according to Chapter IV. As shown in Fig. 5.1c, the SCC fracture surface of a HIPped Ti-811 sample also contained by flat facets. These elongated facets corresponded to the size of lamellar microstructure in HIPped Ti-811 sample. Fig. 5.1d is a close up image of the white dashed line box in Fig. 5.1c. is Fig. 5.1d. In addition

to tear ridges, there were planar slip bands with spacing from 100nm to 800 nm (features denoted by the white arrowhead) on the facet in Fig. 5.1d.

5.1.2 FIB Lift-out and T-EBSD

In order to reveal the SCC mechanism by study the dislocation substructure underneath the fracture surface, FIB lift-out technique was used to extract a small volume of material from either dimples or facets fracture surface. FIB lift-out lamellae were obtained from the dimpled region of the pre-crack (Fig. 5.2b) of the wrought Ti-811 bar, and from the SCC fracture surfaces containing facets of the wrought and HIPped Ti811 samples (Fig. 5.2e, and Fig. 5.2h). A small amount of Pt deposition remained the foils after the final low FIB energy polishing at 2 kV and 27 nA to identify the fracture surface for the facet crystallography analysis. An interesting phenomenon was observed in region 2 of Fig. 5.2e, where a secondary crack was found at the top right corner of black dashed box, and both the secondary crack and main fracture surface were roughly parallel to the $(0001)_\alpha$ plane. Fig. 5.2h shows the foil sectioned from the faceted region of HIPped Ti811, and the insert is an enlarged image of region 3. Stair-like steps were observed on the facets with a spacing of approximately 700nm, which was expected as the planar slip bands similar to Fig. 5.1d.

As fraction of β phase was about 10% in both wrought and HIPped Ti-811, thus pole figures were only computed for α -Ti texture. With all the three lamellae, the loading condition was tensile stress along vertical direction (red arrows in Fig. 5.2b, e and h). Fig. 5.2c is the pole figure of region 1 in Fig. 5.2b. There is a strong basal pole in the area of interest and the $[0001]_\alpha$ direction is inclined approximately 25° away from the tensile direction. For region 2 beneath facets (the faceted region (Fig. 5.2e), all the data points have their c-axis inclined approximate 45° away from the loading direction. As the size of α grains were in the range of $20\text{-}30\mu\text{m}$ in the wrought Ti-811, the EBSD mapping area (black dashed box) of $2 \times 2 \mu\text{m}^2$ indicates that it

could be a single grain in region 2, which agrees with the pole figure data. For region 3 beneath SCC facets of HIPped Ti-811 (Fig. 5.2h), the basal pole is approximately 6° away from the loading axis.

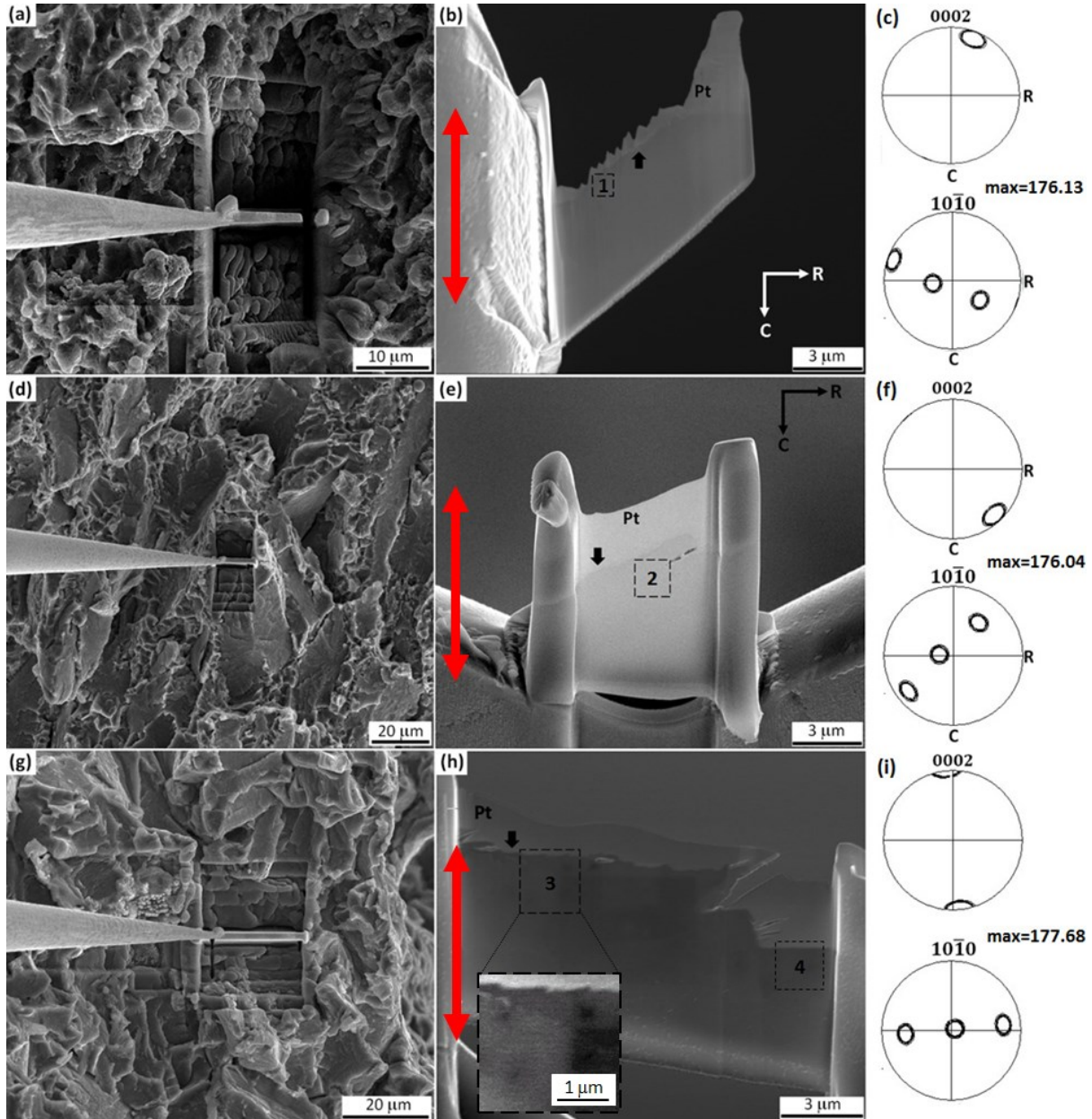


Fig. 5.2 (a-f) FIB lift-out lamellae obtained from a fractured wrought Ti-811 sample, (a) and (b) from pre-crack dimpled fracture, (d) and (e) from SCC faceted fracture. Pole figures of α phase, (c) the pole figure corresponding to region 1 in (b), (f) the pole figure corresponding to region 2 in (e). (g-i) FIB lift-out lamella obtained from a fractured HIPped Ti-811 sample, (g) and (h) from SCC faceted fracture, and the insert in (h) is an enlarged view of region 3; (i) the pole figure corresponding to region 3 in (h). All the fracture surfaces beneath the platinum (Pt) deposition are denoted by the black arrowheads, and all the red arrows denote the tensile direction in (b), (e) and (h).

Based on the tensile loading direction (vertical direction in Fig. 5.2b, 5.2e, and 5.2h) and crystallographic orientations in the grains of interest, the relative critical tensile stress (σ_c) can then be calculated by the Schmid factor (m) and Critical Resolved Shear Stress (CRSS, τ_c) for various slip systems in α -Ti grains as following Eq. (5.1):

$$\sigma_c = \tau_c/m \quad (5.1)$$

The slip system with the lowest σ_c will be preferentially activated. As CRSS data for various slip systems in α phase of Ti-811 are not available, a reference relating to a Ti-6.6Al single crystal at 300 K was adopted considering its high Al content [28]. The combination of basal and prismatic $\langle a \rangle$ slip systems which gives a pyramidal $\langle a \rangle$ slip, was not considered here. The CRSS of $\langle c + a \rangle$ slip systems is roughly four times as high as that of $\langle a \rangle$ slip on either the basal or prismatic planes. Different types of $\langle c + a \rangle$ slip systems generally have not been listed clearly in numerous CRSS studies. Therefore, the same CRSS was used in our study for the first-order pyramidal $\{10\bar{1}1\}$ and second-order pyramidal $\{11\bar{2}2\}$ $\langle c + a \rangle$ slip [121, 122].

Tab. 5.1 lists the Schmid factors and relative σ_c of various slip systems in regions 1-3 as shown in Fig. 5.2. Although the α -Ti grain in region 1 is orientated such that $\langle c + a \rangle$ slip systems had the highest Schmid factor, the relative σ_c is still lower for basal $\langle a \rangle$ slip due to the high relative CRSS of $\langle c + a \rangle$ slip. Therefore, basal $\langle a \rangle$ slip is the easiest activated slip system compared to other systems in region 1. For region 2, the basal plane is inclined approximately 45° away from the loading axis, which means that the Schmid factor will be the highest for basal $\langle a \rangle$ slip, thus the basal $\langle a \rangle$ slip will be preferentially activated. In region 3, beneath the SCC facets of a HIPped Ti-811 sample, the c -axis is close to the stress axis which results in a high Schmid factor for pyramidal $\langle c + a \rangle$ slip systems, and a low relative σ_c in turn. However, the difference between the relative σ_c of $\langle c + a \rangle$ slip systems and basal $\langle a \rangle$

slip system is small, only about 20%. Unlike the other two regions (1 and 2) orientated favourably for basal $\langle a \rangle$ slip, the $\langle c + a \rangle$ slip will be preferentially activated in region 3.

Tab. 5.1. Schmid factors, relative CRSS and relative critical tensile stress for various slip systems for the interested regions of FIB lift-out lamellae in Fig. 5.2b, e and h.

Slip systems*		Schmid Factor (m)	Relative CRSS (τ_c) [28]	Relative Critical tensile stress (σ_c)
$\langle a \rangle$	(0001)	0.368 - 0.369	0.2625	0.711 - 0.713
	{10̄10}	0.076 - 0.077	0.2375	3.084 - 3.125
Region 1: underneath dimples in wrought Ti-811				
$\langle c + a \rangle$	{10̄11}	0.497 - 0.498	1	2.008 - 2.012
	{11̄22}	0.463	1	2.16
Region 2: underneath SCC facets in wrought Ti-811				
$\langle a \rangle$	(0001)	0.493 - 0.500	0.2625	0.525 - 0.532
	{10̄10}	0.194 - 0.250	0.2375	0.950 - 1.224
$\langle c + a \rangle$	{10̄11}	0.345 - 0.411	1	2.433 - 2.899
	{11̄22}	0.255 - 0.319	1	3.135 - 3.922
$\langle a \rangle$	(0001)	0.075 - 0.109	0.2625	2.408 - 3.5
	{10̄10}	0.003 - 0.007	0.2375	33.93 - 79.17
Region 3: underneath SCC facets in HIPped Ti-811				
$\langle c + a \rangle$	{10̄11}	0.444 - 0.457	1	2.188 - 2.252
	{11̄22}	0.478 - 0.487	1	2.053 - 2.092

*Where $\langle a \rangle$ -type slip systems have slip direction in $\langle 11\bar{2}0 \rangle$, and $\langle c + a \rangle$ -type slip direction is $\langle 11\bar{2}3 \rangle$

5.1.3 Dislocation Contrast Analysis

After the FIB lift-out experiment, all FIB lamellae were subjected to dislocation contrast analysis, and the same areas in the black dashed boxes were investigated. As shown in Fig. 5.3a, t the c -axis is consistent with the pole figure in region 1 (Fig. 5.2c). Fig. 5.3b and c are high magnification images for Fig. 5.3a. During the dislocation contrast analysis, the electron beam was tilted a few degrees away from the $[2\bar{1}\bar{1}0]$ zone axis to obtain the appropriate g

vector. The basal plane was approximately on edge and parallel to the beam direction. The distribution of dislocations seems to be heterogeneous in region 1. Straight dislocation segments were on $(0002)_\alpha$ planes from 600 to 1500 nm beneath the fracture surface (below the Pt deposition) when $g = [01\bar{1}\bar{1}]$ was operating. Most of the straight features were extinct under $g = [0002]$, which suggests that they had a $\langle a \rangle$ type Burgers vector. However, two planar slip bands with a thickness of 20 nm (see white arrowheads in Fig. 5.3b) remained visible under $g = [0002]$. One explanation is that they are bands of $\langle c + a \rangle$ dislocations, which have contrast under both $g = [0002]$ and $g = [01\bar{1}\bar{1}]$. However, $\langle c + a \rangle$ type dislocations glide on pyramidal planes, and they are not expected as edge on features residing on the basal plane when the electron beam direction is approximately parallel to $[2\bar{1}\bar{1}0]$. Another possibility is that the two slip bands are residual contrast of $\langle a \rangle$ type edge dislocations. Despite the invisibility criterion $g \cdot b = 0$, the strain field raised from a high density of $\langle a \rangle$ type edge dislocation debris in the bands leads to an incomplete vanished contrast [123]. Therefore, arrays of dislocations including the two slip bands can be determined as $\langle a \rangle$ type dislocations on the basal plane, which is predicted and confirmed by the relative σ_c calculation in Tab. 5.1.

The deformed substructure underneath the facets (region 2) in wrought Ti-811 is shown in Fig. 5.4. The black arrowhead at top right corner denotes the secondary crack that is aligned on the basal plane. TEM shows the same crystallographic orientation to the pole figure in Fig. 5.2g. The bright field micrograph of Fig. 5.4a shows a high density of dislocations with $b = \langle c + a \rangle$ under $g = [0002]$, which were not observed in region 1 beneath the dimples Fig. 5.3. When $g = [0\bar{1}11]$ reflection was excited, localized planar slip bands and straight dislocation segments were observed gliding on the basal plane, while there were no dislocations with a $\langle c \rangle$ component. As B was close to $[2\bar{1}\bar{1}0]$, the dislocation arrays and bands that resided on the basal plane were determined to be basal $\langle a \rangle$ slip in Fig. 5.4b. The activation of basal $\langle a \rangle$ slip in region 2 was also predicted by Schmid's law calculations (Tab. 5.1). In addition to the predicted

basal $\langle a \rangle$ slip, $\langle c + a \rangle$ slip is also present in region 2 (Fig. 5.4a). The feature originated from the secondary crack tip denoted by the white arrowhead was a sub-grain boundary in Fig. 5.4b, and grains on each sides of the boundary had a misorientation of 1.4° (see the SAD pattern (Fig. 5.4c) taken from the yellow circle in Fig. 5.4b). The small angle sub-grain boundary is not an effective barrier for dislocation motion, and therefore the slip bands are continuous across the boundary in Fig. 5.4b.

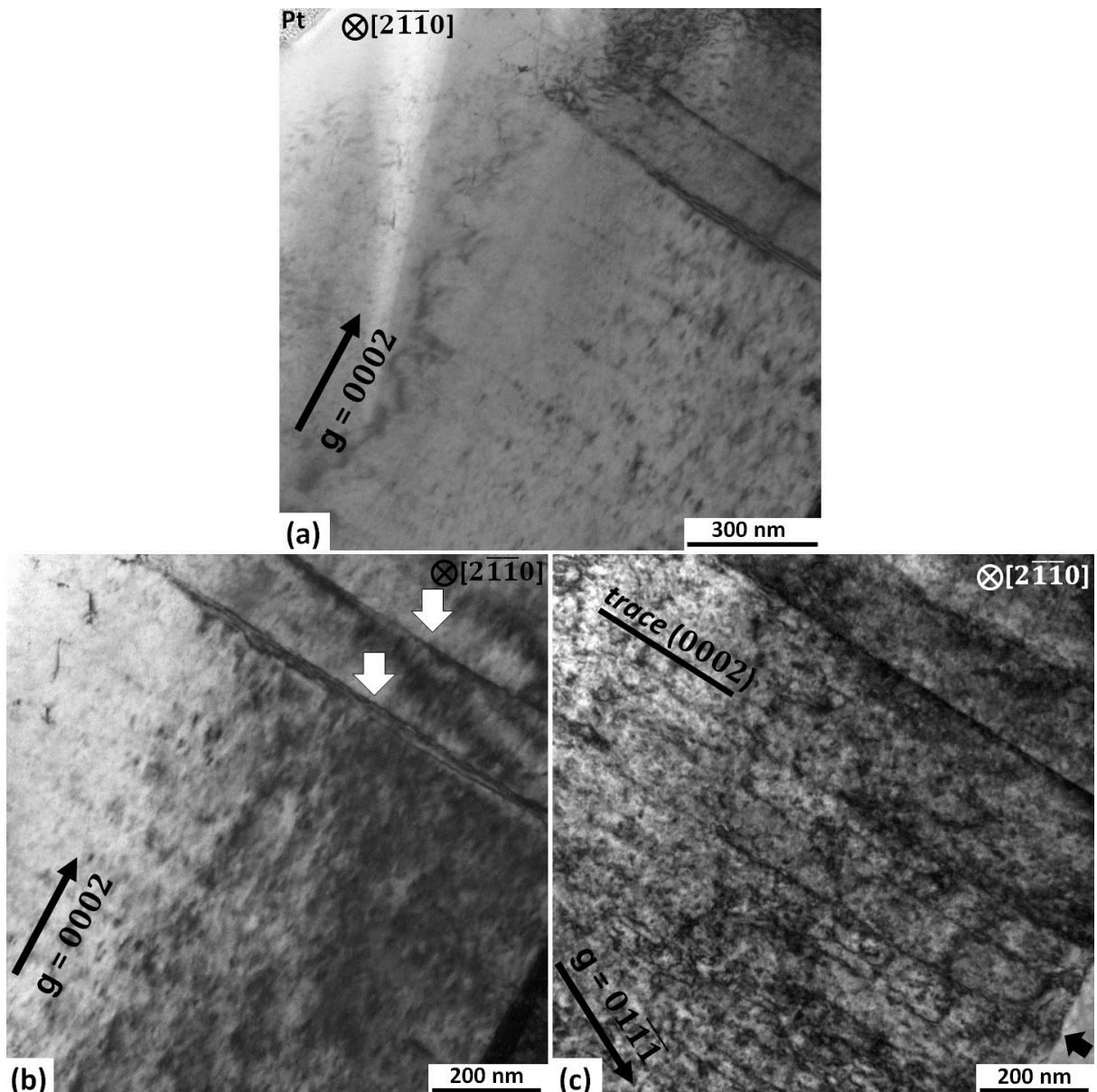


Fig. 5.3. Bright Field (BF) TEM micrographs of region 1 lift-out from the pre-crack dimples of wrought Ti-811 in Fig. 5.2b. Low magnification (a) $g = [0002]$, high magnification (b) $g = [0002]$, the white arrowheads indicate two planar slip bands, (c) $g = [01\bar{1}1]$, the black arrowhead denotes a grain boundary at bottom right, $B \approx [2\bar{1}\bar{1}0]$. In all case black arrow indicates the excited g vector.

The interim crack length was shorter in the dimpled region of pre-crack than that of the SCC facets. As the SCC test was a constant displacement test, the stress intensity factor (K) has an inverse relationship with the interim crack length according to Equation 3.1. Therefore K was decreasing during the crack propagation (increased crack length) and stress intensity factor was higher for dimpled regions than that of the faceted regions. However, higher dislocation density was presented in the material underneath facets than that of dimples according to the contrast analysis in Fig. 5.4 and Fig. 5.3 respectively. This will be further discussed in section 5.2.

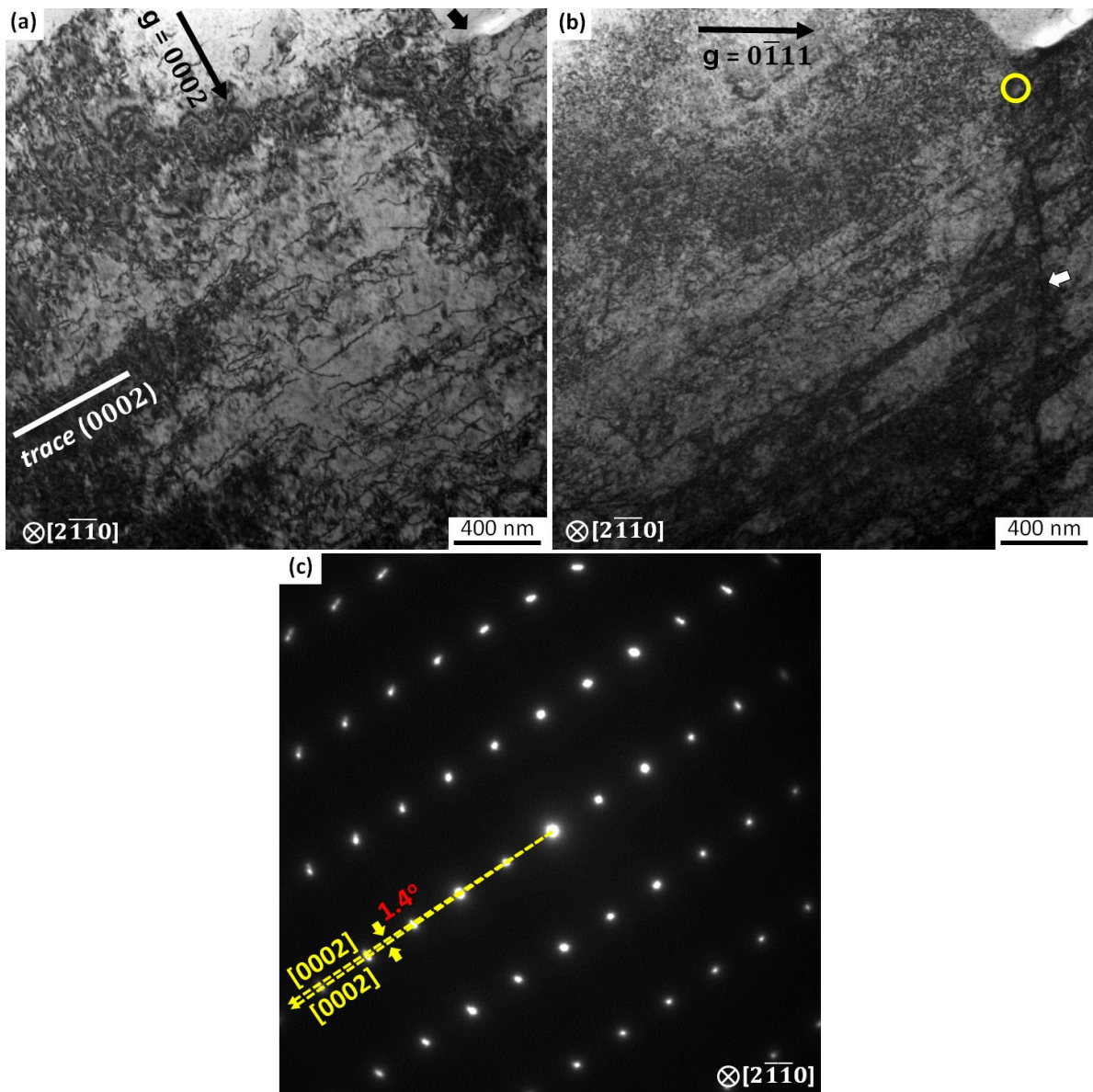


Fig. 5.4. BF TEM micrographs of region 2 lift-out from the SCC facets of wrought Ti-8Al sample in Fig. 5.2e. (a) BF image when $g = [0002]$ is excited, the black arrowhead denotes the secondary crack tip which is previously illustrated in Fig. 5.2 (e); (b) BF image when $g = [0\bar{1}11]$ is excited, white arrowhead indicates a sub-grain boundary; (c) Selective area diffraction (SAD) pattern taken from the yellow circle in (b). $B \approx [2\bar{1}\bar{1}0]$. In all case black arrow indicates the excited g vector.

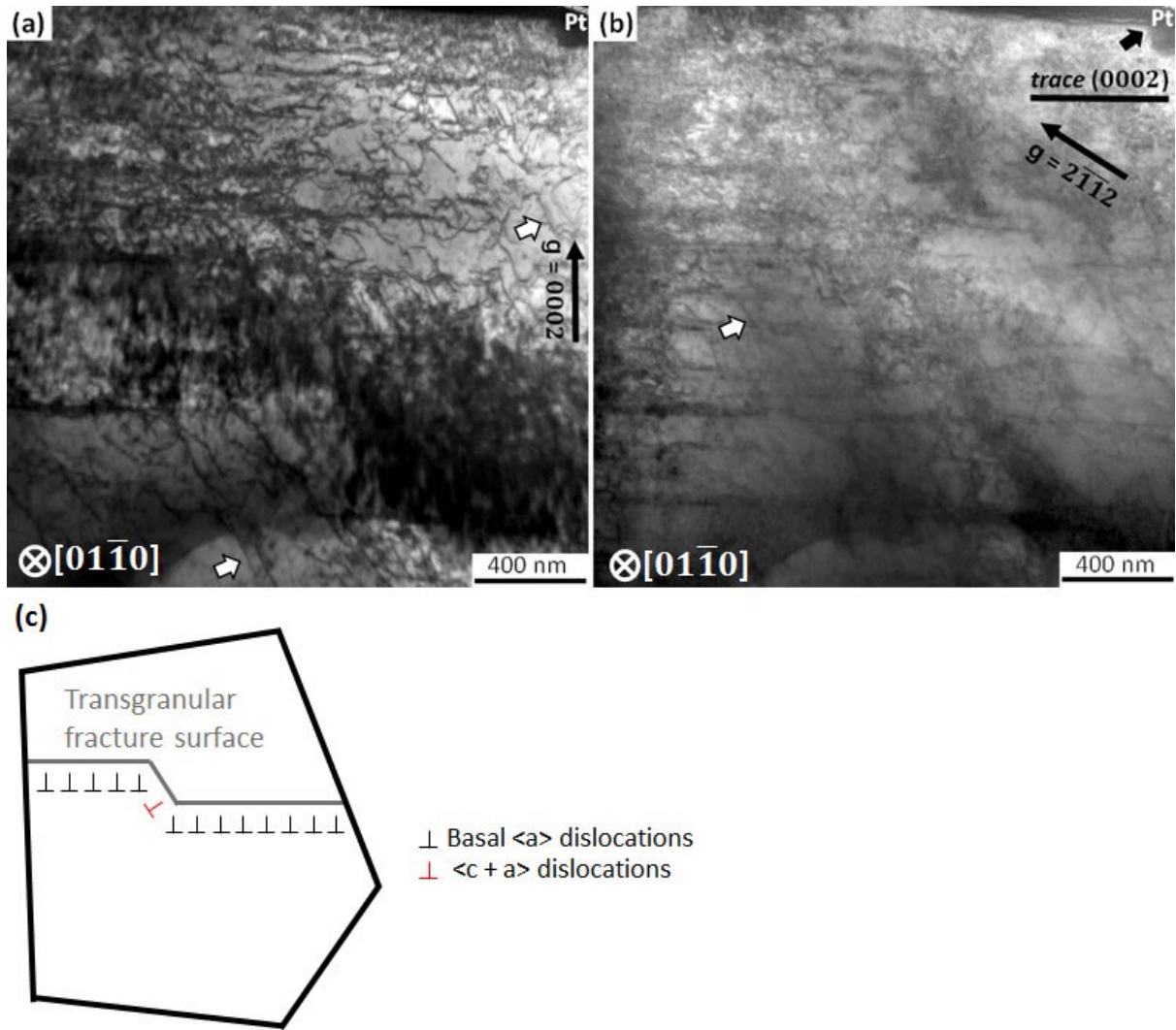


Fig. 5.5. BF TEM micrographs of region 3 lift-out from the SCC facets of HIPped Ti-811 sample in Fig. 5.2h. (a) $g = [0002]$, (b) $g = [2\bar{1}\bar{1}2]$, (c) proposed steps formation mechanism on facets in α grain. The white arrowheads indicate the linear $< c + a >$ segments resided on the $(\bar{2}112)$ plane, and the black arrowhead denotes a step on facet surface. $B \approx [01\bar{1}0]$, In all case black arrow indicates the excited g vector.

Fig. 5.5 provides BF images taken with diffraction conditions of $g = [0002]$ and $[2\bar{1}\bar{1}2]$ for region 3 underneath the faceted fracture of HIPped Ti-811. Highly localized basal $< a >$ slip bands were observed to be parallel to the (0002) trace underneath the facet containing steps for $g = [2\bar{1}\bar{1}2]$. In addition to $< a >$ slip, a high density of $< c + a >$ entanglements appeared from areas very close to the surface to that 1600nm beneath when $g = [0002]$ was excited. Besides, linear $< c + a >$ dislocation segments were also observed on $(\bar{2}112)$ plane, which are indicated by the white arrowheads. In region 3, activation of $< c + a >$ slip is predicted by Schmid's law calculation in table 2. Fig. 5.5c is an illustration of steps formation on faceted

fracture surface by $\langle c + a \rangle$ slip joining the neighbouring basal $\langle a \rangle$ slip bands, and it will be elaborated in details in the discussion section.

5.2 Discussion

The nature of dislocation and density of dislocation will be discussed in the following sections. To help identify the mechanisms involved in the SCC of Ti-811, the nature and density of dislocations will be discussed in the following sections. It is possible that they could be affected by the ion beam damage during the FIB lift-out sample preparation stage. Previous studies [113-115] have identified defects, including dislocations, produced by high energy Ga^+ ion damage in FIB lift-out foils. However, a recent study on a near α Ti alloy showed that FIB lamellae, which were prepared by using a sequentially reduced ion beam energy during the thinning process and a final low polishing voltage and current at 2 kV and 28 pA, had a comparable sample quality with electropolished foils in the dislocation contrast experiment [116]. In the current study, a low energy ion beam at 2 kV and 27 pA was used in the final polish process. Therefore, FIB lift-out conducted in our experiment is not expected to affect the dislocation analysis.

5.2.1 Nature of Dislocation

From the TEM contrast analysis, basal $\langle a \rangle$ glides were observed in both regions 1 and 2 from dimpled and faceted fracture of the wrought Ti-811 material respectively. The activation of such type dislocation was predicted by the relative critical tensile stress (σ_c) calculation in Tab. 5.1. In addition to the basal $\langle a \rangle$ dislocation, $\langle c + a \rangle$ dislocations were observed only underneath the facets (region 2 illustrated in Fig. 5.4). In general, $\langle c + a \rangle$ glide is expected to be important for ductility in α titanium with a HCP crystal structure, because it provides the additional independent slip systems for a homogeneous plastic deformation according to von Mises criterion [8, 124-127]. Therefore, one would have expected to find $\langle a \rangle$ as well as $\langle c + a \rangle$ dislocations in the fractured surface.

$a>$ type dislocations beneath the dimpled fracture. Instead they were observed underneath facets in the SCC regions which are associated with brittle failure. Thus “facets” need not be regarded as brittle failure, because there were extensive tear ridges and planar slip bands observed on facets surface. Such tear ridges and planar slip bands on facets are indications of microplasticity [13, 75, 128], which suggests a high degree of dislocation activity at the crack tip. Previous research in Ti-811 proposed an assumption that either basal $< a >$ slip or $< c + a >$ slip are promoted in the SCC crack tip region enriched with hydrogen [13]. For the first time, direct evidence has been provided for the role of hydrogen in SCC. Therefore, hydrogen induced dislocation emission seems likely to be related to the activation of $< c + a >$ slip below facets.

5.2.2 Dislocation Density

The self-loaded SCC experiment was a constant displacement test. Therefore, the stress intensity factor was reducing during crack propagation which means the stress intensity factor was much higher in the dimpled region at pre-crack than that of propagation facets formed subsequently. However, a higher density of dislocation was observed below the SCC faceted crack region (region 2 illustrated in Fig. 5.4) compared to that below dimples (region 1 illustrated in Fig. 5.3) for wrought Ti-811 sample. The difference in dislocation density may help us to reveal the aqueous NaCl SCC mechanism in Ti-811.

Several studies of hydrogen effects on dislocation showed that hydrogens lowered the dislocation emission energy [129], as well as reduced the flow stress and increased dislocation velocity along a narrow slip band [67, 129-131]. Another hydrogen embrittlement (HE) study pointed out that hydrogen stabilizes edge components of mixed dislocations, therefore it prohibits cross slip [130]. In summary of the previous HE work, hydrogen promotes dislocation emissions and increases dislocation motions on confined crystallographic planes, which results

in a high dislocation density, localized slip bands and a macroscopically high crack velocity. The concept of all these HE studies are similar to the experiment observations in the current work. High density of localized planar basal $\langle a \rangle$ slip bands and $\langle c + a \rangle$ dislocations below the facets, which are covered by extensive plastic tear ridges is a suggestion of hydrogen promoted dislocation emission and motion at hydrostatic stress regions of the crack tip. Therefore, the aqueous NaCl SCC mechanism in Ti-811 is possibly related to the effect of hydrogen on dislocation emission and motion.

5.2.3 Hydrogen Diffusion

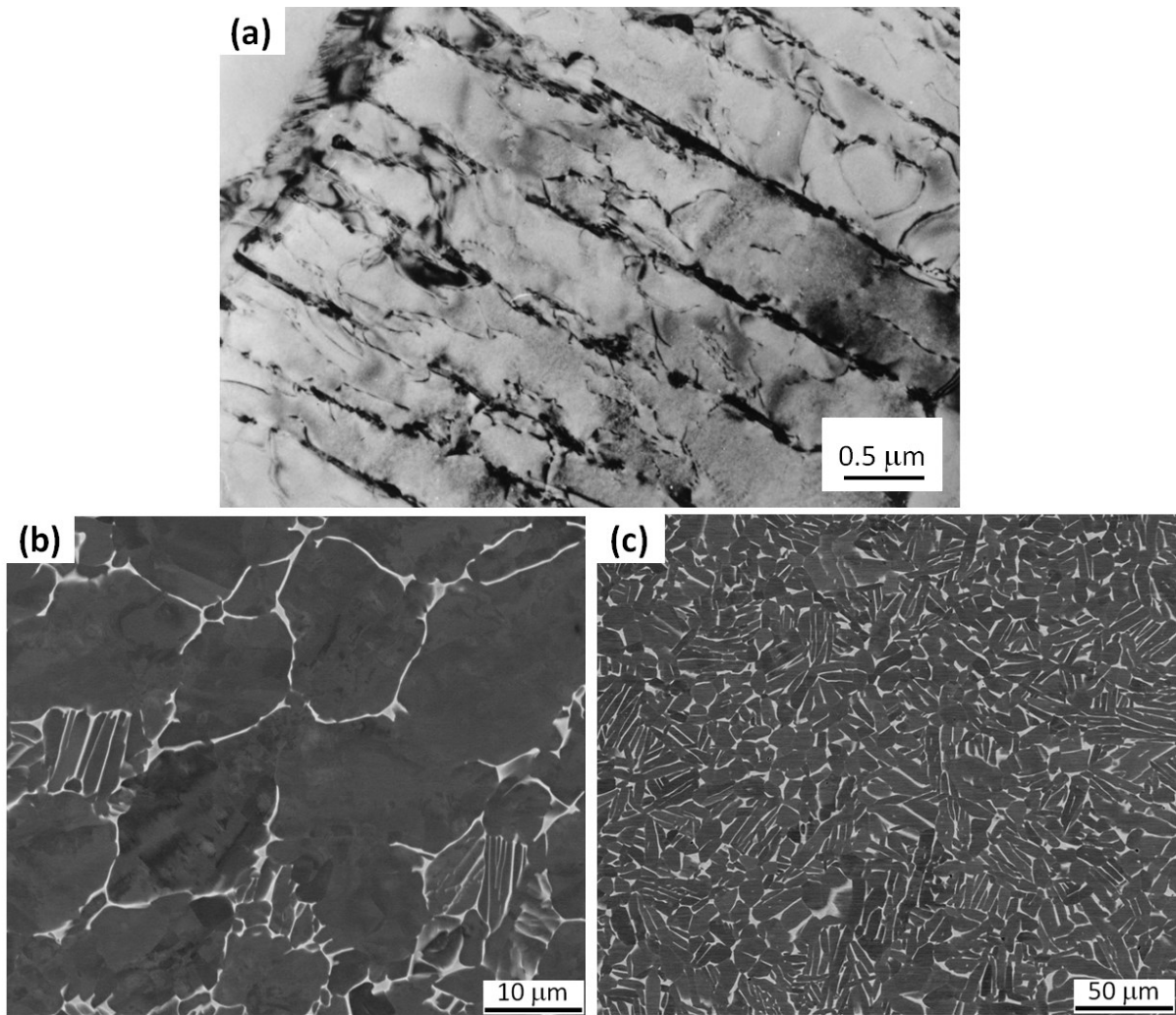


Fig. 5.6. (a) BSE SEM image of the fully lamellar IMI834 alloy in the study of [87], (b) BSE SEM image of the wrought Ti-8Al-1Mo-1V alloy with a bi-modal microstructure used in the current study, (c) BSE SEM image of the HIPped Ti-8Al-1Mo-1V alloy used in the current study.

Solute hydrogen concentrations were about 34 ppm and 24 ppm (see Tab. 3.2) for the wrought and HIPped Ti-811 samples, and they were regarded as low hydrogen levels. Thus, absorbed hydrogen from the vicinity fluid played a significant role in the present SCC study. As described in the introduction section, hydrogen absorption was triggered by electrochemical charging at the crack tip, and the absorbed hydrogen then diffused into the material.

As there is no published data of D_{H_0} and Q for Ti-811, a reference of a near α Ti alloy, IMI834, is adopted in Tab. 1.3. Therefore at room temperature (300K), $2.63 \times 10^{-14} \text{ m}^2/\text{s}$ was the overall diffusion coefficient for IMI 834, in which the spheroidized β phase existed in lamellae region (see Fig. 5.6a) [87]. However, both the wrought and HIPped Ti-811 had an interconnected β phase network (bright β phase in Fig. 5.6b and c), the overall diffusion coefficient should be higher than the calculated $D_{H-\text{IMI834}}$. In addition, it is also expected to be lower than the bulk diffusion in β phase, as there are α grains and lamellae acting as barriers in Ti-811, which confines the diffusion path. Therefore diffusion coefficient of β Ti is the upper limit. $D_{H-\beta}$ is about $2.89 \times 10^{-12} \text{ m}^2/\text{s}$ at 300 K according to Tab. 1.3 [88].

Hydrogen is an interstitial element in Ti alloys, and its solubility and diffusivity is much higher in β phase compared to in α phase due to the low pack density in BCC crystal. As a result, a more rapid diffusion of absorbed hydrogen can be achieved by the interconnected β phase into the bulk material [22]. In addition, there will be a hydrogen concentration gradient developed around the crack tip during the hydrogen charging and diffusion [86, 132, 133].

An estimation of the hydrogen diffusion length by lattice diffusion is [134]:

$$L_H = \sqrt{2D_H t} \quad (5.2)$$

Where t is the diffusion time and D_H is the diffusion coefficient, which is a function of temperature [87]:

The bulk hydrogen diffusion rate (diffusion length/time) is then calculated by equation (5.2), and they are 2.40×10^{-6} m/s for β Ti and 2.30×10^{-7} m/s for IMI834. Therefore, the overall hydrogen diffusion rate should be in the range between 2.30×10^{-7} m/s and 2.40×10^{-6} m/s for Ti-811. As the plateau SCC crack velocity is in the order of 10^{-5} m/s in Chapter IV (Fig. 4.10), which is still at least one magnitude higher than the calculated hydrogen diffusion rate. This indicates that bulk hydrogen diffusion is not sufficient for hydrogen enhanced localized plasticity mechanism operating in such a high crack velocity case.

Hydrogen segregation on mobile dislocations must account for the high cracking velocity. Hydrogen diffusivity can be increased by transportation through dislocations [30, 89, 91, 135-137], especially for the presence of planar slip bands which allow longer slip length [30, 90, 136]. Hydrogen transport through slip bands was reported in various systems including steel [93], Al [90], and Ti [30, 92, 138]. It was stated that pipe diffusion along dislocation is kinetically preferred to volume diffusion, and the hydrogen diffusion rate was increased by orders of magnitude through the pipe diffusion [89, 90]. The coherent ordered α_2 precipitates lead to localized planar slip bands with a length longer than 1 μm underneath SCC fracture surface (Fig. 5.4b and Fig. 5.5b). These planar slip bands then provided transport highway for the absorbed hydrogen at the crack tip to diffuse into grain interior at a high rate. As calculated in the above paragraph, the SCC crack velocity was at least one magnitude higher than the bulk hydrogen diffusion rate in Ti-811. Therefore, hydrogen transport through slip bands helps to keep pace with the high SCC crack velocity. In addition to the hydrogen segregation and diffusion, the hydrogen concentration is high within the slip bands, which leads in turn to an easier crack propagation along the slip bands [8].

5.2.4 Crystallographic Orientation of SCC Faceted Planes

SCC fracture planes were reported to be close to (0002) plane in Ti-811 [13, 17, 36, 59], and they were determined to be inclined 5° to 15° away from the basal plane by using quantitative tilt fractography/EBSD method [13]. Coincidentally, a well-known hydride habit plane {10 $\bar{1}$ 7} is approximately 15° from the (0002) plane. However, hydride formation and fracture mechanism was not suitable for the SCC of Ti-811 as previously mentioned in section 0 and section 0. The tear ridges and localized slip bands observed on the facets (Fig. 5.1b, c and d) are ductile features and are indications of microplasticity.

In the current study, three FIB lift-out lamellae, including region 2 to 4, were examined by TEM from wrought and HIPped Ti-811 samples. BF TEM images of facet surface of these three regions are illustrated in Fig. 5.7, and facet crystallographic orientations are summarized in Tab. 5.2 based on the SAD patterns in Fig. 5.7.

As shown in Fig. 5.7a and b respectively, the main faceted surface of regions 2 and 3 below the Pt deposition layer are parallel to (0002)_a. Especially for region 2, which also has a secondary crack on the basal plane (see the black arrow head in Fig. 5.7a). Fig. 5.7c shows a facet (above region 4) formed on a plane inclined 16.4° away from the basal plane, which is close to a hydride habit plane {10 $\bar{1}$ 7}. In all three cases, $\langle c + a \rangle$ entanglements appear underneath the facet.

The three direct observations showed that facet formations were on planes either parallel to, or inclined 15° away from, the basal plane, which was an incomplete consistency with the range of 5° to 15° away from the basal plane in the previous study [13]. The method of quantitative tilt fractography/EBSD measured the average orientation of a facet plane and had an accuracy of $\pm 3^\circ$ [13, 75], while BF TEM images of the lift-out foils provided direct observations. The average measurements on facets with those ductile features on facets, including planar slip

bands and tear ridges, may also have contributed to the inconsistency of the crystallographic orientation.

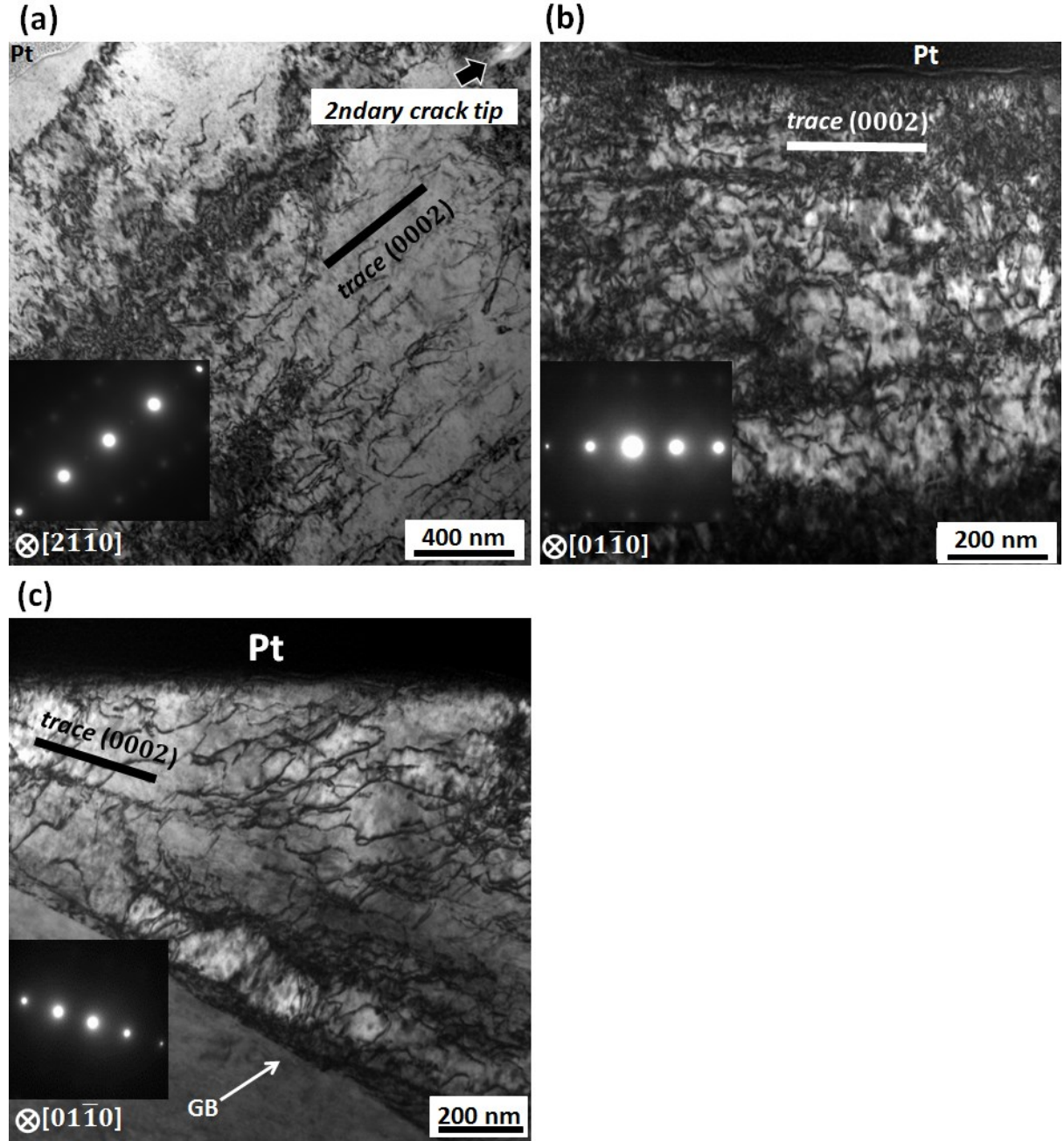


Fig. 5.7. BF TEM micrographs of (a) region 2 lift-out from the SCC facet of wrought Ti-811 sample in Fig. 5.2e, and the black arrow head indicates the secondary crack tip, $B \approx [2\bar{1}\bar{1}0]$, (b) region 3 lift-out from the SCC facet of HIPped Ti-811 sample containing the surface steps in Fig. 5.2h, $B \approx [01\bar{1}0]$, (c) region 4 lift-out from the SCC facet of HIPped Ti-811 sample in Fig. 5.2h, $B \approx [01\bar{1}0]$. The main fracture surface is below the Pt deposition in all cases, and trace of $(0002)_\alpha$ planes are indicated by the SAD patterns.

For regions 2 and 3, faceted planes on $(0002)_\alpha$ could be a result of the fracture propagation along basal $\langle a \rangle$ slip bands, which are illustrated in Fig. 5.7a and b. A slight difference is that the fracture surface contained steps formed by joining adjacent basal $\langle a \rangle$ slip bands rather than

a single slip band in region 3. The facet plane of region 4 (Fig. 5.7c) is approximately 16° from (0002) _{α} , or close to irrational {10̄17} planes. However {10̄17} are not slip planes, the overall propagation facet on {10̄17} could be a result of operation of both the pyramidal $< c + a >$ slip and basal $< a >$ slip. Therefore, the facet orientation is related to the operating dislocations underneath.

Tab. 5.2. Crystallographic orientations of SCC facets investigated in Fig. 5.7.

Samples	Angle between facet normal and [0001] _{α} (°)
Facet of region 2 in wrought Ti-811	0 [#]
Facet of region 3 in HIPped Ti-811	0 *
Facet of region 4 in HIPped Ti-811	15

[#] For main fracture surface and secondary crack tip. *For the horizontal part of the step.

5.2.5 SCC Mechanisms

The tear ridges on facets were evidence of microplasticity [13, 75, 128], which indicated a high degree of dislocation activity at the crack tip. A Previous study proposed a hypothesis, in which either basal $< a >$ slip or $< c + a >$ slip were promoted in the SCC crack tip region enriched with hydrogen [13], and now the first direct TEM evidence is provided by the present work.

The ductile features of steps with spacing at a few hundred nanometres on the facet of region 3 (Fig. 5.5) were related to the planar slip band features on facets (Fig. 5.1d). These steps are fractographic evidence of highly localised plastic deformation. According to the dislocation contrast analysis, extensive basal $< a >$ slip bands and pyramidal $< c + a >$ dislocations are observed beneath the facets. As these steps are parallel to the (0001) _{α} plane, it is suggested that step formation is a result of $< c + a >$ dislocations joining neighbouring basal $< a >$ slip bands in Fig. 5.5c.

In SCC of Ti alloys, the pH was found to be below 2 at the crack-tip zone for a neutral bulk solution [64]. The low pH value (high hydrogen ion concentration) is a result of anodic reaction of Ti, and hydrolysis of Ti ions at the crack-tip zone [64]. Then, hydrogen absorption is a result of cathodic electrochemical reactions at SCC crack tip [64]

Therefore, the absorbed hydrogen weakens the interatomic band, promotes dislocation emission and increases the dislocation density around the crack tip by AIDE. The diffused hydrogen then promoted a localized plastic deformation ahead of the crack tip by HELP. The overall crack propagation was a result of the accumulation of highly localized plastic deformation in the vicinity grains ahead of the crack tip. Thus, a combined AIDE and HELP mechanism schematically shown in Fig. 5.8 is proposed for the SCC of Ti-811 in aqueous NaCl solution.

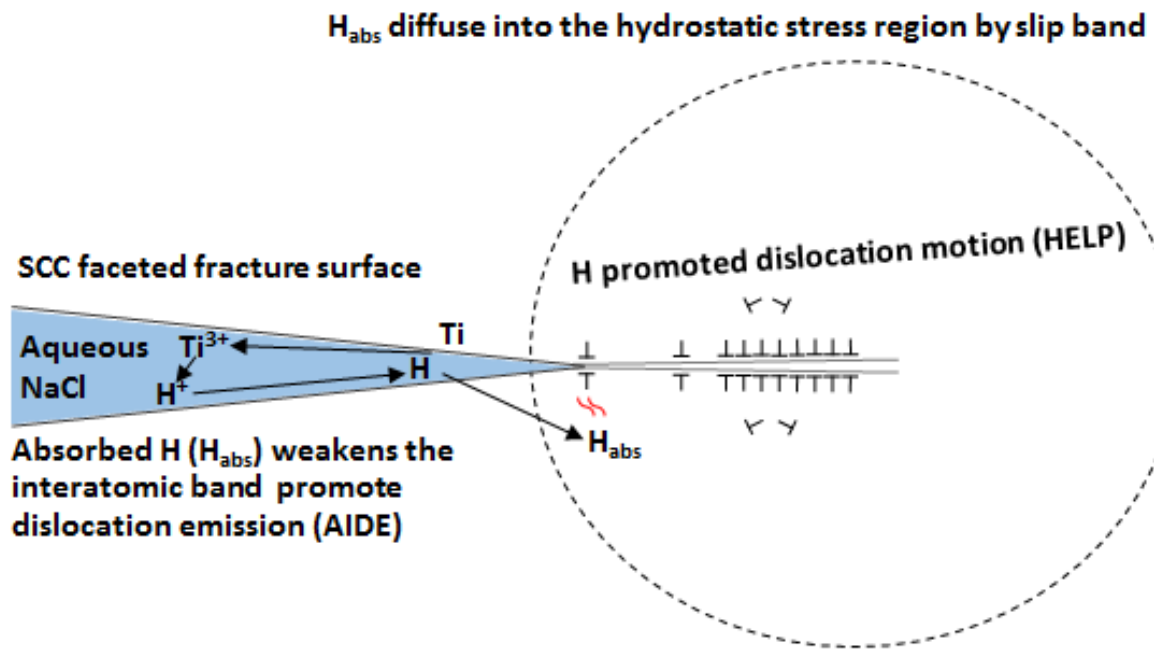


Fig. 5.8. Illustration of a hybrid aqueous NaCl SCC mechanism including absorption induced dislocation emission (AIDE) and hydrogen enhanced localized plasticity (HELP) for Ti-8Al-1Mo-1V. H_{abs} is the absorbed hydrogen.

5.3 Summary

In order to understand the SCC mechanism, a combination of FIB lift-out, T-EBSD, and TEM contrast analysis were applied to study the substructure of α grains underneath dimpled and SCC faceted fracture surface in wrought and HIPped Ti-8Al-1Mo-1V.

Schmid's law predicted the activation of slip systems in regions 1-3 based on the relative critical tensile stress (σ_c) calculation. Region 1 and 2 were taken from dimpled and faceted region in SCC sample of wrought Ti-811, and region 3 was lift-out from SCC facets of HIPped Ti-811. In spite of Schmid's law, there is a change in the dislocation types between the regions underneath pre-crack dimples and SCC facets in wrought Ti-811. Both regions were orientated favourably for basal $< a >$ slip, but $< c + a >$ slip was observed underneath SCC facets that failed in aqueous NaCl solution.

In addition to the change in dislocation type, an increase in dislocation density was observed in the SCC faceted region compared to that of the pre-crack dimples. The increased dislocation density is an evidence of micro-plasticity related to AIDE mechanism around the crack tip.

The crystallographic planes of the SCC facets were either parallel to, or inclined 15° away to the $(0002)_\alpha$ plane. The orientations of three facets are attributed to the operating dislocation types beneath.

The main hydrogen source is likely external absorbed hydrogen from the solution at the crack tip rather than solute hydrogen. Subsequent hydrogen diffusion is not solely dependent on bulk diffusion, but rather on pipe diffusion through the planar slip bands in α -Ti grains ahead of SCC crack tip.

Based on the TEM evidence, it may be concluded that a combined AIDE and HELP mechanism is proposed as the aqueous NaCl SCC mechanism for Ti-8Al-1Mo-1V.

CHAPTER VI: CONCLUSIONS

One research aim of this work was to determine the individual effect of microtexture and α_2 precipitates on SCC properties for Ti-8Al-1Mo-1V, and thereby to improve the SCC resistance of Ti-8Al-1Mo-1V by manipulating microtexture and α_2 precipitates in the alloy.

- i. Both ordered α_2 precipitates and microtexture were found to be detrimental to the SCC property of Ti-8Al-1Mo-1V. The slip bands on SCC facets are evidence of localized planar slip, which is promoted by α_2 precipitates and the SCC process is subsequently accelerated. The presence of microtextured regions increases the SCC crack propagation velocity significantly, and the SCC crack propagation direction is correlated to the microtexture according to the EBSD result.
- ii. Hot isostatic pressing (HIPping) without any post heat treatments can reduce the SCC susceptibility significantly compared to wrought Ti-8Al-1Mo-1V. In addition, the mechanical properties are not affected adversely by the HIPping processes.
- iii. Zero SCC susceptibility for Ti-8Al-1Mo-1V can be obtained by combining the HIPping process and appropriate post heat treatment to eliminate microtexture and α_2 precipitates. However, the post heat treatment, which suppresses the α_2 ordering transformation, results in a decrease in elastic modulus and yield strength. As Ti-8Al-1Mo-1V is weight reduction attractive in aerospace applications for its high young's modulus and specific strength, reduced elastic modulus and yield strength would weaken the advantages of Ti-8Al-1Mo-1V.
- iv. Fractography study showed that there was a transition between ductile dimpled fracture in air and flat faceted fracture in aqueous NaCl solution. Ductile features of tear ridges and slip bands on SCC facets were observed by high resolution SEM, which implies a localized plastic deformation in the microstructure adjacent and below the fracture surface.

Another research aim was to understand the SCC mechanism, which was investigated by studying the difference between the dislocation substructure in α grains underneath dimpled and SCC faceted fracture surface in wrought and HIPped Ti-8Al-1Mo-1V.

- v. The crystallographic planes of facets were either parallel to basal plane or close to a hydride habit plane $\{10\bar{1}7\}$. The facets orientation is a result of the operating dislocations underneath.
- vi. The activation of slip system is predicted by Schmid's law based on the relative critical tensile stress (σ_c) calculation. However, a dislocation type change is accompanied by the fracture mode change from ductile dimples to SCC facets. Both pre-crack dimpled and faceted regions of wrought Ti-8Al-1Mo-1V samples were orientated favourably for basal $\langle a \rangle$ slip. In addition to the predicted basal $\langle a \rangle$ slip, $\langle c + a \rangle$ slip was observed underneath SCC facets that failed in aqueous NaCl solution.
- vii. In addition to the dislocation type change, dislocation density was increased underneath SCC facets compared to that below the pre-crack dimples. The increased dislocation density implies increased degrees of microplasticity, which is related to hydrogen induced dislocation emission and hydrogen promoted dislocation motion during the SCC process.
- viii. It may be concluded that a combined SCC mechanism including absorption induced dislocation emission (AIDE) and hydrogen enhanced localized plasticity (HELP) is the aqueous NaCl SCC mechanism for Ti-8Al-1Mo-1V. Hydrogen is mainly externally absorbed hydrogen from the corrosive fluid around the crack tip. The following hydrogen diffusion should be primarily depended on pipe diffusion through slip bands in α grains.
- ix.

CHAPTER VII: SUGGESTIONS FOR FUTURE WORK

Although a reasonable explanation of microtexture and α_2 precipitates has emerged from this study, and two rational SCC mechanisms are established for the aqueous SCC in Ti-8Al-1Mo-1V. There are still number of interesting areas that should be investigated in future work.

- **Effect of size and volume fraction of α_2 precipitates on SCC properties:** In this work, the effect of α_2 precipitates was studied in the sample with and without microtexture. However, effects of size and volume fraction on SCC properties were not investigated. Techniques including TEM, and X-ray line broadening would be useful to study the size and volume fraction of α_2 precipitates in Ti-8Al-1Mo-1V obtained from different heat treatments. A correlation between α_2 precipitates size and volume fraction and SCC properties can be then established.
- **Effect of sharpness of microtexture on SCC properties:** Ti-8Al-1Mo-1V samples may have different sharpness of microtexture depending on the deformation type and degree in conventionally thermomechanical processing. If Ti-8Al-1Mo-1V samples with different texture intensity are available, it would be interesting to do SCC and EBSD studies to examine the effect of sharpness of microtexture on SCC properties.
- **In-situ SCC experiment in TEM:** If a TEM SCC cell is available, an in-situ SCC test can be performed in TEM. The obtained result will further support the established SCC mechanisms.
- **Extend the established SCC mechanism to other $\alpha+\beta$ Ti alloys:** SCC study of Ti-6Al-4V can be replicated to further extend the established theory to other $\alpha+\beta$ Ti alloys.

REFERENCE

- [1] M. Peters, J. Kumpfert, C.H. Ward, C. Leyens, Titanium Alloys for Aerospace Applications, *Adv Eng Mater*, 5 (2003) 419-427.
- [2] J.J. Lee, Historical and future trends in aircraft performance, cost, and emissions, in, Massachusetts Institute of Technology, 2000.
- [3] M. Easton, A. Beer, M. Barnett, C. Davies, G. Dunlop, Y. Durandet, S. Blacket, T. Hilditch, P. Beggs, Magnesium alloy applications in automotive structures, *JOM*, 60 (2008) 57-62.
- [4] E. Schubert, M. Klassen, I. Zerner, C. Walz, G. Sepold, Light-weight structures produced by laser beam joining for future applications in automobile and aerospace industry, *J Mater Process Tech*, 115 (2001) 2-8.
- [5] J.C. Williams, E.A. Starke Jr, Progress in structural materials for aerospace systems1, *Acta Mater*, 51 (2003) 5775-5799.
- [6] K. Faller, F.H. Froes, The use of titanium in family automobiles: Current trends, *JOM*, 53 (2001) 27-28.
- [7] F.H. Froes, H. Friedrich, J. Kiese, D. Bergoint, Titanium in the family automobile: The cost challenge, *JOM*, 56 (2004) 40-44.
- [8] G. Lutjering, J.C. Williams, *Titanium*, 2nd ed., Springer, Berlin, 2007.
- [9] C. Leyens, M. Peters, *Titanium and Titanium Alloys: Fundamentals and Applications*, WILEY-VCH Verlag GmbH & Co. KGaA, Weinheim, 2003.
- [10] M.J. Donachie, *Titanium: A Technical Guide*, 2nd ed., ASM International, Materials Park, 2000.
- [11] R. Boyer, G. Welsch, E.W. Collings, *Materials Properties Handbook:Titanium Alloys*, ASM International, Materials Park, 1996.
- [12] W. Sha, S. Malinov, *Titanium alloys: modelling of microstructure, properties and applications*, Elsevier, 2009.
- [13] A.L. Pilchak, A.H. Young, J.C. Williams, Stress corrosion cracking facet crystallography of Ti-8Al-1Mo-1V, *Corros Sci*, 52 (2010) 3287-3296.
- [14] D. Fager, W. Spurr, *SOME CHARACTERISTICS OF AQUEOUS STRESS CORROSION IN TITANIUM ALLOYS*, in: DTIC Document, The Boeing Company, Washington, 1967.
- [15] B.F. Brown, *Stress-corrosion cracking in high strength steels and in titanium and aluminum alloys*, Naval Research Lab, Washington DC, 1972.
- [16] S. Orman, G. Picton, The role of hydrogen in the stress corrosion cracking of titanium alloys, *Corros Sci*, 14 (1974) 451-459.
- [17] D.A. Meyn, An analysis of frequency and amplitude effects on corrosion fatigue crack propagation in Ti-8Al-1Mo-1V, *Metallurgical Transactions*, 2 (1971) 853-865.
- [18] J.C. Williams, Some observations on the stress-corrosion cracking of three commercial titanium alloys, in, DTIC Document, 1967.
- [19] D. Banerjee, J.C. Williams, Perspectives on Titanium Science and Technology, *Acta Mater*, 61 (2013) 844-879.
- [20] V.A. Joshi, *Titanium alloys: an atlas of structures and fracture features*, CRC Press, 2006.
- [21] C. Ramachandra, V. Singh, Precipitation of the ordered Ti_3Al phase in alloy Ti-6.3Al-2Zr-3.3Mo-0.30Si, *Scripta Metallurgica*, 20 (1986) 509-512.
- [22] I. Chatteraj, Stress corrosion cracking (SCC) and hydrogen-assisted cracking in titanium alloys, in: V.S. Raja, T. Shoji (Eds.) *Stress corrosion cracking*, Woodhead Publishing, 2011, pp. 381-408.
- [23] S. Billard, J.P. Fondère, B. Bacroix, G.F. Dirras, Macroscopic and microscopic aspects of the deformation and fracture mechanisms of ultrafine-grained aluminum processed by hot isostatic pressing, *Acta Mater*, 54 (2006) 411-421.
- [24] R.R. Boyer, *Titanium and Its Alloys: Metallurgy, Heat Treatment and Alloy Characteristics*, in: *Encyclopedia of Aerospace Engineering*, John Wiley & Sons, Ltd, 2010.
- [25] J.C. Williams, M.J. Blackburn, A Comparison of Phase Transformations in Threee Commercial Titanium Alloys, *ASM Transactions Quarterly*, 60 (1967) 373-383.
- [26] W.D. Callister, *Materials Science And Engineering: An Introduction*, John Wiley & Sons, 2007.
- [27] G.E. Dieter, *Mechanical metallurgy*, McGraw-Hill, New York, 1976.
- [28] J.C. Williams, R.G. Baggerly, N.E. Paton, Deformation behavior of HCP Ti-Al alloy single crystals, *Metall and Mat Trans A*, 33 (2002) 837-850.
- [29] D. Banerjee, J. Williams, Microstructure and slip character in titanium alloys, *Defence Sci J*, 36 (1986) 191-206.
- [30] K.S. Ravichandran, Near threshold fatigue crack growth behavior of a titanium alloy: Ti-6Al-4V, *Acta Metallurgica et Materialia*, 39 (1991) 401-410.
- [31] T.R. Cass, *The science, technology and application of titanium*, Pergamon Press, London, 1970) p, 459 (1970).

- [32] R.H. Ericksen, R. Taggart, D.H. Polonis, The martensite transformation in Ti-Cr binary alloys, *Acta Metallurgica*, 17 (1969) 553-564.
- [33] H.M. Flower, P.R. Swann, D.R.F. West, The effect of Si,Zr, Al and Mo on the structure and strength of Ti martensite, *J Mater Sci*, 7 (1972) 929-938.
- [34] S.C. Wang, M. Aindow, M.J. Starink, Effect of self-accommodation on α/α boundary populations in pure titanium, *Acta Mater*, 51 (2003) 2485-2503.
- [35] Z. Nishiyama, M. Oka, H. Nakagawa, The Electron Microscopic Structure and Lattice Defects of the Martensite in Commercially Pure Titanium, *Transactions of the Japan Institute of Metals*, 7 (1966) 168-173.
- [36] M.J. Blackburn, J.A. Feeney, T.R. Beck, Stress-Corrosion Cracking of Titanium Alloys, in: M. Fontana, R. Staehle (Eds.) *Advances in Corrosion Science and Technology*, Springer US, 1973, pp. 67-292.
- [37] L. Germain, N. Gey, M. Humbert, A. Hazotte, P. Bocher, M. Jahazi, An automated method to analyze separately the microtextures of primary α grains and the secondary α s inherited colonies in bimodal titanium alloys, *Mater Charact*, 54 (2005) 216-222.
- [38] F. Wagner, N. Bozzolo, O. Van Landuyt, T. Grosdidier, Evolution of recrystallisation texture and microstructure in low alloyed titanium sheets, *Acta Mater*, 50 (2002) 1245-1259.
- [39] A.W. Bowen, The influence of crystallographic orientation on the fracture toughness of strongly textured Ti-6Al-4V, *Acta Metallurgica*, 26 (1978) 1423-1433.
- [40] F. Bridier, P. Villechaise, J. Mendez, Slip and fatigue crack formation processes in an α/β titanium alloy in relation to crystallographic texture on different scales, *Acta Mater*, 56 (2008) 3951-3962.
- [41] K. Le Biavant, S. Pommier, C. Prioul, Local texture and fatigue crack initiation in a Ti-6Al-4V titanium alloy, *Fatigue Fract Eng M*, 25 (2002) 527-545.
- [42] N. Gey, P. Bocher, E. Uta, L. Germain, M. Humbert, Texture and microtexture variations in a near- α titanium forged disk of bimodal microstructure, *Acta Mater*, 60 (2012) 2647-2655.
- [43] L. Germain, N. Gey, M. Humbert, P. Bocher, M. Jahazi, Analysis of sharp microtexture heterogeneities in a bimodal IMI 834 billet, *Acta Mater*, 53 (2005) 3535-3543.
- [44] L. Germain, N. Gey, M. Humbert, P. Vo, M. Jahazi, P. Bocher, Texture heterogeneities induced by subtransus processing of near α titanium alloys, *Acta Mater*, 56 (2008) 4298-4308.
- [45] I. Bantounas, D. Dye, T.C. Lindley, The role of microtexture on the faceted fracture morphology in Ti-6Al-4V subjected to high-cycle fatigue, *Acta Mater*, 58 (2010) 3908-3918.
- [46] A.L. Pilchak, A simple model to account for the role of microtexture on fatigue and dwell fatigue lifetimes of titanium alloys, *Scripta Mater*, 74 (2014) 68-71.
- [47] E. Uta, N. Gey, P. Bocher, M. Humbert, J. Gilgert, Texture heterogeneities in α / α s titanium forging analysed by EBSD-Relation to fatigue crack propagation, *Journal of Microscopy*, 233 (2009) 451-459.
- [48] I. Bantounas, T.C. Lindley, D. Rugg, D. Dye, Effect of microtexture on fatigue cracking in Ti-6Al-4V, *Acta Mater*, 55 (2007) 5655-5665.
- [49] M.R. Bache, M. Cope, H.M. Davies, W.J. Evans, G. Harrison, Dwell sensitive fatigue in a near alpha titanium alloy at ambient temperature, *Int J Fatigue*, 19 (1997) 83-88.
- [50] M. Atapour, A. Pilchak, M. Shamanian, M. Fathi, Corrosion behavior of Ti-8Al-1Mo-1V alloy compared to Ti-6Al-4V, *Mater Design*, 32 (2011) 1692-1696.
- [51] M. Nakagawa, S. Matsuya, T. Shiraishi, M. Ohta, Effect of Fluoride Concentration and pH on Corrosion Behavior of Titanium for Dental Use, *J Dent Res*, 78 (1999) 1568-1572.
- [52] S.L.d. Assis, S. Wolynec, I. Costa, Corrosion characterization of titanium alloys by electrochemical techniques, *Electrochim Acta*, 51 (2006) 1815-1819.
- [53] M.J. Muñoz-Portero, J. García-Antón, J.L. Guiñón, R. Leiva-García, Pourbaix diagrams for titanium in concentrated aqueous lithium bromide solutions at 25°C, *Corros Sci*, 53 (2011) 1440-1450.
- [54] S.Y. Yu, J.R. Scully, Corrosion and Passivity of Ti-13% Nb-13% Zr in Comparison to Other Biomedical Implant Alloys, *Corrosion*, 53 (1997) 965-976.
- [55] N.T.C. Oliveira, A.C. Guastaldi, Electrochemical stability and corrosion resistance of Ti-Mo alloys for biomedical applications, *Acta Biomaterialia*, 5 (2009) 399-405.
- [56] E. Peláez-Abellán, L. Rocha-Sousa, W.D. Müller, A.C. Guastaldi, Electrochemical stability of anodic titanium oxide films grown at potentials higher than 3 V in a simulated physiological solution, *Corros Sci*, 49 (2007) 1645-1655.
- [57] R.C. Newman, 2.09 - Stress Corrosion Cracking, in: B. Cottis, M. Graham, R. Lindsay, S. Lyon, T. Richardson, D. Scantlebury, H. Stott (Eds.) *Shreir's Corrosion*, Elsevier, Oxford, 2010, pp. 864-901.
- [58] S.P. Lynch, 1 - Mechanistic and fractographic aspects of stress-corrosion cracking (SCC), in: V.S. Raja, T. Shoji (Eds.) *Stress Corrosion Cracking*, Woodhead Publishing, 2011, pp. 3-89.
- [59] M.J. Blackburn, J.C. Williams, Metallurgical aspects of the stress corrosion cracking of titanium alloys, in: R.W. Staehle, A.J. Forty, D.v. Rooyen (Eds.) *Proceedings of the Conference on Fundamental Aspects of Stress Corrosion Cracking*, National Association of Corrosion Engineers, The Ohio State University, Columbus, OH, 1967, pp. 620-636.

- [60] R.W. Schutz, Titanium, in: R. Baboian (Ed.) Corrosion Tests and Standards: Applications and Interpretation, ASTM International, West Conshohocken, 2005, pp. 598.
- [61] N. Winzer, A. Atrens, G. Song, E. Ghali, W. Dietzel, K.U. Kainer, N. Hort, C. Blawert, A Critical Review of the Stress Corrosion Cracking (SCC) of Magnesium Alloys, *Adv Eng Mater*, 7 (2005) 659-693.
- [62] J.A. Beavers, B.A. Harle, Mechanisms of High-pH and Near-Neutral-pH SCC of Underground Pipelines, *Journal of Offshore Mechanics and Arctic Engineering*, 123 (2001) 147-151.
- [63] M.D. Pustode, V.S. Raja, N. Paulose, The stress-corrosion cracking susceptibility of near- α titanium alloy IMI 834 in presence of hot salt, *Corros Sci*, 82 (2014) 191-196.
- [64] R.J.H. Wanhill, Aqueous Stress Corrosion in Titanium Alloys, *Brit Corros J*, 10 (1975) 69-78.
- [65] S.P. Lynch, 2 - Hydrogen embrittlement (HE) phenomena and mechanisms, in: V.S. Raja, T. Shoji (Eds.) *Stress corrosion cracking*, Woodhead Publishing, 2011, pp. 90-130.
- [66] M.H.O. Könönen, E.T. Lavonius, J.K. Kivilahti, SEM observations on stress corrosion cracking of commercially pure titanium in a topical fluoride solution, *Dent Mater*, 11 (1995) 269-272.
- [67] D.S. Shih, I.M. Robertson, H.K. Birnbaum, Hydrogen embrittlement of α titanium: In situ tem studies, *Acta Metallurgica*, 36 (1988) 111-124.
- [68] D. Mauney, E. Starke Jr, R. Hochman, Hydrogen Embrittlement and Stress Corrosion Cracking in Ti-Al Binary Alloys, *Corrosion*, 29 (1973) 241-244.
- [69] J.C. Scully, D.T. Powell, The stress corrosion cracking mechanism of α -titanium alloys at room temperature, *Corros Sci*, 10 (1970) 719-733.
- [70] M. Koyama, C.C. Tasan, E. Akiyama, K. Tsuzaki, D. Raabe, Hydrogen-assisted decohesion and localized plasticity in dual-phase steel, *Acta Mater*, 70 (2014) 174-187.
- [71] S.P. Knight, Stress corrosion cracking of Al-Zn-Mg-Cu alloys: effects of heat-treatment, environment, and alloy composition, in: Department of Materials Engineering, Monash University, Melbourne, 2008.
- [72] D.P. Abraham, C.J. Altstetter, Hydrogen-enhanced localization of plasticity in an austenitic stainless steel, *Metall and Mat Trans A*, 26 (1995) 2859-2871.
- [73] S.P. Lynch, S. Moutsos, A brief history of fractography, *Journal of Failure Analysis and Prevention*, 6 (2006) 54-69.
- [74] G. Lu, Q. Zhang, N. Kioussis, E. Kaxiras, Hydrogen-Enhanced Local Plasticity in Aluminum: An *ab initio* Study, *Phys Rev Lett*, 87 (2001) 095501.
- [75] A.L. Pilchak, J.C. Williams, Observations of Facet Formation in Near- α Titanium and Comments on the Role of Hydrogen, *Metall and Mat Trans A*, 42 (2011) 1000-1027.
- [76] H.V. Sudhaker Nayak, K.I. Vasu, Y.V.R.K. Prasad, Texture dependent stress corrosion failure of commercial titanium sheets in bromine-methanol solution, *J Mater Sci*, 15 1265-1275.
- [77] X.G. Zhang, J. Vereecken, Stress Corrosion Cracking Mechanism of Ti-6Al-4V in Acidic Methanol, *Corrosion*, 46 (1990) 136-141.
- [78] K.W. Gao, W.Y. Chu, B. Gu, T.C. Zhang, L.J. Qiao, In-Situ Transmission Electron Microscopic Observation of Corrosion-Enhanced Dislocation Emission and Crack Initiation of Stress Corrosion, *Corrosion*, 56 (2000) 515-522.
- [79] J.K. Gregory, H.G. Brokmeier, The relationship between crystallographic texture and salt water cracking susceptibility in Ti-6Al-4V, *Materials Science and Engineering: A*, 203 (1995) 365-372.
- [80] D.N. Fager, W.F. Spurr, SOME CHARACTERISTICS OF AQUEOUS STRESS CORROSION IN TITANIUM ALLOYS, *Trans. ASM*, 61 (1968).
- [81] T.R. Beck, M.J. Blackburn, Stress corrosion cracking of titanium alloys, *AIAA J*, 6 (1968) 326-332.
- [82] J.C. Williams, R. Taggart, D.H. Polonis, The morphology and substructure of Ti-Cu martensite, *Metallurgical Transactions*, 1 (1970) 2265-2270.
- [83] J.C. Williams, A.W. Sommer, P.P. Tung, The influence of oxygen concentration on the internal stress and dislocation arrangements in α titanium, *Metallurgical Transactions*, 3 (1972) 2979-2984.
- [84] A.P. Woodfield, P.J. Postans, M.H. Loretto, R.E. Smallman, The effect of long-term high temperature exposure on the structure and properties of the titanium alloy Ti 5331S, *Acta Metallurgica*, 36 (1988) 507-515.
- [85] L.-A. Yao, F.-X. Gan, Y.-X. Zhao, C.-L. Yao, J.L. Bear, Microelectrode Monitoring the Crevice Corrosion of Titanium, *Corrosion*, 47 (1991) 420-423.
- [86] I.M. Robertson, H.K. Birnbaum, P. Sofronis, Chapter 91 Hydrogen Effects on Plasticity, in: J.P. Hirth, L. Kubin (Eds.) *Dislocations in Solids*, Elsevier, 2009, pp. 249-293.
- [87] H.-J. Christ, M. Decker, S. Zeitler, Hydrogen diffusion coefficients in the titanium alloys IMI 834, Ti 10-2-3, Ti 21 S, and alloy C, *Metall and Mat Trans A*, 31 1507-1517.
- [88] R. Wasilewski, G. Kehl, Diffusion of hydrogen in titanium, *Metallurgia (England)* Published August 1971-December 1977 as *Metall. Met. Form.*, 50 (1954).
- [89] J. Tien, A. Thompson, I.M. Bernstein, R. Richards, Hydrogen transport by dislocations, *Metallurgical Transactions A*, 7 (1976) 821-829.

- [90] J. Albrecht, I.M. Bernstein, A.W. Thompson, Evidence for Dislocation Transport of Hydrogen in Aluminum, *Metallurgical Transactions A*, 13 (1982), 811-820.
- [91] A.C. Hollis, J.C. Scully, The stress corrosion cracking and hydrogen embrittlement of titanium in methanol-hydrochloric acid solutions, *Corros Sci*, 34 (1993) 821-835.
- [92] C.Q. Chen, S.X. Li, K. Lu, Dislocation interaction with hydrides in titanium containing a low hydrogen concentration, *Philosophical Magazine*, 84 (2004) 29-43.
- [93] H. Matsunaga, H. Noda, Visualization of Hydrogen Diffusion in a Hydrogen-Enhanced Fatigue Crack Growth in Type 304 Stainless Steel, *Metall and Mat Trans A*, 42 (2011) 2696-2705.
- [94] R. Narayanan, S.K. Seshadri, T.-Y. Kwon, K.-H. Kim, Corrosion of anodic TiO coatings on Ti-6Al-4V in simulated body fluid, *Journal of Biomedical Materials Research Part A*, 86A (2008) 502-509.
- [95] W.M. Haynes, CRC handbook of chemistry and physics, CRC press, 2014.
- [96] A. Kawabe, I. Nakagawa, Z. Kanno, Y. Tsutsumi, T. Hanawa, T. Ono, Evaluation of biofilm formation in the presence of saliva on poly(ethylene glycol)-deposited titanium, *Dental Materials Journal*, 33 (2014) 638-647.
- [97] K. Zhang, The microstructure and properties of hipped powder Ti alloys, in: School of Metallurgy and Materials, University of Birmingham, 2010, pp. 266.
- [98] F.H. Froes, D. Eylon, Powder metallurgy of titanium alloys, *Int Mater Rev*, 35 (1990) 162-184.
- [99] H.V. Atkinson, S. Davies, Fundamental aspects of hot isostatic pressing: An overview, *Metall and Mat Trans A*, 31 (2000) 2981-3000.
- [100] K. Zhang, J. Mei, N. Wain, X. Wu, Effect of Hot-Isostatic-Pressing Parameters on the Microstructure and Properties of Powder Ti-6Al-4V Hot-Isostatically-Pressed Samples, *Metall and Mat Trans A*, 41 (2010) 1033-1045.
- [101] A.S. Helle, K.E. Easterling, M.F. Ashby, Hot-isostatic pressing diagrams: New developments, *Acta Metallurgica*, 33 (1985) 2163-2174.
- [102] K.T. Kim, H.C. Yang, Densification behaviour of titanium alloy powder under hot isostatic pressing, *Powder Metall*, 44 (2001) 41-47.
- [103] F.H. Froes, S.J. Mashl, J.C. Hebeisen, V.S. Moxson, V.A. Duz, The technologies of titanium powder metallurgy, *JOM*, 56 (2004) 46-48.
- [104] ASTM, E1409-13, Standard Test Method for Determination of Oxygen and Nitrogen in Titanium and Titanium Alloys by Inert Gas Fusion, , in, ASTM International, West Conshohocken, PA, 2013.
- [105] ASTM, E1447-09, Standard Test Method for Determination of Hydrogen in Titanium and Titanium Alloys by Inert Gas Fusion Thermal Conductivity/Infrared Detection Method, in, ASTM International, West Conshohocken, PA, 2016.
- [106] ASTM, G168-00, Standard Practice for Making and Using Precracked Double Beam Stress Corrosion Specimens, in, ASTM International, West Conshohocken, PA, 2000.
- [107] J. Card, R. Cannon, E. Saiz, A. Tomsia, R. Ritchie, On the physics of moisture-induced cracking in metal-glass (copper-silica) interfaces, *J Appl Phys*, 102 (2007) 053516.
- [108] ASTM, E8/E8M-11, Standard test methods for tension testing on metallic materials, in, ASTM International, West Conshohocken, PA 2011.
- [109] R.J. Young, M.V. Moore, Dual-Beam (FIB-SEM) Systems, in: L.A. Giannuzzi, F.A. Stevie (Eds.) *Introduction to Focused Ion Beams: Instrumentation, Theory, Techniques and Practice*, Springer US, Boston, MA, 2005, pp. 247-268.
- [110] D.J. Dingley, Dislocation Invisibility in Dark-Field Electron Microscopy, *physica status solidi (b)*, 38 (1970) 345-355.
- [111] M. Zakaria, W. Voice, A. Wilson, M.H. Loretto, X. Wu, The influence of strain rate on the visibility of dislocations in transmission electron microscopy images of deformed Ti-6 wt% Al-4 wt% V and in Timet 550, *Philosophical Magazine*, 84 (2004) 887-898.
- [112] K. Higashida, N. Narita, M. Tanaka, T. Morikawa, Y. Miura, R. Onodera, Crack tip dislocations in silicon characterized by high-voltage electron microscopy, *Philosophical Magazine A*, 82 (2002) 3263-3273.
- [113] P.R. Munroe, The application of focused ion beam microscopy in the material sciences, *Mater Charact*, 60 (2009) 2-13.
- [114] C.A. Volkert, A.M. Minor, Focused Ion Beam Microscopy and Micromachining, *Mrs Bull*, 32 (2007) 389-399.
- [115] D. Kiener, C. Motz, M. Rester, M. Jenko, G. Dehm, FIB damage of Cu and possible consequences for miniaturized mechanical tests, *Materials Science and Engineering: A*, 459 (2007) 262-272.
- [116] T. Chapman, V. Vorontsov, A. Sankaran, D. Rugg, T. Lindley, D. Dye, The Dislocation Mechanism of Stress Corrosion Embrittlement in Ti-6Al-2Sn-4Zr-6Mo, *Metall and Mat Trans A*, 47 (2016) 282-292.
- [117] S.-C. Liao, J. Duffy, Adiabatic shear bands in a Ti-6Al-4V titanium alloy, *J Mech Phys Solids*, 46 (1998) 2201-2231.

- [118] X. Feaugas, M. Clavel, CYCLIC DEFORMATION BEHAVIOUR OF AN α/β TITANIUM ALLOY—I. MICROMECHANISMS OF PLASTICITY UNDER VARIOUS LOADING PATHS, *Acta Mater.*, 45 (1997) 2685-2701.
- [119] I. Robertson, P. Sofronis, A. Nagao, M.L. Martin, S. Wang, D.W. Gross, K.E. Nygren, Hydrogen Embrittlement Understood, *Metall and Mater Trans B*, 46 (2015) 1085-1103.
- [120] S. Cao, C.V.S. Lim, B. Hinton, X. Wu, Effects of microtexture and Ti3Al (α_2) precipitates on stress-corrosion cracking properties of a Ti-8Al-1Mo-1V alloy, *Corros Sci.*, 116 (2017) 22-33.
- [121] N. Cheneau-Späth, J.H. Driver, Plane Strain Compression of Titanium Crystals, in: *Mater Sci Forum*, *Trans Tech Publ*, 1994, pp. 639-644.
- [122] T.R. Bieler, S.L. Semiatin, The origins of heterogeneous deformation during primary hot working of Ti-6Al-4V, *Int J Plasticity*, 18 (2002) 1165-1189.
- [123] M. Wollgarten, M. Beyss, K. Urban, H. Liebertz, U. Köster, Direct evidence for plastic deformation of quasicrystals by means of a dislocation mechanism, *Phys Rev Lett*, 71 (1993) 549-552.
- [124] H. Numakura, Y. Minonishi, M. Koiwa, $<11\bar{2}3>\{10\bar{1}1\}$ slip in titanium polycrystals at room temperature, *Scripta Metallurgica*, 20 (1986) 1581-1586.
- [125] D. Terada, S. Inoue, N. Tsuji, Microstructure and mechanical properties of commercial purity titanium severely deformed by ARB process, *J Mater Sci*, 42 (2007) 1673-1681.
- [126] M.H. Yoo, Slip, twinning, and fracture in hexagonal close-packed metals, *Metallurgical Transactions A*, 12 (1981) 409-418.
- [127] R.V. Mises, Mechanik der plastischen Formänderung von Kristallen, *ZAMM - Journal of Applied Mathematics and Mechanics / Zeitschrift für Angewandte Mathematik und Mechanik*, 8 (1928) 161-185.
- [128] A.L. Pilchak, W.J. Porter, R. John, Room temperature fracture processes of a near- α titanium alloy following elevated temperature exposure, *J Mater Sci*, 47 (2012) 7235-7253.
- [129] M.L. Wasz, F.R. Brotzen, R.B. McLellan, A.J. Griffin, Effect of oxygen and hydrogen on mechanical properties of commercial purity titanium, *Int Mater Rev*, 41 (1996) 1-12.
- [130] I.M. Robertson, The effect of hydrogen on dislocation dynamics, *Eng Fract Mech*, 68 (2001) 671-692.
- [131] H.K. Birnbaum, P. Sofronis, Hydrogen-enhanced localized plasticity—a mechanism for hydrogen-related fracture, *Materials Science and Engineering: A*, 176 (1994) 191-202.
- [132] B. Gu, J. Luo, X. Mao, Hydrogen-Facilitated Anodic Dissolution-Type Stress Corrosion Cracking of Pipeline Steels in Near-Neutral pH Solution, *Corrosion*, 55 (1999) 96-106.
- [133] J. Woodtli, R. Kieselbach, Damage due to hydrogen embrittlement and stress corrosion cracking, *Eng Fail Anal*, 7 (2000) 427-450.
- [134] D. Delafosse, T. Magnin, Hydrogen induced plasticity in stress corrosion cracking of engineering systems, *Eng Fract Mech*, 68 (2001) 693-729.
- [135] X. Wu, Y. Katada, I.S. Kim, S.G. Lee, Hydrogen-involved tensile and cyclic deformation behavior of low-alloy pressure vessel steel, *Metall and Mat Trans A*, 35 (2004) 1477-1486.
- [136] G. Itoh, K. Koyama, M. Kanno, Evidence for the transport of impurity hydrogen with gliding dislocations in aluminum, *Scripta Mater*, 35 (1996) 695-698.
- [137] C. Hwang, I.M. Bernstein, Dislocation transport of hydrogen in iron single crystals, *Acta Metallurgica*, 34 (1986) 1001-1010.
- [138] M. Gerland, P. Lefranc, V. Doquet, C. Sarrazin-Baudoux, Deformation and damage mechanisms in an α/β 6242 Ti alloy in fatigue, dwell-fatigue and creep at room temperature. Influence of internal hydrogen, *Materials Science and Engineering: A*, 507 (2009) 132-143.

Appendix

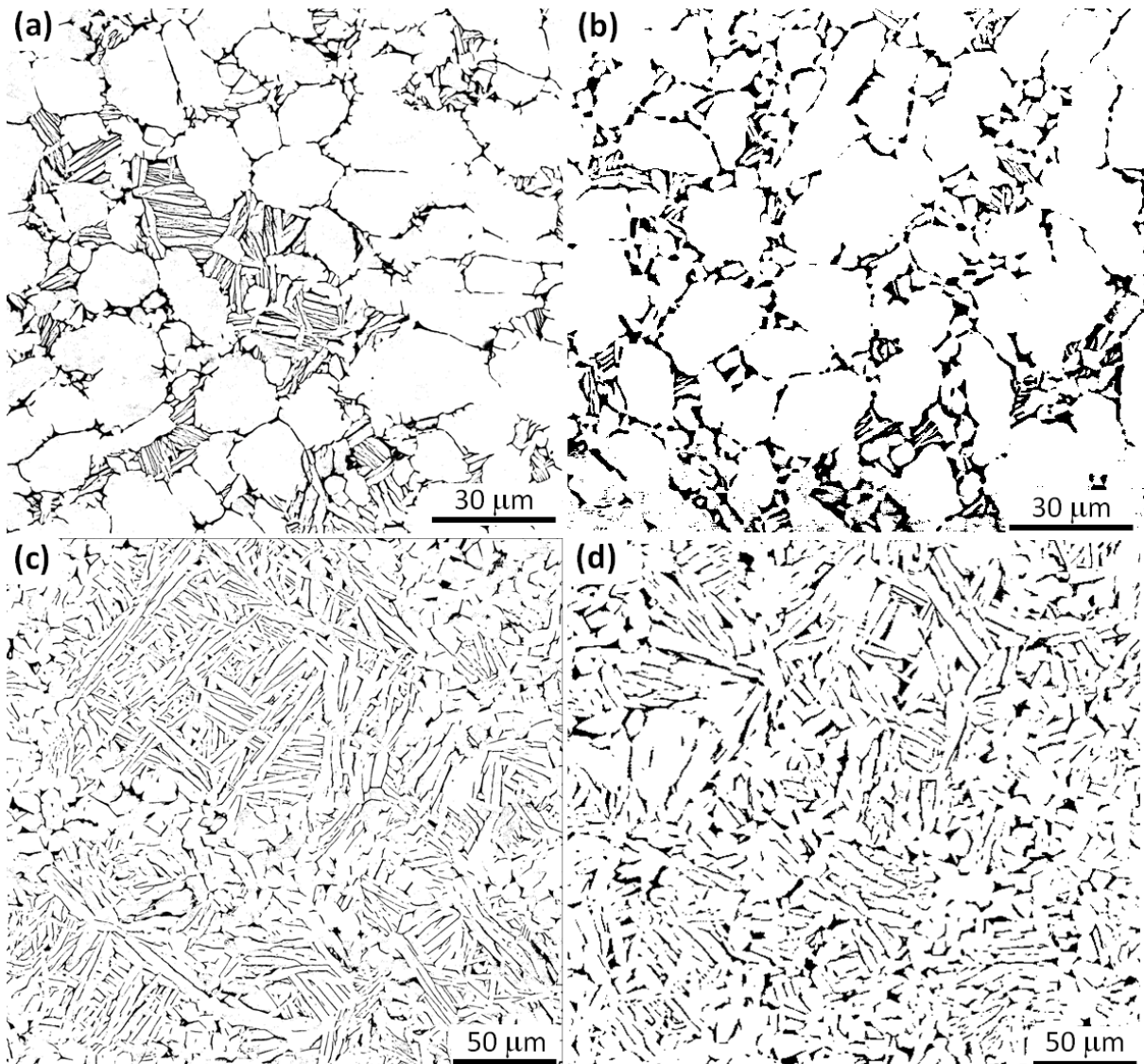


Fig. A1. Threshold image of Fig. 4.1 for phase volume fraction measurement. White phase is α , and black phase is β .

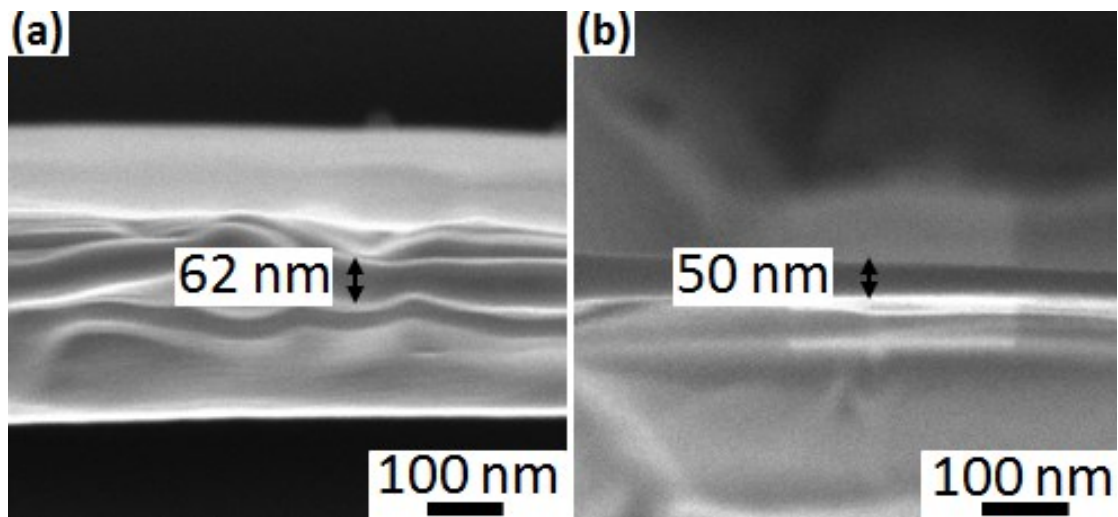


Fig. A2. The thickness of FIB lift-out lamellae obtained from the wrought Ti-811 sample, (a) the thickness of Pt deposition above region 1 in Fig. 5.2b, and (b) the thickness of Pt deposition above region 2 in Fig. 5.2e.

According to Fig. A2, the thickness of retained Pt deposition on FIB lift-out foils are similar above regions 1 and 2 in Fig. 5.2. As regions 1 and 2 are located next to the Pt deposition layers. It would be expected that the thickness of these two regions are similar.

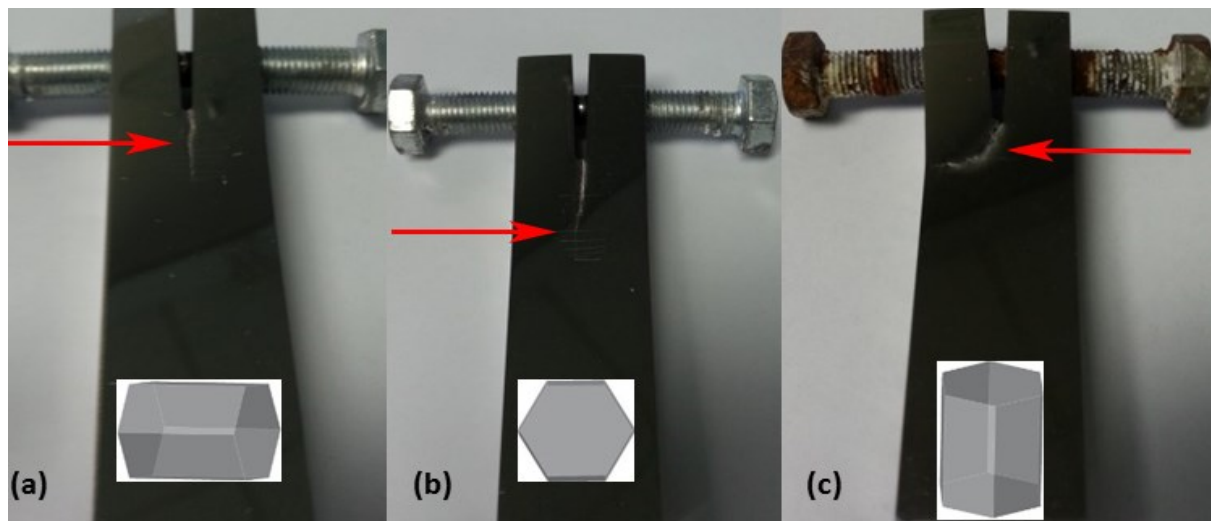


Fig. A3. SCC crack propagation in DCB samples with different orientations in 0.1 M aqueous NaCl solution.

Fig. A3 shows the SCC crack propagation direction in samples with different orientations sectioned from the wrought Ti-811 bar.